107學年度

學生專題研究論文集

東 海 大 學 應 用 物 理 系

目錄

Comparison on the structure and exchange bias in Co/MnPt and MnPt/Co polycrystalline films on glass substrates

H.W. Chang[1]*, P.Y. Yeh[2], Y.C. Chen[2], Y.L. Lai[2], P.H. Pan[2], C.R. Wang[2], Lance Horng[3], W.C. Chang[1]

[1] Department of Physics, National Chung Cheng University, Chia-Yi, 621 Taiwan
[2] Department of Applied Physics, Tunghai University, Taichung, 407 Taiwan.
[4] Department of Physics, National Changhua University of Education, Changhua 500, Taiwan.

Introduction

Exchange bias (EB), characterized by a shift of hysteresis loop originated from the interaction between the ferromagnetic (FM) and antiferromagnetic (AF) layers, is foundation for spin-valve (SV) based devices.

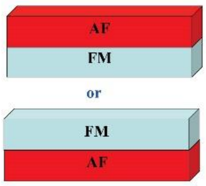

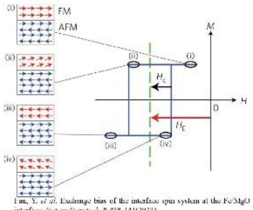

Fan, Y. et al. Exchange bias of the interface spin system at the Fe/MgO interface. Nature Nanotech. 8, 438-444 (2013)

For exchange bias material

$L1_0$-MnPt advantage:

1. **High T_N (975 K)**
2. **Large K_{AF} of 1.4×10^7 erg/cm^3**
3. **Excellent corrosion resistance**

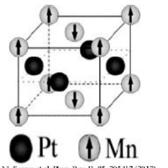

Marcio M. Soares et al. Phys. Rev. B, 85, 205417 (2012)

In this work, the effect of post thermal process on ordering phase transformation, microstructure, and EB field of Co/MnPt (MnPt at bottom of bilayer) and MnPt/Co (MnPt at top of the bilayer) bilayers on Ta underlayer are studied.

Experiment

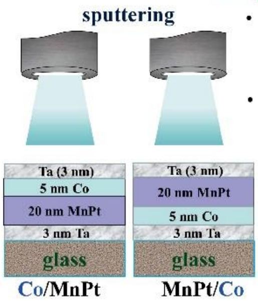

- **At RT by magnetron sputtering at the external magnetic field of 1 kOe induced from NdFeB sintered magnets.**
- **Field (2 kOe) cooling from 150 to 300 °C to RT.**

Analysis:

Crystal structures by XRD	Magnetization curve by AGM
Microstructure by TEM	Surface morphology by AFM

Results and Discussion

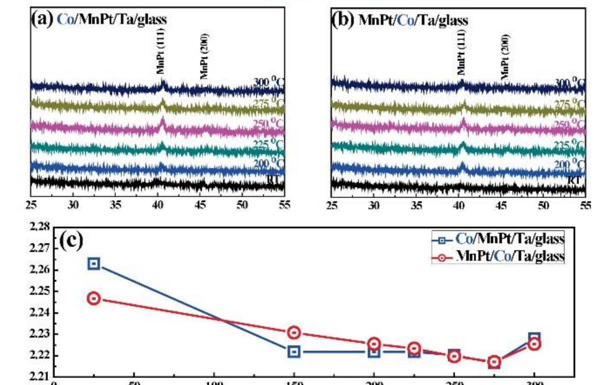

FIG. 1. XRD patterns of (a) Co/MnPt and (b) MnPt/Co films annealed at various temperatures, and (c) (111)-spacing of Co/MnPt and MnPt/Co films annealed at various temperatures in the range of 150-300 oC.

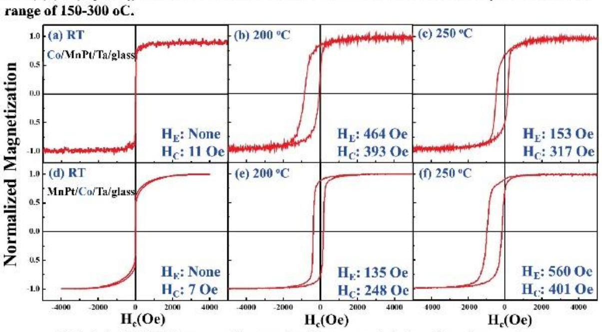

FIG. 2. (a)-(f) M-H curves of two series films annealed at various temperature.

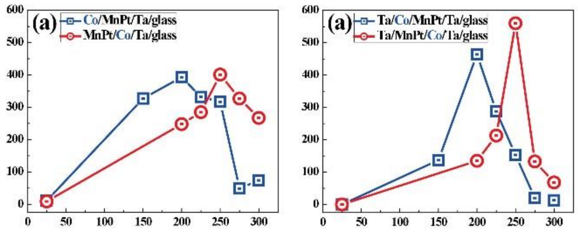

FIG. 3. (a) H_c and (b) H_E of the studied films annealed at various temperatures.

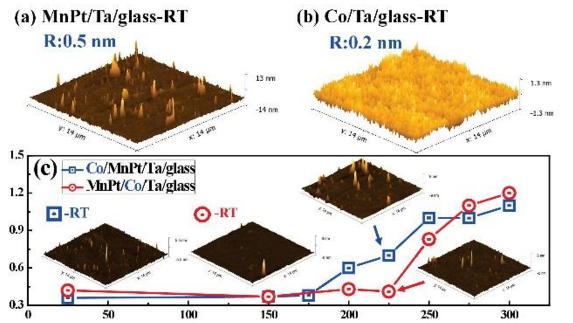

FIG. 4. AFM images of (a) the as-deposited MnPt film, (b) the as-deposited Co film, (c) the root-mean-square roughness (R) of the studied films annealed at various temperatures.

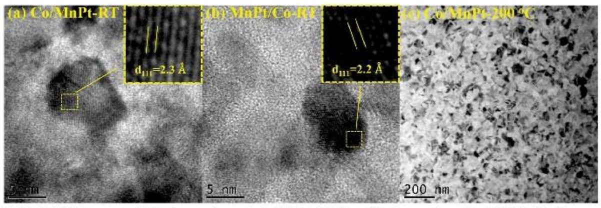

FIG.5. TEM images of (a) the as-deposited Co/MnPt film, (b) the as-deposited MnPt/Co film, and (c) Co/MnPt film annealed at 200 °C.

Conclusions

- **The increase of H_E with T is mainly dominated by the ordering degree of MnPt layer and the roughness of the interface.**
- **The ordering behavior and the roughness with increasing T might be related to the stress/strain state of the MnPt layer in as-deposited films.**
- **As compared to MnPt/Co film (T = 250 °C), Co/MnPt film with more compressive in film plane exhibits $L1_0$-ordering, the onset of stress release, and the optimized H_E at lower T = 200 °C.**

Structural evolution, ferroelectric, and nanomechanical properties of $Bi_{1-x}Sm_xFeO_3$ films (x = 0.05-0.16) on glass substrates

T.K. Lin[1], C.C. Kao[1], C.F. Chang[1], H.W. Chang[2*], C.R. Wang[1], C.S. Tu[3]

1 Department of Applied Physics, Tunghai University, Taichung 407, Taiwan
2 Department of Physics, National Chung Cheng University, ChiaYi 621, Taiwan
3 Department of Physics, Fu Jen Catholic University, Taipei 24205, Taiwan

I. INTRODUCTION

- Perovskite $BiFeO_3$(BFO), showing outstanding multiferroic(MF) properties of ferroelectricity(FE) (T_C ~810℃) and antiferromagnetism(AFM) (T_N~370ºC), has recently received considerable attention.
- The major problems in BFO is high leakage current, and therefore, Sm-doped-BFO(BSFO) was reported as an effective way to reduce leakage and thus enhance ferroelectric properties.
- In this study, $Bi_{1-x}Sm_xFeO_3$ films with x = 0.05-0.16 are grown on refined metallic Pt(111) electrode layer buffered glass substrate by pulsed laser deposition (PLD) at reduced temperature of 450°C.

II.EXPERIMENT

- BSFO thin films of 200 nm thickness was deposited on a Pt/glass stack using PLD at 450°C and an oxygen pressure of 30 mTorr.

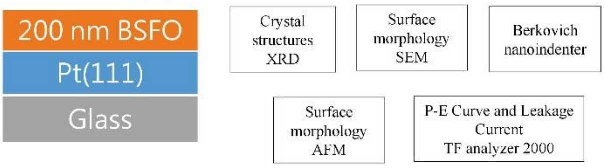

III.RESULT AND DISCUSSION

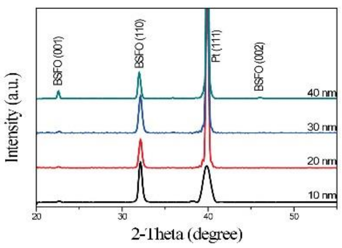

Fig. 1. XRD patterns of $Bi_{0.90}Sm_{0.10}FeO_3$ films deposited on Pt underlayers with the thickness in the range of 10-40 nm.

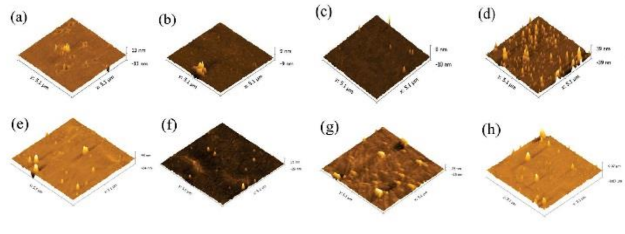

Fig. 2. AFM images of the refined Pt with the thickness of (a) 10 nm, (b) 20 nm, (c) 30 nm, and (d) 40nm, and those of 200-nm-thick $Bi_{0.90}Sm_{0.10}FeO_3$ films deposited on Pt underlayer with the thickness of (e) 10 nm, (f) 20 nm, (g) 30 nm, and (h) 40nm.

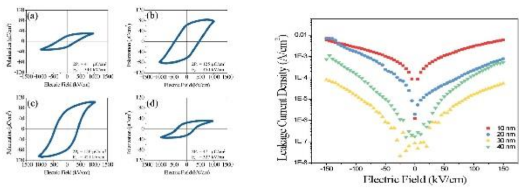

Fig. 3. P-E curves of $Bi_{0.90}Sm_{0.10}FeO_3$ films on Pt underlayers with the thickness of (a) 10 nm, (b) 20 nm, (c) 30 nm, and (d) 40 nm (e) Leakage current density of $Bi_{0.90}Sm_{0.10}FeO_3$ films on Pt underlayers with the thickness of 10-40 nm.

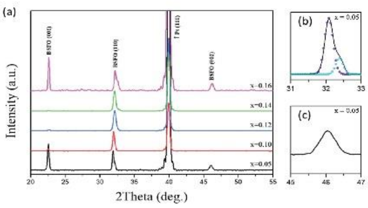

Fig. 5. XRD patterns of the $Bi_{1-x}Sm_xFeO_3$ films (x = 0.05-0.16) on 30-nm-thick Pt underlayer

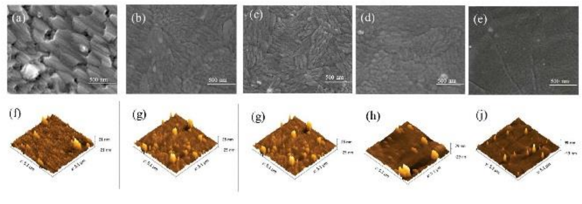

Fig. 5. SEM images of the samples with (a) x = 0.05, (b) x = 0.10, (c) x = 0.12, (d) x = 0.14, and (e) x = 0.16, and AFM images of the samples with (f) x = 0.05, (g) x = 0.10, (h) x = 0.12, (i) x = 0.14, and (j) x = 0.16.

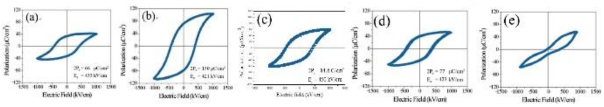

Fig. 6. P-E curves of the samples with (a) x = 0.05 (b) x = 0.10 (c) x = 0.12 (d) x = 0.14 and (e) x = 0.16.

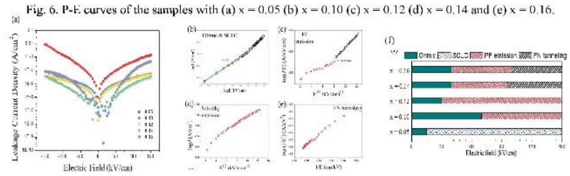

Fig. 7. (a) Leakage current density of the $Bi_{1-x}Sm_xFeO_3$ films (x = 0.05-0.16), curves fitting results of leakage current of the $Bi_{0.9}Sm_{0.1}FeO_3$ film with (b) Ohmic and SCLC mechanism, (c) PF emission, (d) Schottky emission, (e) FN tunneling, and (f) leakage mechanisms of the $Bi_{1-x}Sm_xFeO_3$ films (x = 0.05-0.16).

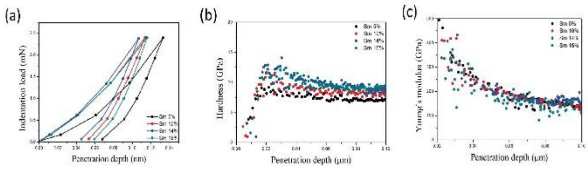

Fig. 8. (a) Load-displacement, (b) hardness-displacement and (c) young's modulus-displacement curves for BSFO thin films with x = 0.05-0.16.

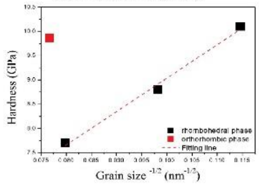

Fig. 10. Plot of the experimental data of hardness versus grain size. The dashed line represents a fit to the Hall-Petch equation with $H(D) = 2.16 + 68.7 D^{-1/2}$, except for the orthorhombic phase.

Table. 1 Ferroelectric properties of the developed Sm-doped $BiFeO_3$ films

Composition	Method	Bottom electrode	Substrates	Temperature (°C)	$2P_r$ (μC/cm²)	E_c (kV/cm)	[ref]
$Bi_{0.92}Sm_{0.08}FeO_3$	CSD	Pt	$Pt/Ti/SiO_2/Si$	550	140	320	S. K. Singh et al.
$Bi_{0.90}Sm_{0.10}Fe_{0.97}Hf_{0.03}O_3$	PLD	$LaNiO_3$	$Pt/Ti/SiO_2/Si$	700	90	150	R. Agarwal et al.
$Bi_{0.90}Sm_{0.10}FeO_3$	PLD	$SrRuO_3$	$SrTiO_3$(100)	600	135	350	C.-J. Cheng et al.
$Bi_{0.90}Sm_{0.10}FeO_3$	PLD	$SrRuO_3$	$SrTiO_3$(100)	600	140	300	S. Fujino et al.
$Bi_{0.90}Sm_{0.10}FeO_3$	PLD	Pt(111)	Glass	450	150	420	this work

IV . CONCLUSIONS

- Grain size and surface roughness of BSFO films are reduced with increasing Sm content..
- BSFO thin films exhibit hardness in the range of 7.7-10.1 GPa and Young's modulus of 154.6-167.5 GPa. The result suggests that nanomechanical properties can be improved with smaller grain size.
- Ferroelectric properties are sensitive to microstructure, surface morphology, and Sm content. Enhanced ferroelectric properties with remanent polarizations ($2P_r$) of 66-150 μC/cm² can be attributed to flat surface, fine microstructure, and low leakage current.
- The BSFO films with x = 0.16 exhibits the P-E curve with a double hysteresis loop, possibly due to the induction of an orthorhombic phase.

Photocatalytic Properties of ALD-TiO_2-enclosed Gold Nanoparticle

Riza Ariyani Nur Khasanah[1,a], Ming-Chao Kao[1], Shien-Der Tzeng[2], Ing-Song Yu[3], Yen-Ping Peng[4], Min-Chieh Chuang[5], and Forest Shih Sen-Chien[1,b,*]

[1]Department of Physics, Tunghai University, Taiwan
[2]Department of Physics, National Dong Hwa University, Taiwan
[3]Department of Materials Science and Engineering, National Dong Hwa University, Taiwan
[4]Department of Environmental Science and Engineering, Tunghai Unversity, Taiwan
[5]Department of Chemistry, Tunghai University, Taiwan
[a]riza.Ariyani.n@mail.ugm.ac.id, [b,*]fsschien@thu.edu.tw

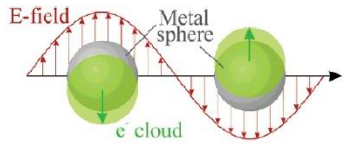

Supported by : Ministry of Science and Technology, Taiwan

Motivation

Au nanoparticle (AuNP) has surface plasmon resonance (SPR) effect, which can absorb the visible light to store as high-intensity plamonic energy. Hence, Nanocomposite of AuNP/TiO_2 and TiO_2/AuNP has been considered as a promising candidate for a photoanode or a photocathode to stimulate or enhance the visible photocatalytic water splitting. This research aims to study the photocatalytic properties of TiO_2/AuNP and finally we can propose the potential structure for photocatalytic water splitting.

Materials and Method

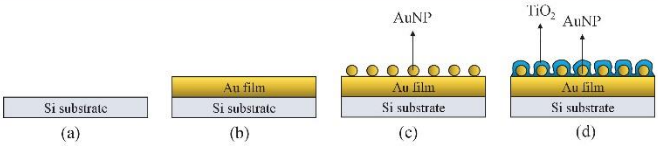

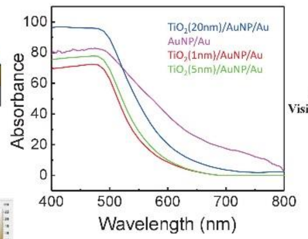

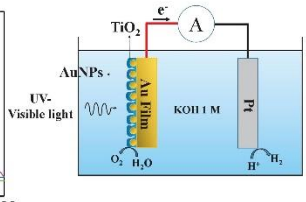

Preparation of sample:

- The deposition of Au thin film by sputtering for bottom contact (1 cm x 1 cm).
- The assembly of AuNP layer on Au thin film.
- The atomic-layer-deposition growth of conformal TiO_2 thin film to enclose AuNP layer.

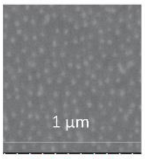

SEM image of TiO_2(1 nm)/AuNP/Au

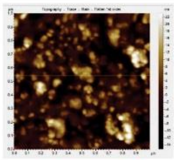

AFM image of TiO_2(1 nm)/AuNP/Au

- The coverage of AuNP = 15 %
- The diameter size of AuNP = 30 nm
- The thickness of TiO_2 = 1 nm, 5 nm and 20 nm

Electrochemical measurement
Instruments : Zahner Elektrik, Germany
Anode : sample
Cathode : Pt
Electrolyte : KOH 1 M (PH = 14)
Light source : AM 1.5 (1 sun)
532 nm laser (30 mW)

Results and Discussion

Photocurrent (V = 0) measured in 2 terminals under1 Sun AM 1.5 (left) and λ = 532 nm (30 mW) (right)

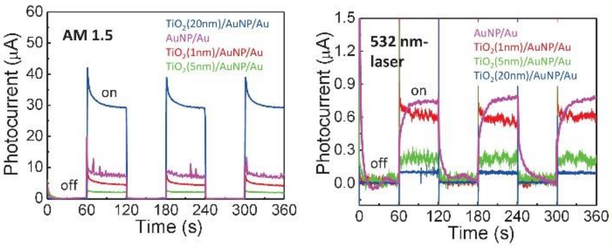

- Under 1 Sun AM 1.5, TiO_2(20 nm)/AuNP/Au has a highest current (30 µA) mainly due to the contribution of TiO_2 that absorbs UV light.
- Under 532 nm wavelength, AuNP/Au has the highest current (0.7 µA) due to the effect of SPR effect that absorbs the wavelength of 532 nm. TiO_2(1nm)/AuNP/Au has the similar current which is mainly also due to SPR effect.
- For TiO_2/AuNP/Au, the photocurrent under 532 nm decreases as the thickness of TiO_2 increases. It is contradictive to the absorbance. The presence of TiO_2 limited the light absorption of AuNP to 532 nm.

Cyclic Voltammetry of different structure (left) and different thicknesses of TiO_2 (right) measured in 3 terminals (reference : Ag/AgCl)

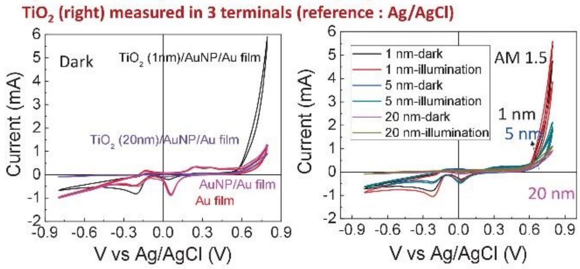

- The CV behaviors of TiO_2/AuNP/Au and AuNP/Au consist of gold oxide formation (0.2 V) and it's corresponding reduction (0.01 V), oxygen reduction to produce hydroperoxyl (-0.2 V) and it's corresponding oxidation (-0.1 V), water oxidation to produce O_2 (>0.6 V) and H^+ reduction to produce H_2 (predicted <-1 V).
- The onset potential of TiO_2(1nm)/AuNP/Au is lowest (0.6 V). So, it is potential to be a good photoanode.
- The CV behavior of AuNP/Au is similar to Au film. It is predicted that the sample is good as a photcathode, but needs more negative bias

Conclusions

TiO_2(1 nm)/AuNP/Au has more advantages than the other samples which potential to be a good photoanode due to the lowest onset potential. Although the photocurrent under AM 1.5 (1 sun) is very small, but it can enhance the light absorption under visible light due to SPR effect.

Influence of Absorption Transition in Electrical Properties of Perovskite Solar Cell

Asmida Herawati,[†] *Forest Shih-Sen Chien,*[*,†] *Shun-Hsiang Chan,*[‡] *Guan-You Lin,*[†] *Tsong-Shin Lim,*[†] *and Ming-Chung Wu*[*,‡,§]

[†] *Department of Applied Physics, Tunghai University, Taichung 40704, Taiwan*
[‡] *Department of Chemical and Materials Engineering, Chang Gung University, Taoyuan 33302, Taiwan*
[§] *Division of Neonatology, Department of Pediatrics, Chang Gung Memorial Hospital, Linkou, Taoyuan 33305, Taiwan*

Motivation

The emerging organometal halide perovskites (e.g., $CH_3NH_3PbI_3$, $MAPbI_3$) have intensively studied in recent years because of its excellent optoelectronic property, e.g. wide visible range absorption spectra. The incident photon-to-current efficiency of $MAPbI_3$ exhibits four peaks, which can be related to the absorption transitions between the multiple energy levels of $MAPbI_3$.[7, 9] That are 1.5 (T_1), 2.3 (T_2), 2.8 (T_3), and 3.5 (T_4) eV in Figure 1. [1] The influence of the absorption transitions to the properties of PSCs was investigated by the impedance response of PSCs and photo luminance.

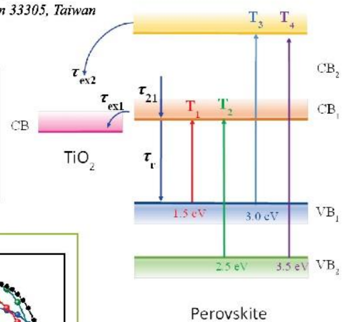

Figure 1. The absorption transitions to the properties of PSCs was investigated

Methods

The PSCs consisted of FTO/dense TiO_2/meso-TiO_2/$MAPbI_3$/spiro-OMeTAD/Ag . The impedance spectroscopy was performed with LCR meter (Hioki 3522-50 LCR HiTESTER). Fluorescence was collected using an objective (10x, 0.4 N.A, Olympus) and detected by an avalanche photodiode (SPCM-AQR-15-FC, PerkinElmer) with a 720 nm long pass filter.

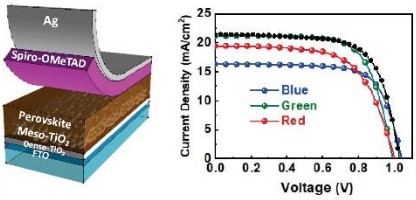

Figure 2. (a) Device structure of PSC. Figure 2. Spectral absorbance of MAPbI3 layer (b) and EQE of the PSC

Results and Discussions

Photo-induced charge density strongly depends on the wavelength of excitation (Figure 3).

In Figure 4 (a), Rp exhibits a linear relationship with F_{ph}, as the photoconductance of perovskite layer[2] and Cp remains almost constant so Rp and Cp are considered as the resistance and the capacitance of the perovskite layer.

In Figure 4 (b), the Cp of 405 nm is apparently higher than that of 532 nm and 650 nm, indicating the photocharges excited by T_3 experience a relaxation process significant from that by T_1 and T_2. Therefore the PL spectra excited with different wavelengths as a function of power density shown in Figure. 5.

Usually, it is considered that there are defects existing beneath CB1 and trapping the photoelectron excite electrons to CB1 by both T1 and T2. The probability of electrons trapped by low defects is the same, so PL excited by 532 nm and 632 nm exhibit similar intensities.

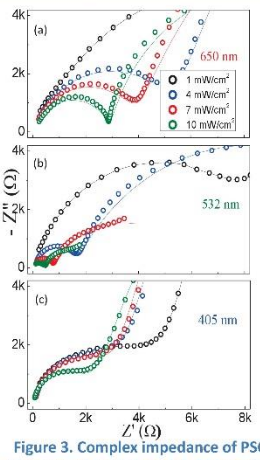

Figure 3. Complex impedance of PSC illuminated by 650 nm (a), 532 nm (b) and 405 nm lasers (c)

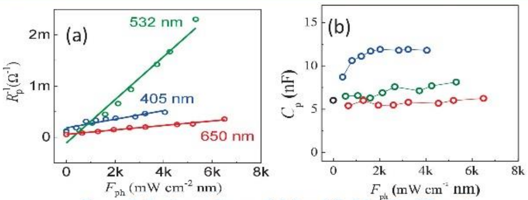

Figure 4. F_{ph} dependence of (a) and C_p (b) with different wavelengths. The lines in (a) are the linear fitting.

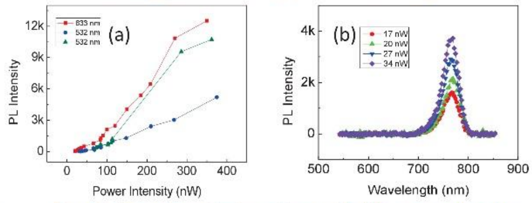

Figure 5. Power intensity dependence with different wavelengths excitation(a) and wavelength dependence of PL intensity (b) with 532 laser excitation

Conclusions

From the optical power dependence of the impedance, the perovskite layer exhibit a high photoconductance response to 532 nm excitation. From the optical power dependence of the impedance, the perovskite layer exhibit a high photoconductance response to 532 nm excitation. The increases of the trapped level will lower PL intensity excited by 405 nm . The integration intensity of 405 is remarkably lower than that 532 nm and 650. It indicates the relatively significant part of photocharges excited by 405 nm relaxes through the non-radiative process. We suggest there are trapping centers between CB1 and CB2.

Next Progress

1. Measure the time-resolved photoluminescence (TRPL) with different wavelength laser excitation to know the effect of absorption transition to the life time of Perovskite.
2. Analysis effect of trap in CB_1 and CB_2.

References

(1) Zhao, Y.; Nardes, A. M.; Zhu, K. Mesoporous Perovskite Solar Cells: Material Composition, Charge-Carrier Dynamics, and Device Characteristics. *Faraday Discuss.* **2014,** *176*, 301-312.
(2) Chu, Z.; Yang, M.; Schulz, P.; Wu, D.; Ma, X.; Seifert, E.; Sun, L.; Li, X.; Zhu, K.; Lai, K. Impact of Grain Boundaries on Efficiency and Stability of Organic-Inorganic Trihalide Perovskites. *Nat. Commun.* **2017,** *8*, 2230.

Acknowledgment

This work was supported by the Ministry of Science and Technology, Taiwan (MOST 105-2112-M-029-001-MY3 & 106-2221-E-182-057-MY3)

Structure, ferroelectric properties of $Hf_{0.5}Zr_{0.5}O_2$ films on the glass substrates

W.S. Wang(王惟萱)[1], C.R. Wang(王昌仁)[1], H.W. Change(張晃暐)[2]

[1]Department of Applied Physics, Tunghai University, Taichung 407, Taiwan
[2]Department of Physics, National Chung Cheng University, Chia-Yi 621, Taiwan

Introduction

Ferroelectric behavior based on HfO_2-based films has been reported in recent years due to the ferroelectric phase stabilized by a variety of dopants.
Owing to processing simplicity and silicon compatibility, this has attracted attention promising for non-volatile memory applications. Most work has been devoted on the epitaxial HfO films, but few study on the polycrystalline $(Hf,Zr)O_2$ films is available.
In this work, structure and ferroelectric properties of $Hf_{0.5}Zr_{0.5}O_2$ polycrystalline films with various oxygen pressures and substrate temperatures are studied.

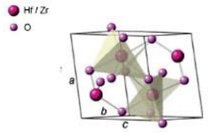

m-HZO

Experiment

Pulse Laser Deposition
Laser wavelength: 1064、532nm)

1064nm

50nmPt
40nm HZO(T°C)
20nmPt
Glass

1064、532nm

50nmPt
40nm HZO(x mTorr)
20nmPt
Glass

- Crystal structures: XRD
- Surface morphology: SEM
- P-E Curve: TF analyzer 2000
- M-H Curve: VSM

Result and discussion

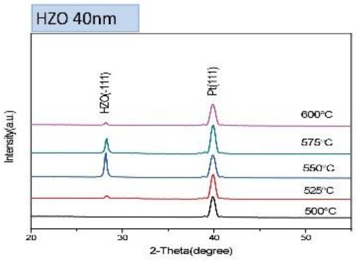

Fig. 1. XRD patterns of HZO thin films on Pt/glass substrate with oxygen pressures of 100mTorr at various temperatures of 500-600℃. (The wavelength of laser is 1064nm)

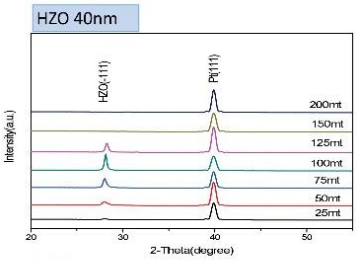

Fig. 2. XRD patterns of HZO thin films on Pt/glass substrate with various oxygen pressures of 25-200mt at temperature of 550℃. (The wavelength of laser is 1064nm)

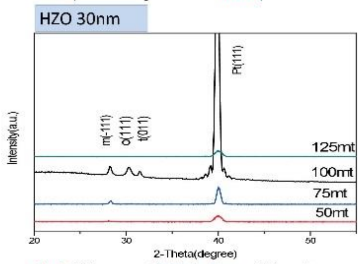

Fig. 3. XRD patterns of HZO thin films on Pt/glass substrate with various oxygen pressures of 50-125mt at temperature of 550℃. (The wavelength of laser is 532nm)

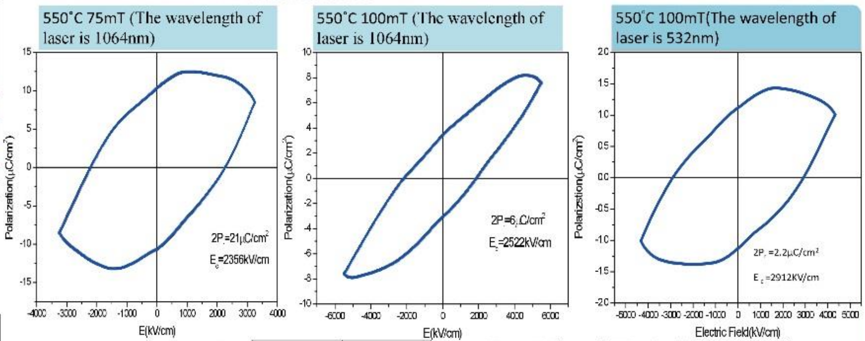

Fig. 4. PE loops of HZO thin films on Pt/glass substrate at temperature 550℃.

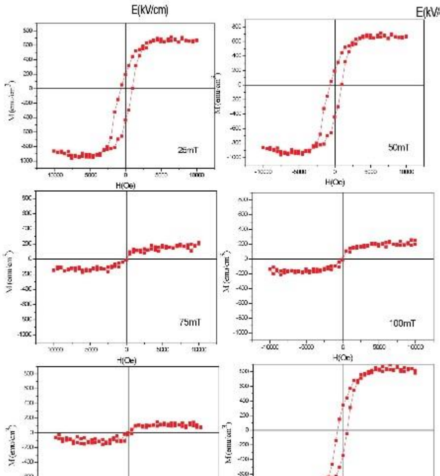

Fig. 5. M-H curves of HZO thin films on Pt/glass substrate with various oxygen pressures of 25-200mTorr at temperature 550℃.

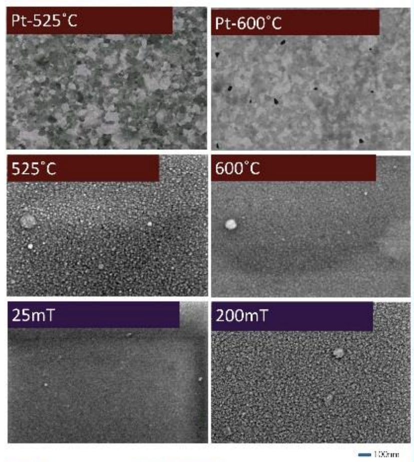

Fig. 6. SEM images of HZO thin films on Pt/glass substrate with oxygen pressures of 100mTorr at various temperatures of 525、600℃ and the various oxygen pressures of 25、200mTorr at temperature 550℃.

Conclusons

- A monoclinic ($\bar{1}11$) texture is detected for HZO films at 550 °C within oxygen pressure in the range of 50-125 mtorr and at 525-600 °C within oxygen pressure of 100 mtorr.
- A orthorhombic (111) and tetragonal (011) texture is detected for HZO films at the wavelength of laser is 532nm.
- Microstructure analysis show uniformly fine microstructure with small grain size is observed for all studied HZO films, and the size of HZO grains is increased from 10 nm at 525 °C to 25 nm at 600 °C.
- Magnetic is found at 25 mtorr, 50 mtorr and 200 mtorr.
- Ferroelectricity is found at 75 mtorr and 100 mtorr, their $2P_r$ are about 21and 6μC/cm², respectively.

Magnetic and nanomechanical properties of sputtered CoFe/MnN films

T.L. Chen[1], M.Y. Lee[1], C.R. Wang[1], H.W. Chang[2]

[1]Department of Applied Physics, Tunghai University, Taichung, 407 Taiwan

[2]Department of Physics, National Chung Cheng University, Chia-Yi, 621 Taiwan

Introduction

Exchange bias is a phenomenon that mainly exists at the interface between ferromagnetic and antiferromagnetic interfaces, resulting in a shift in the hysteresis curve and an increase in the coercive field. Since it can be utilized in spintronic components and giant magnetoresistance, it is currently attracting attention.

MnN conforms the good antimagnetic condition:

1. **Temperature stability, T_b ↑.**
2. **High Néel temperature, 660 K.**
3. **Exchange bias and coercive fields, $H_{EB} > H_C$.**
4. **Environmental safety and price.**

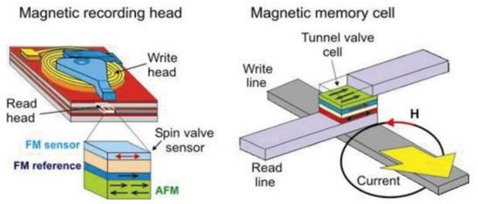

Experiment

Ta(5nm) / CoFe(5nm) / MnN(t_{nm}) / Ta(5nm) / SiO_2/Si(100)

→ **Field cooling**

F-C from 80℃ to RT at H=1 kOe

Magnetic property VSM

Crystal structure XRD

Surface morphology AFM

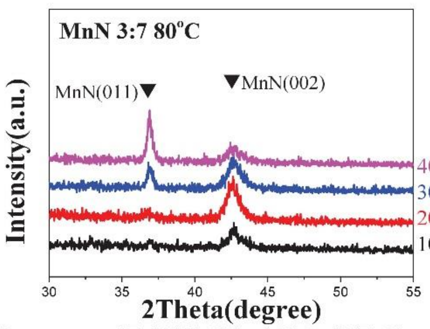

Fig 1. XRD patterns of Ta(5)/MnN(tnm)/CoFe(5)/Ta(5) annealed at 80 ℃ for 15 min.

Results and Discussion

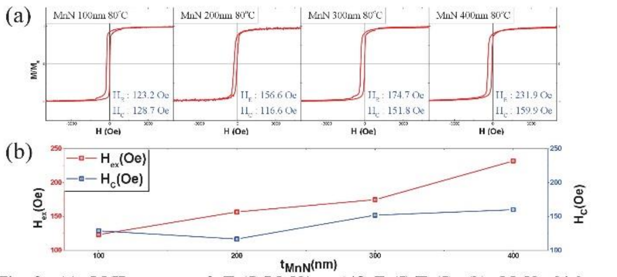

Fig 2. (a) M-H curves of Ta(5)/MnN(t_{nm})/CoFe(5)/Ta(5) (b) MnN thickness dependences of H_{ex} and H_C annealed at 80 °C for 15 min within applied magnetic field of 1 kOe.

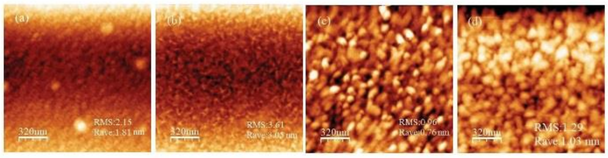

Fig 3. Surface morphology of Ta(5)/MnN(t_{nm})/CoFe(5)/Ta(5) annealed at 80℃ for 15 min within applied magnetic field of 1 kOe: (a) t=100 (b) t=200 (c) t=300 (d) t=400.

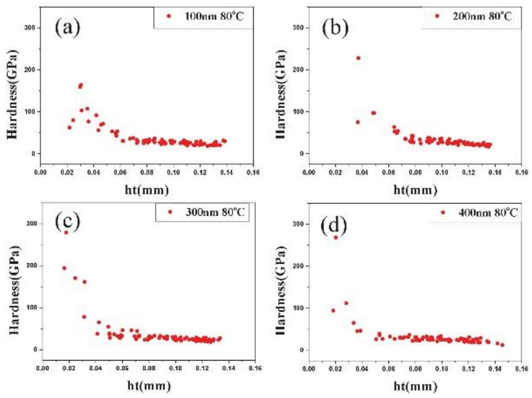

Fig4. The depressing depth dependences of hardness for different thickness (a) 100nm (H=19.5GPa) (b) 200nm (H=20.8GPa) (c) 300nm (H=22.9GPa) (d) 400nm (H=20.7GPa) of MnN annealed at 80℃ for 15 min within applied magnetic field of 1 kOe.

Conclusions

- **MnN texture can be tuned by thickness.**

(002) texture is obtained for MnN thickness of 100-200 nm, and is gradually transformed into (011) with increasing MnN thickness. MnN (011) texture is attained for 400 nm.

- **The texture evolution with thickness has influence on magnetic and nanomechanical properties.**
- **CoFe/MnN with (011) texture exhibits larger exchange bias.**
- **The hardness of MnN (011) is harder than MnN(002).**
- **They may be related to planar density of structure.**

Exchange bias in CoFe/MnN polycrystalline films on SiO_2/Si(100) substrates

Y.H. Chien[1], H.W. Chang[2], C.R. Wang[1], Lance Horng [3]

[1] Department of Applied Physics, Tunghai University, Taichung, 407 Taiwan.
[2] Department of Physics, National Chung Cheng University, Chia-Yi, 621 Taiwan
[3] Department of Physics, National Changhua University of Education, Changhua 500, Taiwan.

Introduction

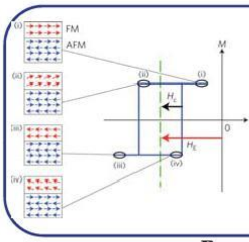

- In studied exchange bias systems, MnN exhibited higher Néel temperature (660K) and lower cost.
- It crystallizes in the θ phase of the Mn-N phase diagram, which has the tetragonal face-centered with a = 4.256 and c = 4.189 Å at room temperature (RT).
- In this study, CoFe/MnN and MnN/CoFe films are prepared on SiO_2/Si(100) substrates by sputtering at room temperature (RT).

Experiment

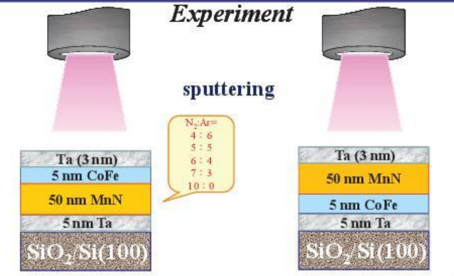

Crystal structures by XRD

Magnetization curve by AGM

Results and Discussion

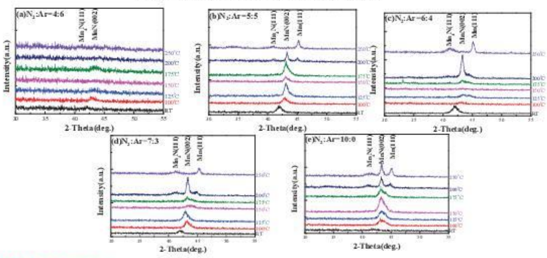

Fig.1. XRD patterns of CoFe/MnN layers with various sputtering atmosphere N_2:Ar of MnN and different annealing temperatures.

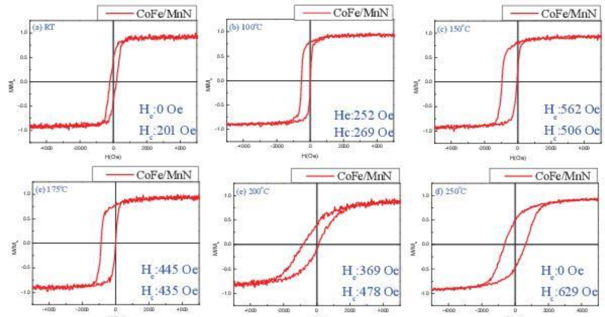

Fig.2. Magnetic hysteresis loops of CoFe/MnN layers with sputtering atmosphere N_2:Ar=5:5 of MnN at different annealing temperatures.

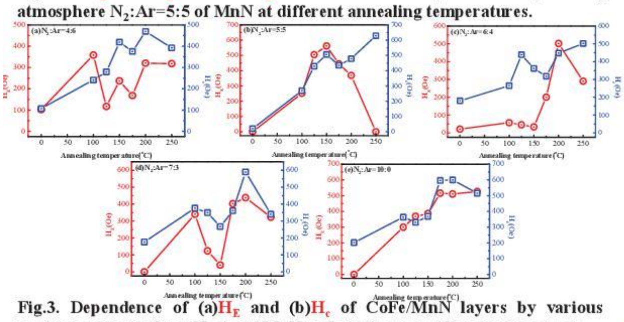

Fig.3. Dependence of (a)H_E and (b)H_c of CoFe/MnN layers by various sputtering atmosphere N_2:Ar of MnN and various annealing temperatures.

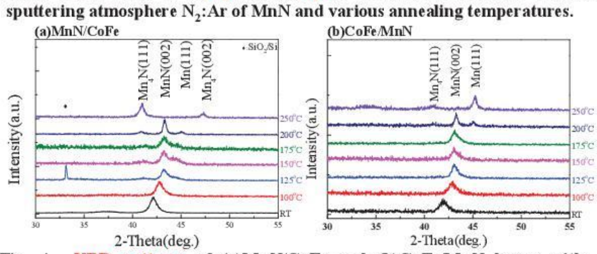

Fig. 4. XRD patterns of (a)MnN/CoFe and (b)CoFe/MnN layers with different annealing temperatures.

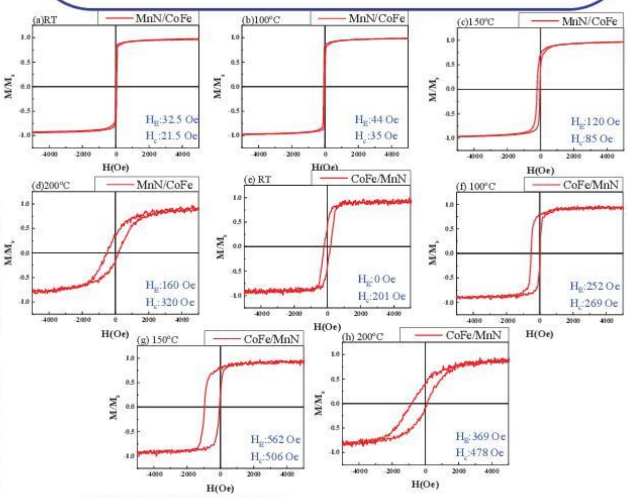

Fig.5. Magnetic hysteresis loops of (a)-(d)MnN/CoFe and (e)-(h)CoFe/MnN layers with different annealing temperatures.

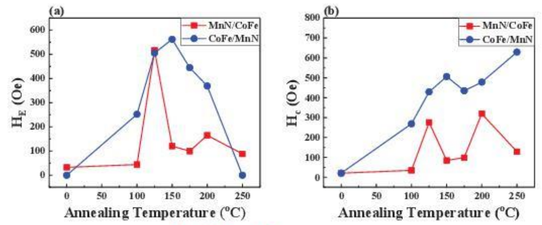

Fig.6. Dependence of (a)H_E and (b)H_c of MnN/CoFe and CoFe/MnN films by various annealing temperatures.

Conclusions

- The largest H_{eb} of 562 Oe is obtained in the presented Ta/CoFe/MnN/Ta films by sputtering at the room temperature followed by post annealing at 150 °C.
- High interfacial exchange energy of 0.47 mJ/m² attained for CoFe/MnN films in this study is comparable to M. Meinert et al. (0.41 mJ/m²).
- In CoFe/MnN films, better H_E is found for MnN prepared at N_2:Ar=5:5.
- At high annealing temperature, MnN(002) phase is transformed into Mn_4N(111) and Mn(111) phase, related to N disffusion during annealing.
- Compared to MnN/CoFe, CoFe/MnN films exhibit higher H_E at annealing temperature 150℃ .
- This study provides useful information to fabricate exchange bias CoFe/MnN system.

Optimization of exchange bias in Co / MnPt system

Y.C. Chen[1], H.W. Chang[2], C.R. Wang[1], Lance Horng[3]

[1] Department of Applied Physics, Tunghai University, Taichung, 407 Taiwan.

[2] Department of Physics, National Chung Cheng University, Chia-Yi, 621 Taiwan

[3] Department of Physics, National Changhua University of Education, Changhua 500, Taiwan.

Introduction

MnPt, an antiferromagnetic (AF) intermetallic alloy with a very high Néel temperature T_N ~ 973 K, has attracted much attention due to the potential applications in sensors, magnetic random access memory (MRAMs), read heads, and advanced spintronic devices.

In this study, Ta/Co/MnPt films are prepared on SiO2/Si(100) substrates at room temperature (RT) by sputtering at the external magnetic field of 1 kOe. The samples are annealed at designated temperature, and then cooling to RT at the applied magnetic field of 2 kOe. Ta underlayer effect on microstructure and magnetic properties of MnPt/Co are studied.

Experiment

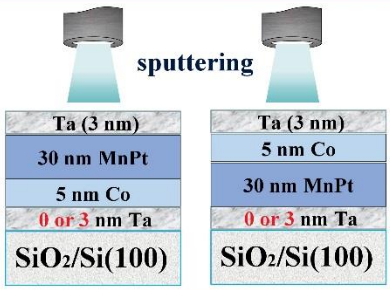

Film prepared by Sputter

Crystal structures XRD

M-H curve VSM

Surface morphology AFM

Results and discussion

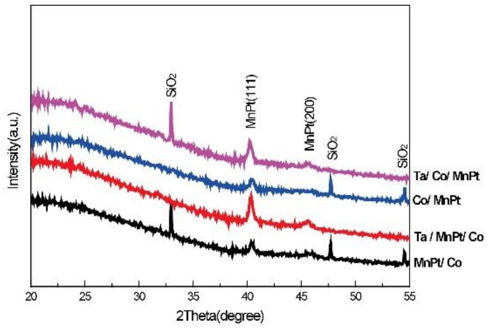

Fig1. X-ray diffraction patterns of SiO_2/Ta(0 or 3nm)/Co(5nm)/MnPt(30nm) and SiO_2/Ta(0 or 3nm)/MnPt(30nm)/Co(5nm) annealed at 250℃ for 1hr.

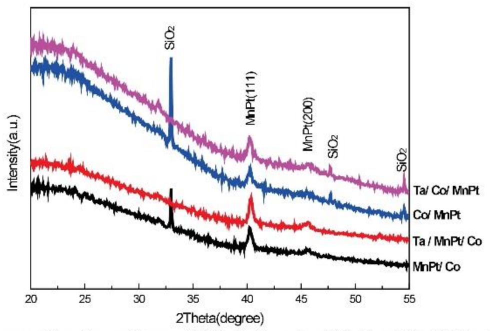

Fig2. X-ray diffraction patterns of SiO_2/Ta(0 or 3nm)/Co(5nm)/MnPt(30nm) and SiO_2/Ta(0 or 3nm)/MnPt(30nm)/Co(5nm) annealed at 275℃ for 1hr.

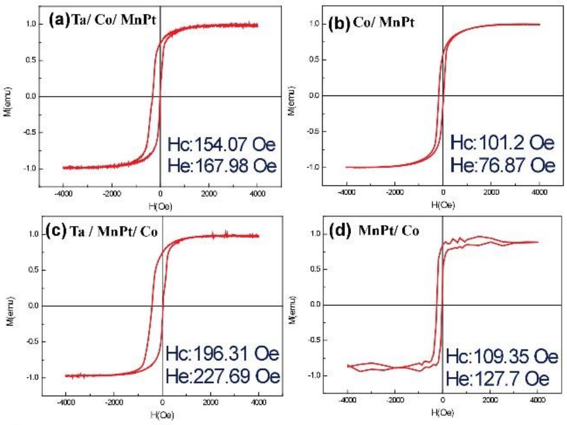

Fig3. M-H loops of the (a) SiO_2/Ta(3nm)/Co(5nm)/MnPt(30nm); (b) SiO_2/Ta(0nm)/Co(5nm)/MnPt(30nm);(c)SiO_2/Ta(3nm)/MnPt(30nm)/Co(5nm); (d) SiO_2/Ta(0nm)/MnPt(30nm)/Co(5nm) annealed at 250℃ for 1hr.

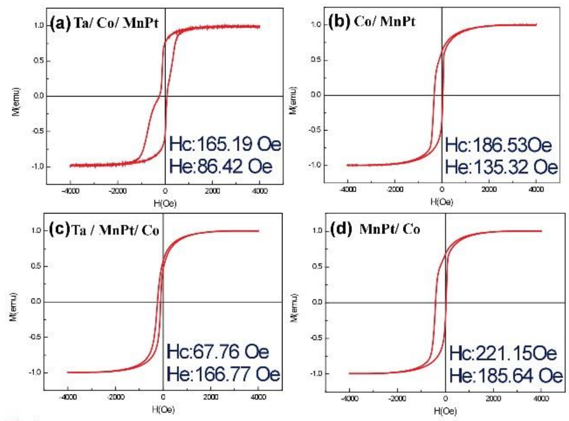

Fig4. M-H loops of the (a) SiO_2/Ta(3nm)/Co(5nm)/MnPt(30nm); (b) SiO_2/Ta(0nm)/Co(5nm)/MnPt(30nm); (c) SiO_2/Ta(3nm)/MnPt(30nm)/ Co(5nm); (d) SiO_2/Ta(0nm)/MnPt(30nm)/Co(5nm) annealed at 275℃ for 1hr.

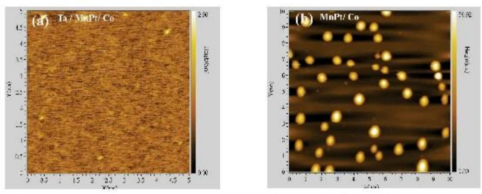

Fig5. AFM images of the studied films annealed at 275 ℃ with various thickness of Ta underlayer (a) 3 nm and (b) 0 nm.

Conclusions

- Magnetic properties of Co/MnPt and MnPt/Co bilayer systems with Ta underlayer annealed at various temperatures are studied.
- Ta underlayer is effective in flattened the interface and therefore reduced coercivity (H_c).
- At the same annealing temperature, the exchange bias field (H_e) of MnPt/Co is always larger than Co/MnPt system.
- This study provides useful information to optimized MnPt-based exchange bias system.

Wolff algorithm on Ising model

Zhang Yu-Hua (張宇華) Ng Kwai-Kong (吳桂光)

Abstract

In this paper I numerically study the two dimensional Ising model using the Monte Carlo method. I first introduce the Monte Carlo method with the importance sampling and Markov process, then I show the deferent between the single-spin-flip dynamics and wolff algorithm to simulate the Ising model in 2d square lattice , and thought the autocorrelation function to compare the efficiency of both the Metropolis–Hastings and Cluster Some of the programming details are also presented. Finally the simulated results are analyzed and discussed.

Ising model

伊辛模型是個簡易模型，自旋分佈為周期性點陣。在一維二維三維空間中等間距分佈。每個晶格點都有自旋（spin）σ（σ=±1）。我们可以通过某些算法制造Markov process。然后通过蒙地卡罗方法对晶格spin进行翻转从而达到模拟晶格不同状态的目的。我們先構造一個二維的伊辛模型。

为了創造一个好的Markov process.我們找到兩種處理狀態變化的方法

(1)Isingle-spin-flip dynamics
1.從系統中隨機抽取一個spin
2.計算翻轉后的能量變化量（ΔE）
3.以某一接受率（Acceptance Ratio） $P_A(\Delta E)$來決定是否進行翻轉
4.重複N次，N為晶格大小。

(2)Wolff算法
1.是隨機選擇一spin進行翻轉
2.然後看這個spin周圍（不包括對角線）有沒有同方向的。
3.如果沒有就回到步驟1.
4.如果有則以某概率加入cluster然後將整個cluster進行翻轉。
5.然後重複此步驟N次，N為晶格大小（低溫情況下翻轉過於頻繁因此選擇當翻轉spin總數等於N時就停止次步驟）。

Metropolis接受準則為：$P_A(\Delta E) = \min[e^{-\beta(\Delta E)}, 1]$
Wolff算法的Cluster接受率為:$p = 1 - e^{-2\beta J}$

T=2 T=2.5 T=4

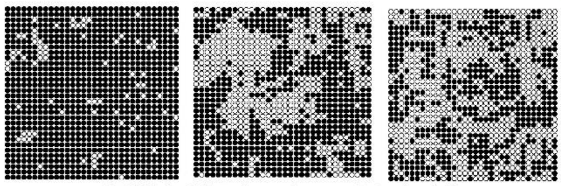

不同溫度下的32*32 Ising model spin 分佈

居里溫度T_C=2/ln(1+√2)≈ 2.2692。耦合常數 J = −1 （鐵磁）。當溫度較高時，spin排列比較混亂。當溫度從高到低接近居里溫度時同方向spin成片聚集，越過居里溫度時，大部分spin為同方向排列。Spin由排列由混亂到有序，是明顯的相變現象。因爲外加場h=0，所以我們看到模型是產生自發對稱性破缺

Analysis and Results

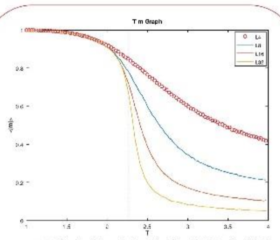

Wolff算法的磁化強度隨溫度變化

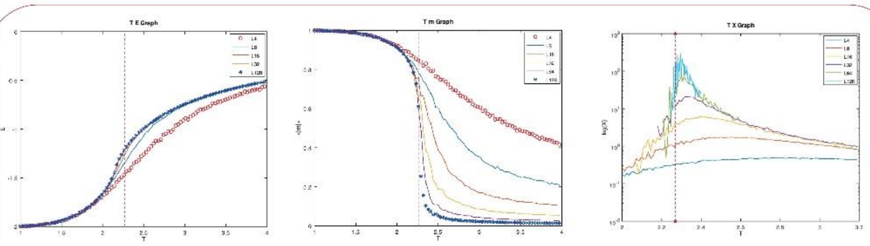

single-spin-flip dynamics的能量、磁化強度、磁化率隨溫度變化係

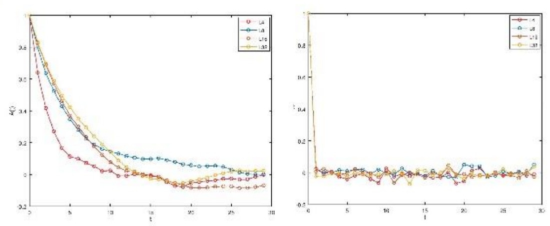

左圖是的single-spin-flip dynamics的autocorrelation function 。
右圖是Wolff算法。溫度T=3，L為晶格大小
可以看出Wolff算法的autocorrelation function下降速度要比single-spin-flip dynamics 快的多。

reference

[1].张志东，伊辛模型的研究进展简介，Chinese Journal of Nature，Vol.30 No.2：98-101；

[2].Newman MEJ, Barkema GT, "Monte Carlo Methods in Statistical Physics, Clarendon Press, 1999
[3]. Monte Carlo simulations in classical statistical physics Anders W. Sandvik, Department of Physics, Boston University;
[4]. Hastings, W.K. (1970). "Monte Carlo Sampling Methods Using Markov Chains and Their Applications".

Summary and perspectives

Wolff算法的翻轉效率要比single-spin-flip要高，在高溫時波動更小。但是低溫時計算冗餘，因此可以在低溫和平衡溫度時採用single-spin-flip，在靠近臨界溫度時再使用Wolff算法。

Ferroelectric properties of $BiFeO_3$ films on glass substrates with CoPt/Pt buffer layers

M.L. Chen(陳孟霖)[1] , C.R. Wang(王昌仁)[1]and H.W. Chang(張晃暐)[2]

[1]Department of Applied Physics, Tunghai University, Taichung 407, Taiwan
[2]Department of Physics, National Chung Cheng University, Chia-Yi 621, Taiwan

Introduction

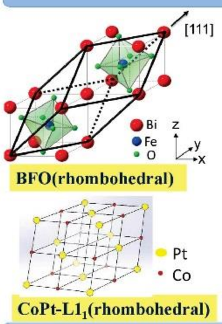

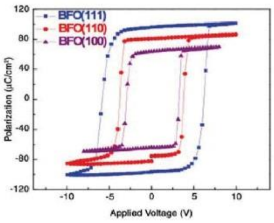

(111)-texture BFO films with high polarization

Experiment

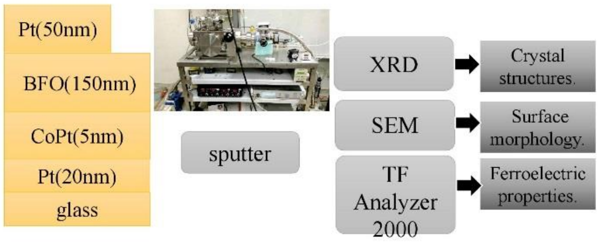

Results and discussion

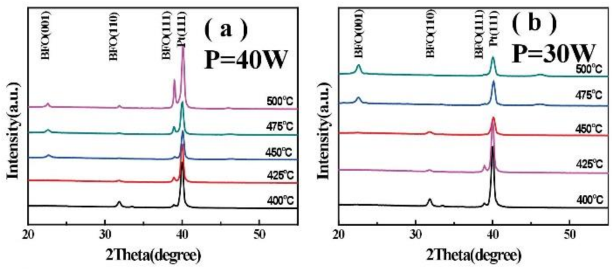

Fig.1. XRD patterns of BFO(200 nm)/CoPt (5 nm)/Pt(20 nm)/glass at (a)P=40W and (b)P=30W deposited at various temperatures.

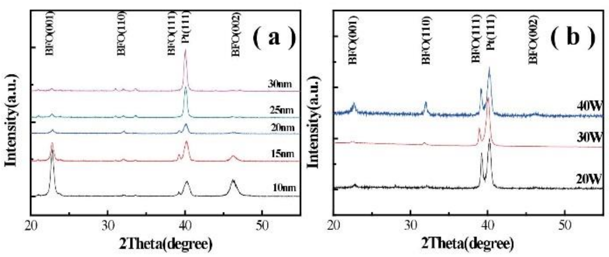

Fig.2. XRD patterns of (a)BFO(200 nm)/CoPt (5 nm)/glass at P=40W deposited at different Pt thickness and (b)BFO(200 nm)/CoPt (10nm) /Pt(20nm)/glass at 500℃ deposited at different powers.

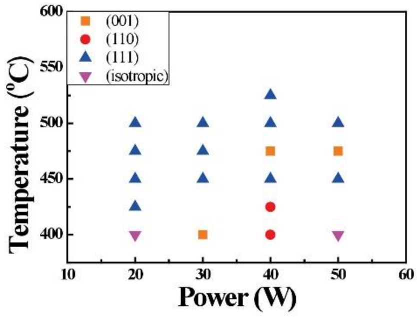

Fig.3. Phase diagram of the textures for this studies 200 nm-thick BFO films.

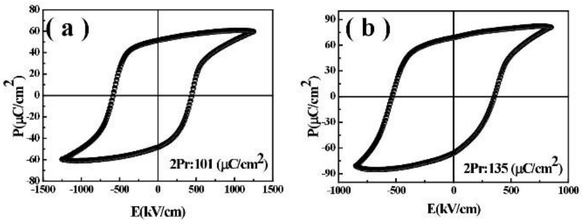

Fig.4. P-E loops of BFO(200nm)/ CoPt(x nm)/Pt(20nm)/40W at 500℃ (a)CoPt 5 nm and (b)CoPt 10 nm.

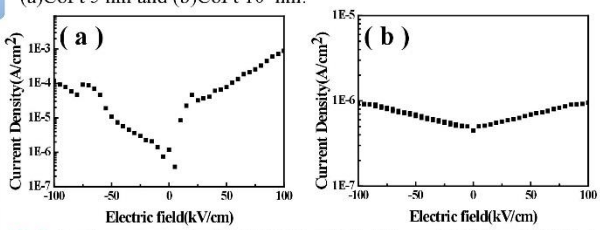

Fig.5. Leakage current of BFO(200nm)/ CoPt(x nm)/Pt(20nm)/40W at 500℃ (a)CoPt 5 nm and (b)CoPt 10 nm.

Conclusions

- **Textures of BFO films can be controlled by sputtering parameters and deposition temperature: (111) at P=40W and T=475-500 °C and P=20W and T=475-575 °C; (110) at P=40W and T=400 °C and P=30W and T=425-450 °C; (001) at P=30W and T=475-500 ℃, respectively.**
- **When the growth temperature is 500 °C, $2P_r$ = 101 μC/cm² at CoPt 5 nm is attained. Increase of CoPt thickness to 10 nm could further improve $2P_r$ to 135 μC/cm² due to low leakage.**
- **As a result, good ferroelectric properties can be obtained.**

Magnetic and nanomechanical properties of sputtered CoFe/MnPt films

P.C. Chen[1], H.W. Chang[2*], C.R. Wang[1*], Lance Horng[3]

[1] Department of Applied Physics, Tunghai University, Taichung, 407 Taiwan.

[2] Department of Physics, National Chung Cheng University, Chia-Yi, 621 Taiwan

[3] Department of Physics, National Changhua University of Education, Changhua 500, Taiwan.

Introduction

Exchange bias (EB), characterized by a shift of hysteresis loop originated from the interaction between the ferromagnetic (FM) and antiferromagnetic (AF) layers, is foundation for spin-valve (SV) based devices.

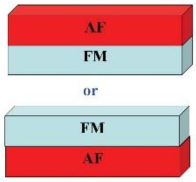

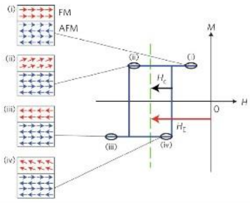

$L1_0$-MnPt advantage:

1. High T_N(975 K)
2. Large K_{AF} of 1.4×10^7 erg/cm^3
3. Excellent corrosion resistance

Applications

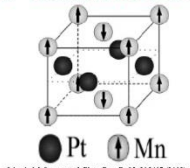

Marcio M. Soares et al. Phys. Rev. B. 85, 205417 (2012)

For the most device fabrication processes, the contact-induced damage may significantly affect the fundamental properties of the devices, and thus a quantitative assessment of the mechanical properties of materials is important.

Experiment

- MnPt layer in films are prepared by sputtering at the external magnetic field of 1 kOe induced from NdFeB sintered magnets and N_2 and Ar atmosphere.
- To obtain and align $L1_0$-MnPt, the samples are treated through field (1 kOe) cooling from 150-425 °C to RT.

Analysis:

Crystal structures by XRD	Surface morphology by AFM
nanomechanical by nanoindenter	Magnetization curve by AGM

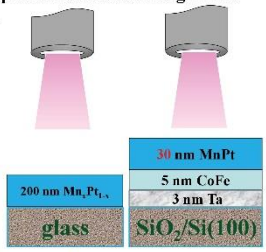

Results and Discussion

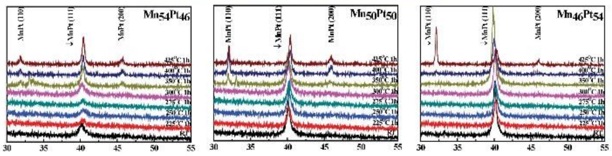

Fig.1. XRD patterns of Mn_xPt_{1-x}(x=54、50、46) film deposited with various annealing temperature.

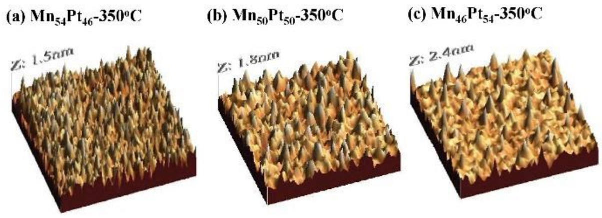

Fig.2. Surface morphologies of Mn100-xPtx thin film (x=54、50、46) at 350 °C.

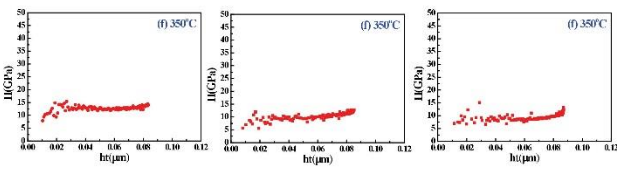

Fig.3. Hardness of $Mn_{100-x}Pt_x$ (x=54、50、46) films at 350 °C

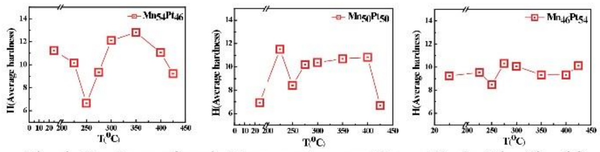

Fig. 4. Hardness of varied temperature on $Mn_{100-x}Pt_x$ (x=54、50、46) films.

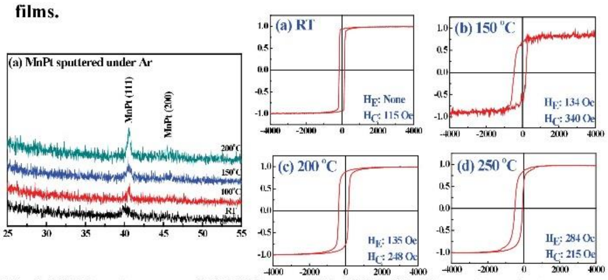

Fig.5. XRD patterns and M-H loop of Ta/CoFe/MnPt sputtered at Ar

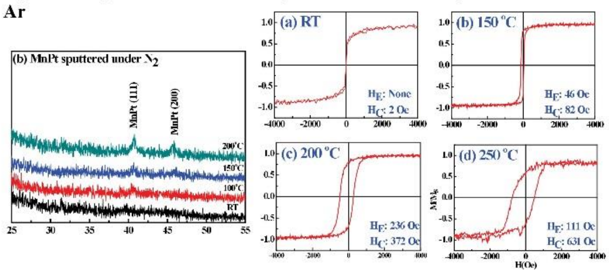

Fig.6. XRD patterns and M-H loop of Ta/Co/MnPt sputtered at N_2

Conclusions

- With increasing annealing temperature, MnPt is transformed from FCC to FCT($L1_0$).
- Two major factors taken into account to explain the nanomechanical properties with annealing temperature include reduced hardness by grain growth and enhanced hardness by the promotion of ordering of MnPt.
- Exchange bias of the films deposited at N_2 is lower than those prepared under Ar atmosphere probably due to poor crystallinity of MnPt.

Measuring the size of polymer spheres by small angle light scattering

Professor: Tsong-Shin Lim(林宗欣) Student: Wei-Yu Ku(古唯佑)
Department of Applied Physics, TUNGHAI UNIVERSITY, Taichung, Taiwan

Abstract

This study is to set up a small angle light scattering instrument to measure the sample size. We use polymer sphere to test. The light source is a He-Ne laser (wavelength λ = 543 nm). After passing through the sample, we use optical power meter horizontally moved to measure the optical power at each position, and each position and optical power meter are recorded to draw an One-dimensional intensity profile of the scattering. Then using the deduced formula to curve fitting and the radius of the polymer sphere is obtained. We used two different types of optical power meters for comparison, and used the results of the measurements to analyze the advantages and disadvantages of each of the two optical power meters.

Theory

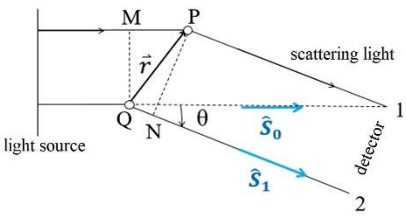

- When the light(wave vector direction $\hat{S}_0$) hits particles P, Q, it produces scattered light(we choose wave vector direction $\hat{S}_1$) . The scattered light has an angle θ with the direction of the light source. We call it the scattering angle.
- The two scattered lights will get to position 1 and position 2, respectively, and the phase difference between the two scattered lights is
$\Delta\varphi = \frac{2\pi}{\lambda}\Delta X = \frac{2\pi}{\lambda}\vec{r}\cdot(\hat{S}_0 - \hat{S}_1) = \frac{2\pi}{\lambda}\vec{r}\cdot\left(2\sin\frac{\theta}{2}\hat{k}\right)$, and $\hat{k} = \frac{(\hat{S}_0-\hat{S}_1)}{|\hat{S}_0-\hat{S}_1|}$
- We defined the scattering vector $\vec{q} = \frac{4\pi}{\lambda}\sin\frac{\theta}{2}\hat{k}$
- Two scattering light wave equations are $A_1(x,t) = A_0 b_p e^{\frac{2\pi}{\lambda}i(x-vt)}$, $A_2(x,t) = A_0 b_Q e^{\frac{2\pi}{\lambda}i(x-vt)} e^{-i\Delta\varphi}$
and we call b_i as scattering intensity factor.
- If there are N scattering particles, then $A_{total} = A_1 + A_2 + A_3 + \cdots + A_N$
The sum of all light intensity $I \propto A \cdot A^* = \sum_{n=1}^{N}\sum_{m=1}^{N} A_0{}^2 b_n b_m e^{-i\Delta\vec{r}_{mn}\vec{q}}$
- If it is a scattering of an area in a continuous substance
$$I = A_0^2 \int_{-\infty}^{\infty}\int_{-\infty}^{\infty} \rho(\vec{r}_m)\,\rho(\vec{r}_n) e^{-i(\vec{r}_n-\vec{r}_m)} d\tau d\tau'$$
and we call $\rho(\vec{r}_i)$ as scattering intensity density.
- If the continuous substance is a sphere of radius R and has a uniform scattering intensity density ρ
$$I \propto \frac{9[\sin(qR) - qR\cos(qR)]^2}{(qR)^6}$$

Experiment

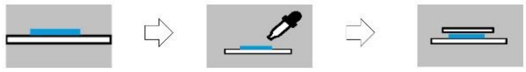

Put hybridization slide on the slide. → Add 25 μl of diluted 1/10 polymer sphere solution → Cover the coverslip

- The picture on the right shows the completed sample. The figure below shows two types of optical design. After laser passing through the sample, we put white paper behind the sample as the screen to view the image, or put the light sensor or an optical power meter to measured the light intensity.

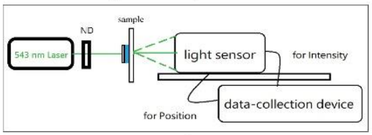

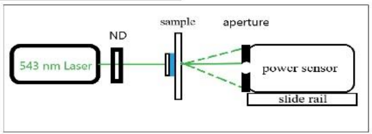

- The light sensor can change the different slit sizes to increase the resolution. We can use bottom rail manual movement sensor and measure the optical power at different positions.
- The data-collection device records the position of the light sensor and the corresponding optical power for analysis.
- The optical power meter can measure a wavelength range of 400 ~ 1100nm. Measured light intensity range from 5nW to 5mW

Results

- The image of the scattered light after the laser passes through the sample will be a bright circle around the circle, as shown in Figure 1 Figure 2 shows the size of the polymer sphere with an optical microscope. The radius of the polymer sphere is about 4.02 μm.

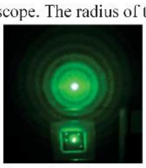

Figure 1 Imaging of scattered light on the screen (circle of 10 cm radius)

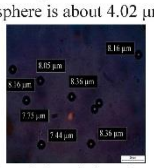

Figure 2 Sample imaging of optical microscope

- Fig. 3 (a)(b) show the results of the optical power meter and the light sensor to measure the intensity of the scattering light.
- We take the left and right peaks for curve fitting. The result of Fig. 3 (a) fitting is R=4.04 μm, as shown in Fig. 4 (a); the result of Fig. 3 (b) fitting is R= 4.19 μm and 4.04 μm, as shown in Fig. 4 (b).

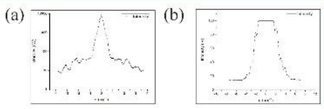

Figure 3 One-dimensional intensity profiles for the scattering for(a) power meter (b) light sensor

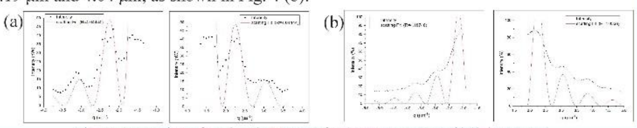

Figure 4 Drawing of peak enlargement for (a) power meter (b) light sensor

Conclusion & Discussion

- The optical power meter can provide a large dynamic range, but we cannot record it position immediately. The advantage of the light sensor module is that it can record the position and corresponding optical power immediately, but the dynamic range is small.
- The particle size of the polymer sphere obtained by the fitting is similar to the real size, but it can be seen from the one-dimensional intensity distribution of the scattered light that the results measured by the two optical power measurements are somewhat inconsistent with the theory.

Environmental Effects on Fluorescence Lifetime of Graphene Quantum Dots

Yung-Pin Chao (趙永斌)[1] and Tsong-Shin Lim (林宗欣)[1]
[1]Department of Applied Physics, Tunghai University, Taichung, Taiwan

Abstract

In this experiment, we want to discuss the effects of different environments on the fluorescence characteristics of graphene quantum dots (GQDs). We mixed polyvinyl alcohol (PVA) and agarose gel separately with GQDs to measure their fluorescence lifetime. From the results, we found that PVA and agarose gel will isolate GQDs from external molecules, thereby reducing the non-radiative transition of electrons due to reacting with oxygen, resulting in a larger fluorescence lifetime. PVA possesses hydroxyl groups and agarose gel without charge, which also causes a change in the radiation transition rate of GQDs and makes the fluorescence lifetime slightly different.

1. Introduction

Regular graphene has no band gap. Therefore, some scholars cut the graphene or graphene-related materials to quantum dots by some physical and chemical methods. Because of the quantum confinement effect and boundary effect cause the band gap in the GQDs to be opened. Therefore, we want to observe the changes in the fluorescence lifetime of GQDs in different environments from this experiment and explore what factors may be the fluorescent luminescence mechanism affecting GQDs.

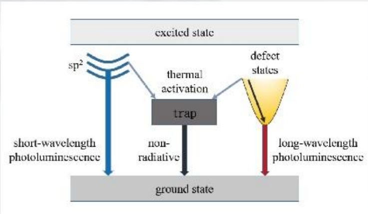

The principle of the fluorescence lifetime can be explained by the time excitons which stay in the excited states. The number of the excitons in the excited state is a function $n(t)$ related to the time t, and the number can be expressed by the following formula:

$$\frac{dn(t)}{dt} = (\Gamma + k_{nr})n(t),$$

Where Γ is the radiation transition rate and k_{nr} is the non-radiative transition rate. Then find the solution of the function $n(t)$ and get the formula:

$$n(t) = n_0 e^{(-t/\tau)},$$

Where n_0 is the number of excitons originally in the excited state, $\tau = (\Gamma + k_{nr})^{-1}$. As mentioned above, the average time that the exciton is in the excited state is the fluorescence lifetime, which can be seen from the average time of the fluorescence intensity decay. The formula is as follows:

$$< t >= \frac{\int_0^\infty tn(t)dt}{\int_0^\infty n(t)dt} = \frac{\int_0^\infty te^{(-t/\tau)}dt}{\int_0^\infty e^{(-t/\tau)}dt} = \frac{\tau^2}{\tau} = \tau,$$

It can be seen that the average time $< t >$ of the fluorescence intensity attenuation is equal to τ, so the average time $< t >$ of the exciton to be in the excited state can be defined as the fluorescence lifetime τ.

2. Experiment

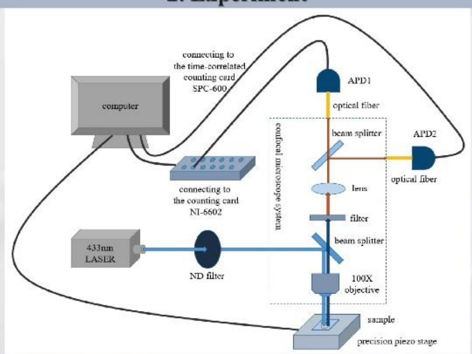

3. Result and Discussion

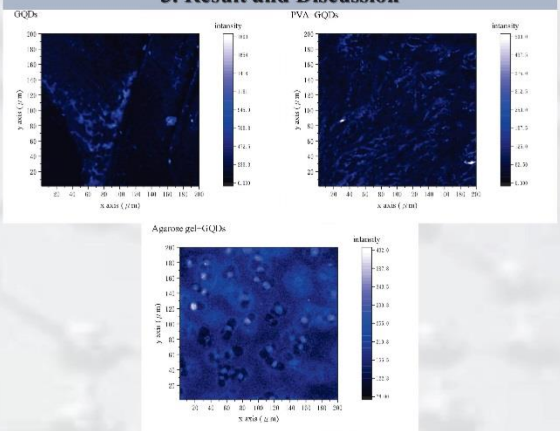

We can see that GQDs are more uniform in PVA, and GQDs in agarose gel are more agglomerated than the others. We suspect that PVA is a hydrophilic aqueous solution, which makes GQDs more uniform in PVA. However, agarose gel is also a hydrophilic aqueous solution, but after pumping and placing it in the dry cabinet, the GQDs that were originally homogeneous agglomerated in the gel due to the loss of water.

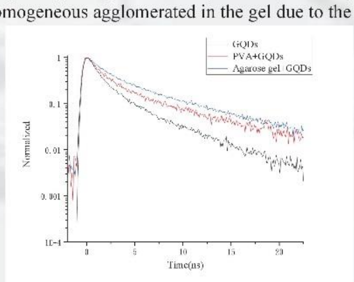

For the fluorescence intensity decay curve, we can use two exponential decay functions for fitting data. The formula is as follows:

$$y = A_1 e^{-t/\tau_1} + A_2 e^{-t/\tau_2} + y_0,$$

y_0 is the background noise, A_1 and A_2 are the amplitudes, and τ_1 and τ_2 are the decay time. Brought all of them into the formula to calculate the average lifetime $< \tau >$. The formula is as follows:

$$< \tau >= \frac{A_1{\tau_1}^2 + A_2{\tau_2}^2}{A_1\tau_1 + A_2\tau_1},$$

The average fluorescence lifetime of GQDs is about 1.13 ns, PVA+GQDs is about 1.35 ns, and agarose gel+GQDs is about 1.53 ns. We found that PVA and agarose gel will isolate GQDs from external molecules, and reducing the non-radiative transition of electrons generated by the reaction with oxygen. Therefore the non-radiative transition rate k_{nr} decreases, and making the fluorescence lifetime τ be larger. In addition, since PVA possesses hydroxyl groups and the agarose gel has no charge, this also affects the quantum state in GQD and affects the radiation transition rate Γ. Thus the fluorescence lifetime τ of GQDs in PVA and in agarose gel are slightly different.

4. Conclusion

- PVA and agarose gel will isolate GQDs from external molecules. Therefore reducing the non-radiative transition of electrons generated by the reaction with oxygen, and making the fluorescence lifetime larger.
- Since PVA possesses hydroxyl groups and the agarose gel has no charge that affects the quantum state in GQD, the fluorescence lifetime of GQDs in PVA and in agarose gel are slightly different.

Magnetic properties of Ta/$Ni_{80}Co_{20}$/Ta thin films with nitrogen implantation

D.Y. Lin[1], C.R. Wang[1], H.W. Chang[2], M.Y. Lee[1]

[1]Department of Applied Physics, Tunghai University, Taichung, 407 Taiwan

[2]Department of Physics, National Chung Cheng University, Chia-Yi, 621 Taiwan

Introduction

Permalloy NiCo films has high permeability resulted from high saturation magnetization. Compared with NiFe, NiCo has a higher coercive force, thus limiting its application.

N interstitialled into magnetically soft FeTa film by sputtering during N_2 atmosphere forms FeTaN phase and therefore reduces H_c has been reported.

In this work, NiCo films were deposited in a nitrogen atmosphere, and the structure and magnetic properties of Ta/$Ni_{80}Co_{20}$/Ta films are presented.

Experiment

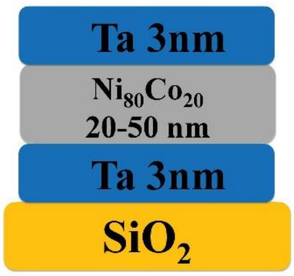

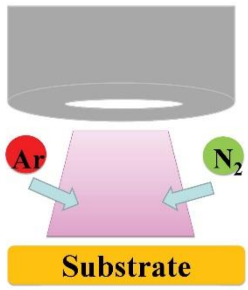

XRD
Structure

VSM
Magnetic properties

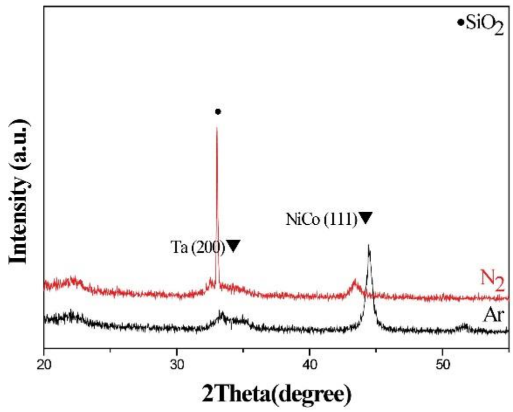

Fig.1 XRD patterns of $Ni_{80}Co_{20}$ film deposited under different atmospheres.

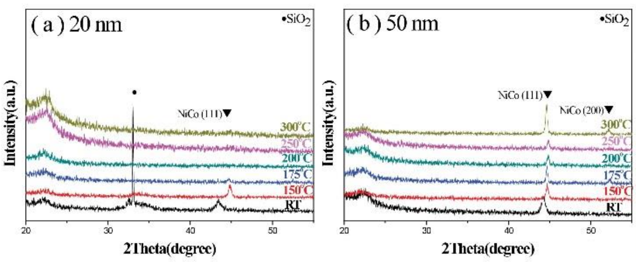

Fig.2 XRD patterns of the Ta/$Ni_{80}Co_{20}$/Ta films prepared annealed (a) 20 nm (b) 50 nm at 150°C-300°C.

Results and Discussion

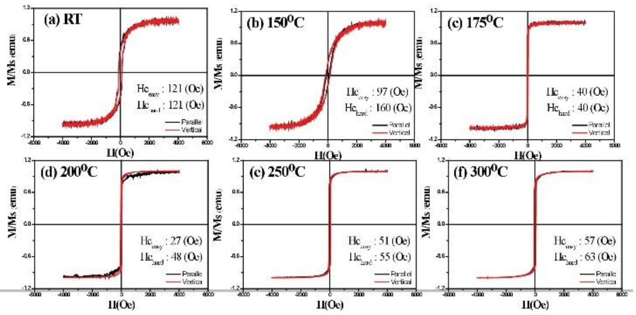

Fig.3 M-H loops of the Ta/$Ni_{80}Co_{20}$(20nm)/Ta films annealing temperature at (a) RT, (b) 150°C. (c) 175°C (d) 200°C (e) 250°C and (f) 300°C.

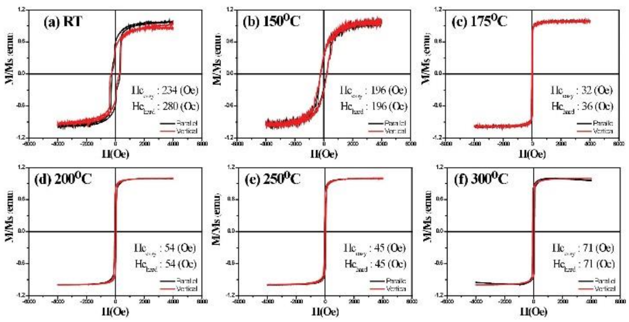

Fig.4 M-H loops of the Ta/$Ni_{80}Co_{20}$(50nm)/Ta films annealing temperature at (a) RT, (b) 150°C. (c) 175°C (d) 200°C (e) 250°C and (f) 300°C.

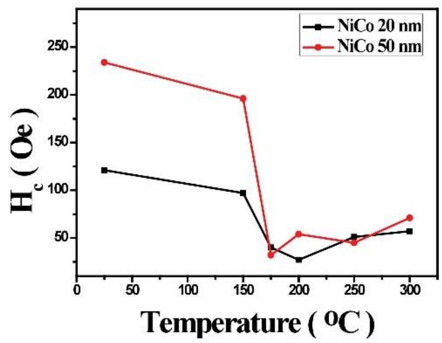

Fig.5 Coercivity at different annealing temperature in various thicknesses.

Conclusions

- Structure and magnetic properties of Ta/$Ni_{80}Co_{20}$/Ta films prepared in a nitrogen atmosphere with various thicknesses and annealing temperatures.
- The nitrogen has been successfully incorporated into the NiCo lattices, but they exhibited a higher coercivity.
- As the annealing temperature increases, the nitrogen is diffused out from the NiCo lattices, and therefore the coercivity is recovered to low.

A study on the deep-Q reinforcement learning

Chen Jia-Hui
Supervisor: Kwai-Kong Ng

Abstract: Computer is known for doing repeated boring work quickly. And now with algorithms of reinforcement learning, computer can learn and think as a human does. In this poster, a cart-pole agent, which managed to balance a pole attached to a cart controlled by the agent, is designed and implemented. The agent uses deep Q network, a method that combines artificial neural network and Q-learning.

Q-learning

Reinforcement learning is a kind of algorithm that agent understands nothing at the beginning. Then through continuous experimentation, the agent learns from numerous situations and master the best strategy to achieve the goal. Just like there is a mean virtual instructor, who don't teach how, but only rates your every action.

Q-learning is a model-free reinforcement learning algorithm. The goal of Q-learning is to learn a policy, which tells an agent what action to take under what circumstances. It does not require a model (hence the connotation "model-free") of the environment, and it can handle problems with stochastic transitions and rewards, without requiring adaptations.

$$Q^{new}(s_t,a_t) \leftarrow (1-\alpha)\cdot\underbrace{Q(s_t,a_t)}_{\text{old value}} + \underbrace{\alpha}_{\text{learring rate}}\cdot\overbrace{\left(\underbrace{r_t}_{\text{reward}} + \underbrace{\gamma}_{\text{discount factor}}\cdot\underbrace{\max_a Q(s_{t+1},a)}_{\text{estimate of optimal future value}}\right)}^{\text{learned value}}$$

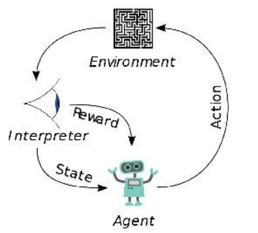

Fig. 1. typical framing of a Reinforcement Learning (RL) scenario

Artificial Neural Network

Artificial neural networks or connectionist systems are computing systems vaguely inspired by the biological neural networks and astrocytes that constitute animal brains. Such systems "learn" to perform tasks by considering examples, generally without being programmed with any task-specific rules.

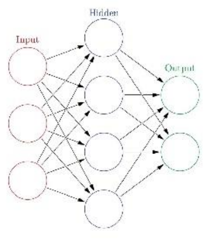

Fig. 2. An example of 3 layers deep neural network

Method

The environment used here is Cartpole-v1 from OpenAI Gym. There are 4 observations in the environment, which are cart position from -4.8 to 4.8, cart velocity from –inf to inf, pole angle from -24 deg to 24 deg and pole velocity from –inf to inf. Two actions are available in the environment which are push cart to the left and push cart to the right. At starting state, all observations are assigned a uniform random value between -0.05 and 0.05. Each training episode will end when pole angle is more than 12 degrees, cart position is more than 2.4 from the center or episode length is greater than 200. The agent is considered solving the cartpole problem when the average step is greater than or equal to 200.0 over 100 consecutive trials.

At first I simply built the agent with Q-table and it didn't learn anything after hundreds of episodes and the pole always fell immediately right after the start.

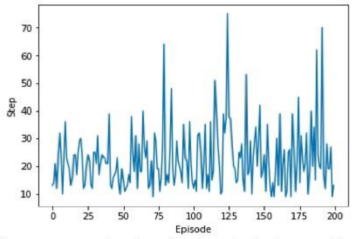

After consulting my supervisor I realized cartpole is a continuous problem and has numerous states, while Q-table stored every state it encountered and learned from these state, so it would take months or even years to train the agent.

The solution is to classify observation intervals into certain numbers, for example cart position between 0.25 and 0.75 will be assigned 0.5. This method lower the computation burden and the agent starts to last over 200 steps after 150 episodes. But there are still some glitches and agent can't last over 200 steps continuously.

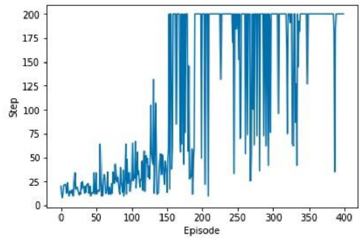

To make it better, I rebuild the agent with deep Q network, which replaces Q-table with neural network and experience replay in Q-learning. The agent masters and solves the problem after 62 steps.

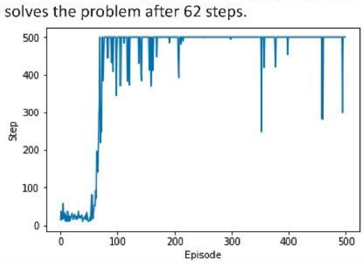

Optimization of exchange bias in IrMn/Co films

Y.R. Lai[1], C.R. Wang[1], H.W. Chang[2]

[1]Department of Applied Physics, Tunghai University, Taichung, 407 Taiwan

[2]Department of Physics, National Chung Cheng University, Chia-Yi, 621 Taiwan

Introduction

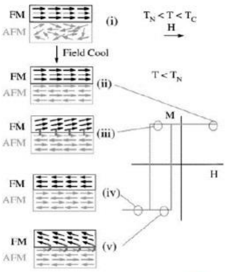

The advantages of IrMn :

1. *high Neel temperature (673K)*
2. *high J_k*
3. *good corrosion resistance*
4. *good thermal stability*

Experiment

sputtering

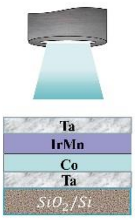

AGM *Magnetic properties*

XRD *Crystal structures*

AFM *Surface morphology*

Results and Discussion

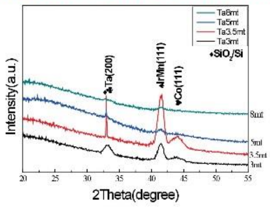

Fig.1. XRD patterns of the samples with different working pressure of Ta underlayer.

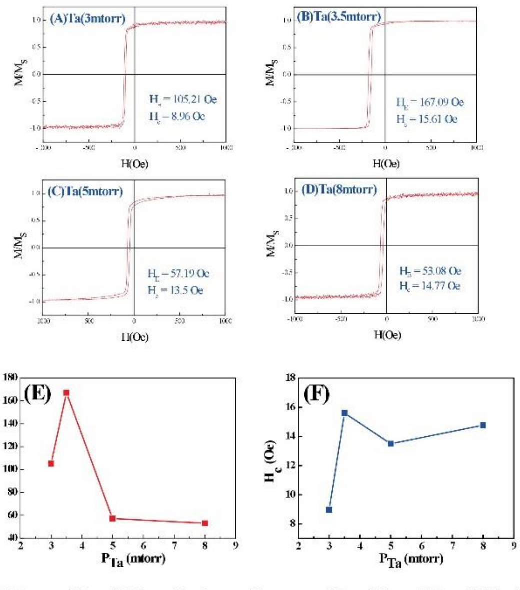

Fig.2 M-H curves of the studied films with various working pressure of Ta underlayers. (E)H_E and (F) H_c of the studied films with different working pressure of Ta underlayers.

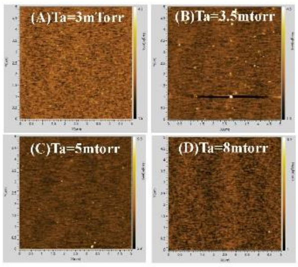

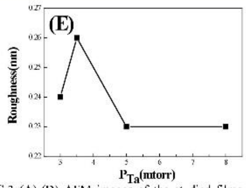

FIG.3 (A)-(D) AFM images of the studied films with various working pressure in Ta underlayers. (E) the root-mean-square roughness of the studied films with different working pressure of Ta underlayers.

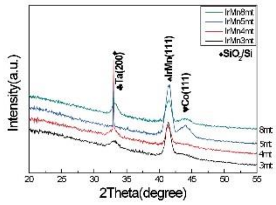

Fig.4. XRD patterns of the samples with various working pressures of IrMn layers.

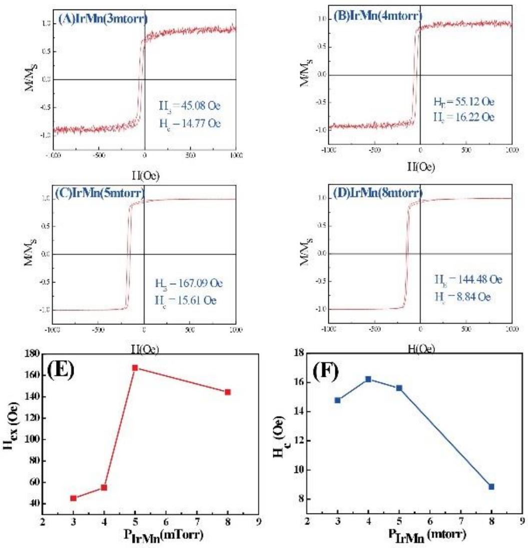

Fig.5 M-H curves of the studied films with various working pressure in IrMn films. (E)H_E and (F) H_c of the studied films with different working pressure of IrMn layer.

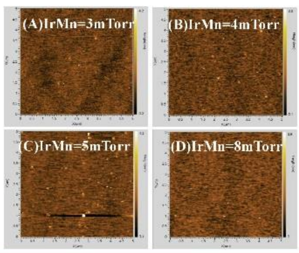

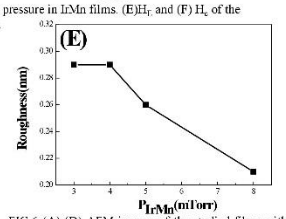

FIG.6 (A)-(D) AFM images of the studied films with various working pressure in IrMn fillms. (E) the root-mean-square roughness of the studied films with different working pressure of IrMn films.

Conclusions

- **In this study, higher H_E=167.1 Oe with small H_C=15.61 Oe for IrMn/Co/Ta film at P_{Ta}=3.5 mtorr at room temperature with strong IrMn(111) texture.**
- **The decrease of H_E at higher Ta working pressure related to weaker IrMn(111) texture.**
- **In this study, higher H_E for IrMn/Co/Ta film at P_{IrMn}=5 mtorr at room temperature with strong IrMn(111) texture.**
- **This study provides useful information to fabricate exchange bias system with Co as a FM layer and IrMn as an AF layer.**

Structure and ferroeletric properties of $BiFeO_3$ films on glass substrates with FePd underlayer

Y.J.Ciao(喬昱智)[1] , C.R. Wang(王昌仁)[1], and H.W. Chang(張晃暐)[2*]

[1]Department of Applied Physics, Tunghai University, Taichung 407, Taiwan
[2]Department of Physics, National Chung Cheng University, Chia-Yi 621, Taiwan

Introduction

- Why BFO??
- The ferroelectric properties of BFO films are highly related to the orientation, and the texture can be controlled by various sputtering parameters, doping elements, and the selection of the underlayer and substrates.
- The advantages of FePd include high magnetocrystalline anisotropy, high saturation magnetization, high T_C and good chemical stability.
- In this work, adopting ferromagnetic underlayer, FCT FePd, in order to obtain some magnetic and electrical properties with BFO coexist antiferromagnetic and ferroeletric .

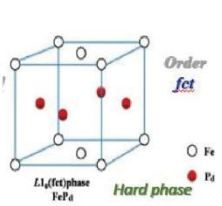

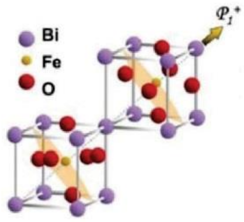

Experiment

Pt(50nm)	Pt(50nm)
BFO(200nm)	BFO(200nm)
FePd(50nm)	FePd(30nm)
Ta(5nm)	Ta(5nm)
glass	glass

XRD | TF 2000

Results and discussion

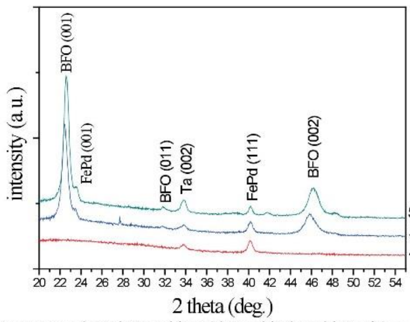

Fig1. XRD patterns of BFO(200nm)/FePd (30nm)/Ta(5nm)/40W/glass deposited at different temperatures.

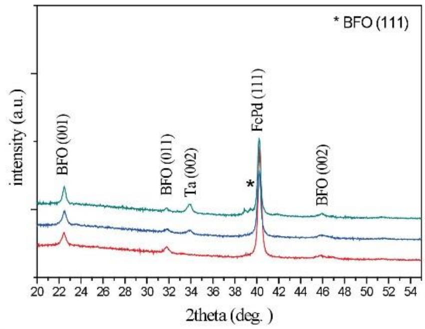

Fig2. XRD diffraction patterns of BFO(200nm)/FePd (50nm)/Ta(5nm)/40W/glass deposited at different temperatures.

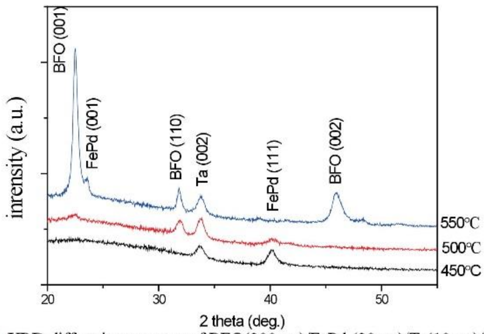

Fig3. XRD diffraction patterns of BFO(200nm)/FePd (20nm)/Ta(10nm)/40W/glass deposited at different temperatures.

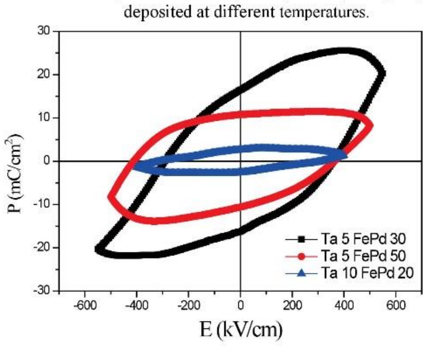

Fig4. P-E curves of BFO(200nm)/ FePd (30nm)/Ta(5nm)/40W at 500℃
BFO(200nm)/ FePd (50nm)/Ta(5nm)/40W at 500℃
BFO(200nm)/FePd (20nm)/Ta(10nm)/40W at 550℃

Conclusions

- **Increasing the temperature to 550℃ improves BFO(111) texture .**
- **Good ferroelectric properties with 2Pr=32.6 ($\mu C/cm^2$) are attained for BFO(200nm)/ FePd (30nm)/Ta(5nm)/40W at 500℃.**
- **The ferroelectric properties are related to the crystallinity and surface morphology.**

Coercivity enhancement of sputtered FePd thin films with Cu top-layer diffusion

P.H. Lin[1], M.Y. Li[1], C.R. Wang[1], H.W. Chang[2*]

[1] Department of Applied Physics, Tunghai University, Taichung

[2] Department of Physics, National Chung Cheng University, Chia-Yi, Taiwan

Introduction

- $L1_0$-FePd thin films is promising as a next generation high-density magnetic recording media and spin-MRAM.

Advantages : 1.Large K_u ~10^7(erg/cm³) 2.High T_C 3.Good chemical stability

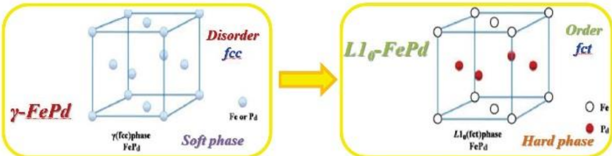

- FePd films deposited at room temperature followed by a rapid thermal annealing could lead to the phase transformation from the A1 to $L1_0$.
- However, the coercivity of the developed FePd films is normally low (< 1 kOe), though few literatures reported epitaxial FePd(001) films exhibit high coercivty of 6 kOe.
- We expect that Cu top-layer diffusion may improve coercivity of FePd films due to the magnetic isolation effect.
- In this work, effect of Cu top-layer diffusion on the coercivity of FePd films is studied.

Experiment

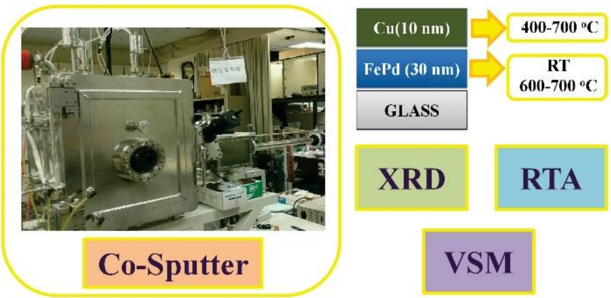

Result and Discussion

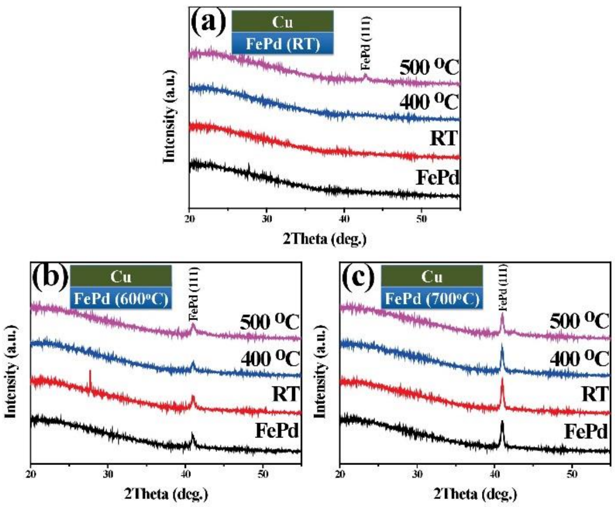

Fig.1 XRD patterns of FePd(RT～700 °C)/Cu(10 nm) films post annealed at various temperatures. (a) RT ; (b) 600 °C ; (c) 700 °C

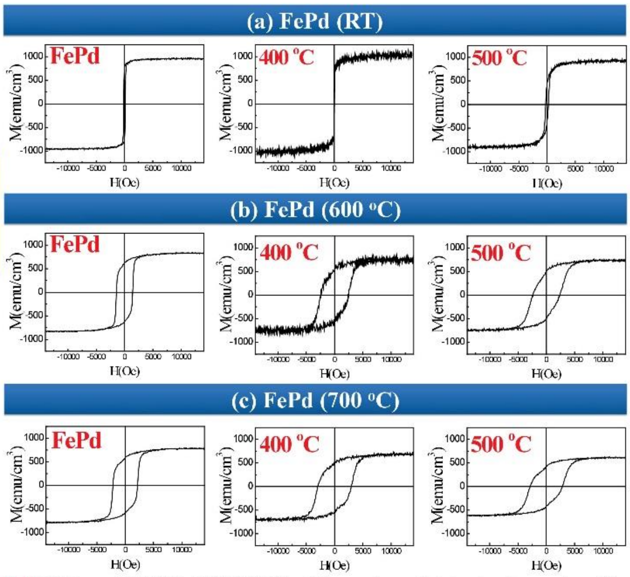

Fig.2 M-H loops of FePd(RT～700 °C)/Cu(10 nm) films post annealed at various temperatures. (a) RT ; (b) 600 °C ; (c) 700 °C

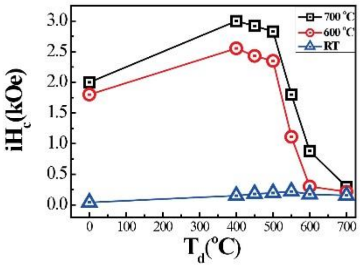

Fig.3 The relation chart(T_d - iH_c) of FePd(RT～700 °C)/Cu(10 nm) films post annealed at various temperatures.

Cu(10 nm)/ FePd 700 °C	M_s(emu/cm³)	M_r(emu/cm³)	H_c(Oe)
RT	780	610	2240
400 °C	750	595	3000
500 °C	670	450	2830

Fig.4 The data form of FePd(700 °C)/Cu(10 nm) films post annealed at various temperatures.

Conclusions

- Coercivity of sputtered FePd films with Cu top-layer diffusion are studied.
- XRD patterns showed that all studied FePd thin films have a preferred (111) orientation.
- With increasing annealing temperature, the phase transformation from the A1 to $L1_0$ for FePd films enhances the coercivity.
- Cu top-layer diffusion is effective in enhancing coercivity of FePd films with higher $L1_0$ degree, and the highest coercivity of 3000 Oe is achieved for FePd films annealed at 700 °C and then Cu(10 nm) diffused at temperature of 400 °C.
- Coercivity enhancement with Cu diffusion is related to the magnetic isolation effect of FePd grain with nonmagnetic Cu.

Magnetic properties of sputtered NiFe thin films with N interstitial

Y.S. Liu[1], D.Y. Lin[1], C.R. Wang[1], H.W. Chang[2]

[1]Department of Applied Physics, Tunghai University, Taichung, 407 Taiwan

[2]Department of Physics, National Chung Cheng University, Chia-Yi, 621 Taiwan

Introduction

Permalloy NiFe has received much attention due to high permeability resulted from high saturation magnetization and low coercivity and good anisotropic magnetoresistance.

In this work, NiFe films were prepared by sputtering at nitrogen atmosphere, and magnetic properties and structure of Ta/NiFe/Ta films with various thickness of NiFe layer annealed at various temperature are studied.

	$Ni_{80}Fe_{20}$	Ta
Structure (a)	FCC (0.355 nm)	FCC (0.331 nm)
Curie Temperature (°C)	400	-
Saturation Magnetization (kG)	10.8	-

Experiment

	DC
Thickness	20-100 nm
Annealing	100-300 °C

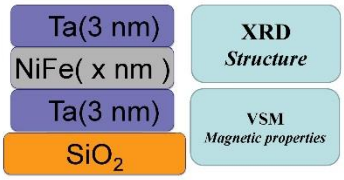

Results and Discussion

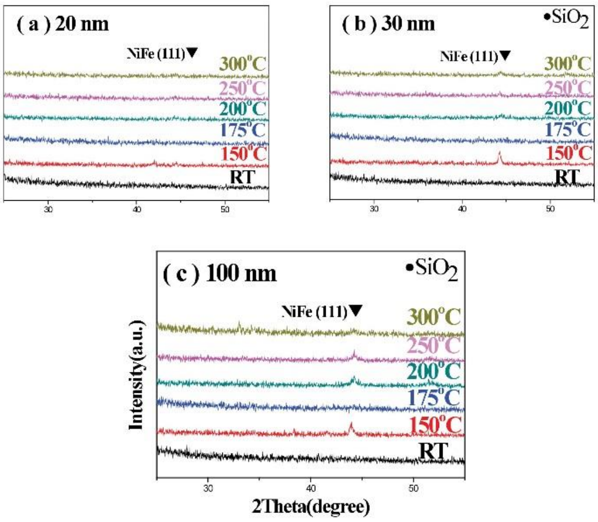

Fig.1 XRD patterns of the Ta/NiFe/Ta films prepared by (a) 20 nm (b) 30 nm and (c) 100 nm.

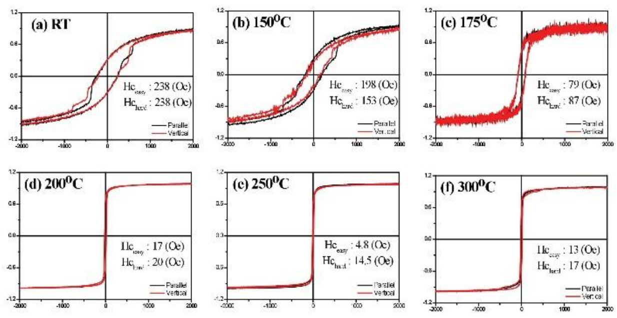

Fig.2 M-H loops of the Ta/NiFe(20 nm)/Ta films annealing temperature at (a) RT (b) 150°C (c) 175°C (d) 200°C (e) 250°C and (f) 300°C.

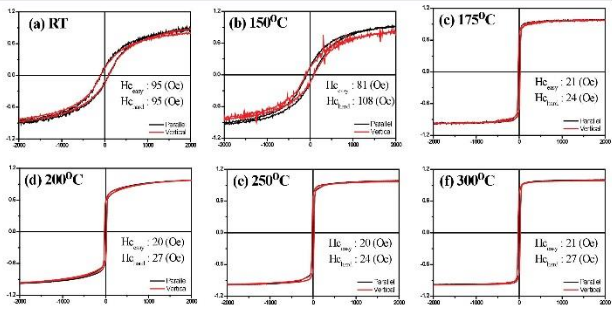

Fig.3 M-H loops of the Ta/NiFe(30 nm)/Ta films annealing temperature at (a) RT (b) 150°C (c) 175°C (d) 200°C (e) 250°C and (f) 300°C.

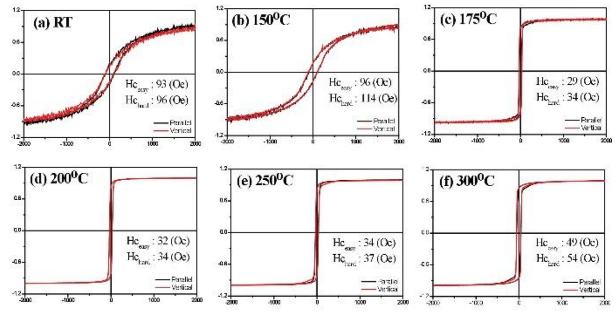

Fig.4 M-H loops of the Ta/NiFe(100 nm)/Ta films annealing temperature at (a) RT (b) 150°C (c) 175°C (d) 200°C (e) 250°C and (f) 300°C.

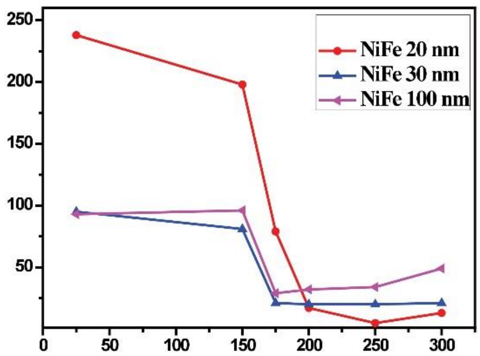

Fig.5 Coercivity at different annealing temperature in various thicknesses.

Conclusions

- Structure and magnetic properties of NiFe films prepared by DC sputtering with various thicknesses and annealing temperatures are studied.
- XRD result shows that NiFe(111) peak shifted to low angle for the films prepared at N_2 atmosphere indicates N interstitalled into NiFe lattice, and NiFe(111) peak toward high angle with increasing annealing temperature reveals N diffused out of NiFe lattice.
- N interstitalled into NiFe lattice leads to high coercivity, and N diffused out of NiFe results in recovery of coercivity to low value.

Magnetic properties of sputtered Co/OsMn films on the SiO_2/Si(100) substrates

C.Y. Hung(洪振瑜) [1], , C.R. Wang(王昌仁) [1], D.Y. Lin(林德育) [1], H.W. Chang(張晃暐) [2*]
[1]Department of Applied Physics, Tunghai University, Taichung, Taiwan
[2]Department of Physics, National Chung Cheng University, ChiaYi, Taiwan

Introduction

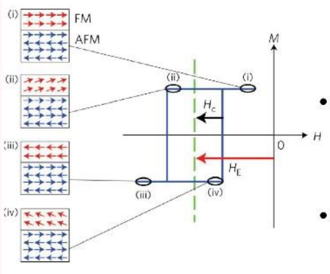

- **Theoretical calculations predict that the antiferromagnetic exchange interaction of Mn becomes stronger with decreasing 3d electron number at the Mn site.**
- **Therefore, it is expected that OsMn alloys may exhibit a higher Néel temperature than RhMn and IrMn alloys reported to have a very high Néel temperature.**
- **In this study, we explored the structure and magnetic properties of OsMn/Co films.**

Experiment

Crystal structures by XRD

Co-sputter

VSM

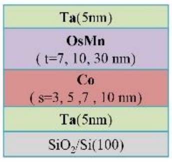

Results and discussion

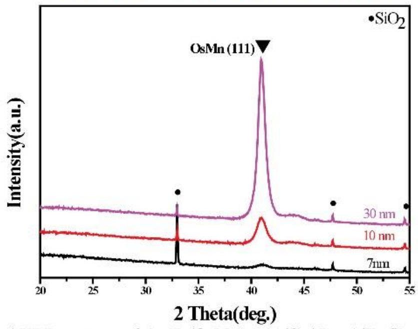

Fig.1 XRD patterns of the Ta/OsMn(t nm)/Co(5 nm)/Ta films prepared at various OsMn thicknesses of 7-30 nm.

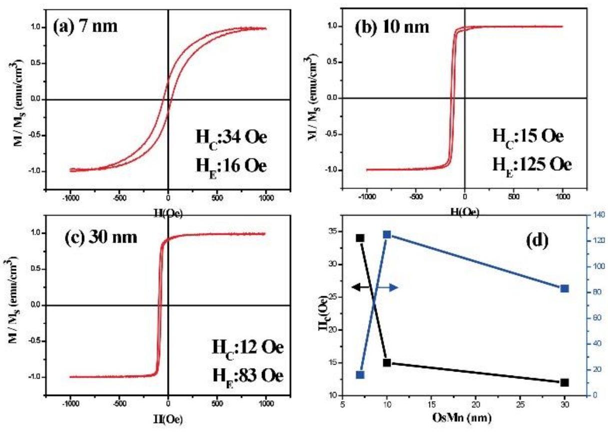

Fig.2 Magnetic hysteresis loops of the Ta/OsMn(t nm)/Co(5 nm)/Ta films prepared at various OsMn thicknesses (a)7 nm, (b)10 nm, (c)30 nm and (d)H_C and H_E in various OsMn thicknesses.

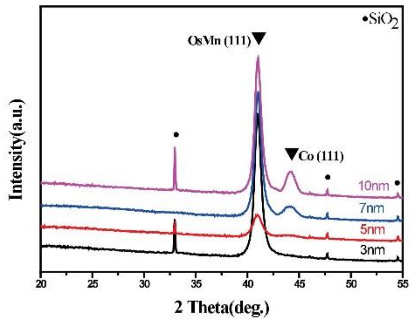

Fig.3 XRD patterns of the Ta/OsMn(10 nm)/Co(s nm)/Ta films prepared at various Co thicknesses of 3-10 nm.

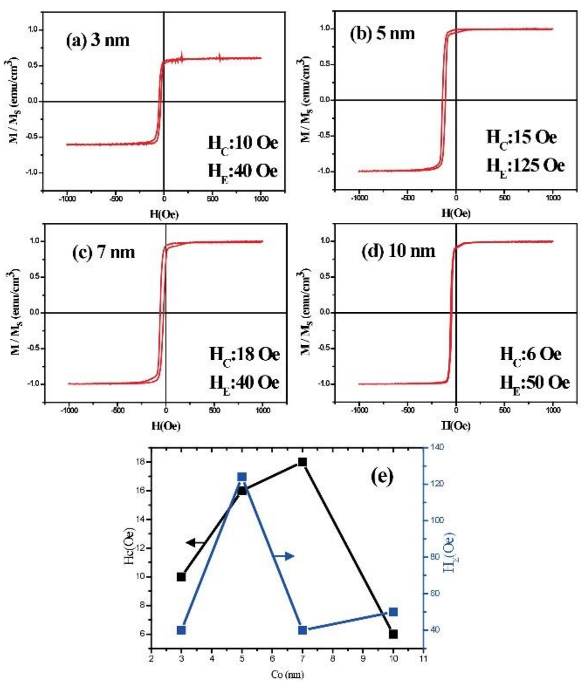

Fig.4 Magnetic hysteresis loops of the Ta/OsMn(10 nm)/Co(s nm)/Ta films prepared at various OsMn thicknesses of (a)3 nm, (b)5 nm, (c)7 nm,(d)10 nm (e)H_C and H_E in various Co thicknesses.

Conclusions

- **In this study, obvious exchange bias is found for OsMn/Co system.**
- **With increasing OsMn increases, the texture of OsMn(111) is promoted.**
- **When the thickness of OsMn increases, H_E has a tendency to rise first and then fall, and maximum value of H_E is 125 Oe at the OsMn thickness of 10 nm.**
- **When thickness of Co increases, H_E has a tendency to rise first and then fall, and the maximum H_E is 125 Oe at the thickness of Co 5nm.**
- **The increased exchange bias is related to stronger magnetocrystalline anisotropy of OsMn, and smooth interface between Co and OsMn.**
- **Further study is ongoing and needed.**

Study of shadow effect on flexible metal mask

Chih-Huang Liao (廖智偟) and Chia-Yi Huang (黃家逸)*
*chiayihuang@thu.edu.tw
Department of applied physics, Tunghai University, Taichung ,Taiwan

ABSTRACT

The evaporation has really great directivity, so the metal mask in vacuum thermal evaporation will cause the shadow effect, and the main substance of this paper is talk about how can we get the perfect graphics without the shadow effect by using the flexible metal mask in the vacuum thermal evaporation. We used the photolithography and sputter to make our metal mask, and try to find out the best level of bending to solve the shadow effect, if we can solve the shadow effect then we can do more application on it.

FABRICATION

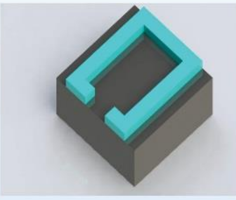

1.Area of PET substrate = 2 × 2cm^2
2.Photoresist = AZ400k
3.Spin-coating = 500 rpm, 10 sec
1000 rpm, 40 sec
4.Baking = 100 sec, 100˚C
5.Exposure time = 12~16 sec

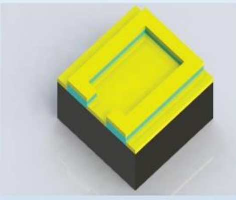

1. Silver deposition using sputter = 5hr

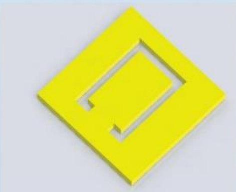

1.Development process = 2 hr

We leave the silver part as the metal mask

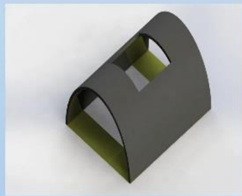

1.Area of PET = 4 × 4 cm^2
2.Cut a square hole in the middle
3.use PI tape sticky as shown as the picture

1.Put the metal mask on the mold which we made in previous step
2. Finally put in the evaporation

RESULTS

plane	flexible
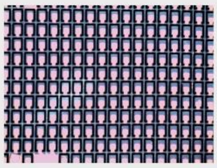	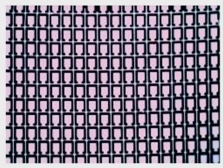

plane	
A little curve	
flexible	

CONCLUSION

We try three different way to test the line width by plane, a little curve, and flexible. And the results are flexible is better than former. Then we compare their shadow effect with the flexible and plane. As the result we can know that the plane is obviously have shadow effect more than the flexible one. In this study we find out that using the flexible metal mask for evaporation will have the better graphics than using the plane metal mask. Not only can solve the shadow effect, but also have more accurate line width.

ACKNOWLEDGMENTS

This research was financially supported by the Ministry of Science and Technology (MOST) of Taiwan under contract no. MOST 107-2112-M-029 -005 -MY3

東海大學

Liquid crystal elastomer: drives a motor with a chemical solvent

Yuxuan Lin(林宇軒), Chia-Yi Huang*(黃家逸)
Department of applied physics,Tunghai University, Taichung, Taiwan
*chiayihuang@thu.edu.tw

Abstract

Liquid crystal polymer (LCP) film is fabricated by a mixture of LC and polymer. The film is immersed into acetone and taken out from it. After acetone fully evaporates in the air, the film curves immediately. Experiment results depict that the curling rate of the LCP film increases with the immersion times and periods. These two factors can increase the degree of curling of the film.

Fabrication

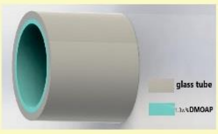

Glass tube alignment
(1) immerse the glass tube with a radius of 3.5mm and a length of 10mm in DMOAP solution.
(2) put it into the ultrasonic vibration machine for internal vibration.
(3) put them in the oven to dry it.

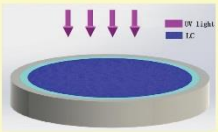

Make liquid crystal polymer film
(1) fill the liquid crystal in the glass tube and keep constant temperature
(2) continuing exposure to ultraviolet light to make the polymer polymerize
(3) wash the excess liquid crystal away

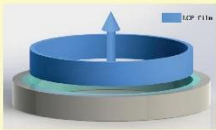

Take out the thin film
(1) immerse the sample in HF
(2) wait for the glass tube to dissolved and remove the film from the glass tube.

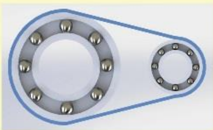

Assemble the motor
(1) combine the removed film with two bearings
(2) drop acetone on one side

Result

Figure 1. Curved liquid crystal polymer

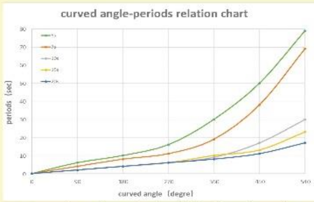

Figure 2. Dependence of curved angles of LCP film on immersion periods.

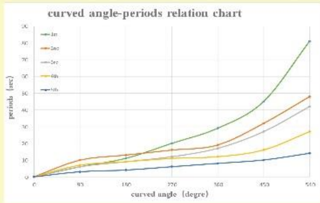

Figure 3. Dependence of curved angles of LCP film on immersion times.

Conclusions

After the acetone volatilizes on the LCP film, the ability of bending on LCP film decreased in a strong degree and finally become stable. However, the film will resume the straight strip shape again when it exposed to acetone again and begin to bend after acetone volatilizes again. Therefore , the LCP film can be reused. We can repeat the ability of curling and stretching of the film. We can let this work become a different kind of operation to drive the machine.

Acknowledgments

This research was financially supported by the Ministry of Science and Technology (MOST) of Taiwan under contract no. MOST 107-2112-M-029 -005 -MY3

Keywords: Liquid crystal, PDLC, organic solvent, chemical change

東海大學

Magnetic and nanomechanical properties of sputtered Co_3Pt thin films

Y.H. Liu (劉宇修)[1], P.Y. Yeh(葉朋佑)[1], C.R. Wang(王昌仁)[1], H.W. Chang (張晃暐)[2*],
[1] Department of Applied Physics, Tunghai University, Taichung, Taiwan
[2] Department of Physics, National Changhua University of Education, Changhua 500, Taiwan.

Introduction

Structure	Element	T_{order} (°C)	K_u (erg/cm³)	M_s (emu/cm³)	Lattice constant
$L1_2$	$CoPt_3$	600	7 x 10^7	520	a=0.3831
$L1_0$	CoPt	600	5x 10^7	850	a=b=0.3803 c=0.3701
$L1_1$	CoPt	200-400	3.5x 10^7	940	a=0.3801
m-$D0_{19}$	Co_3Pt	300-400	2x 10^7	1100	a=0.256 c=0.422

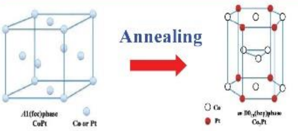

m-D019 Co_3Pt Applications:

- Magnetic memory
- Advanced spintronic devices

For the most device fabrication processes, the contact-induced damage may significantly affect the fundamental properties of the devices, and thus a quantitative assessment of the mechanical properties of films is important.

Experiment

- CoPt films prepared by RF magnetron sputtering at room temperature.
- Various post annealing temperature (300 to 800 °C).

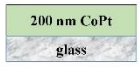

Analysis:

Crystal structures by XRD	Magnetization curve by AGM
Nanomechanical properties nanoindenter	Surface morphology by AFM

Results and discussion

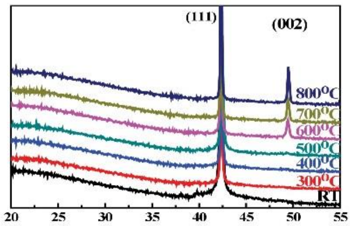

Fig. 1. XRD patterns of CoPt thin film grown on glass substrate. Results show that Co_3Pt thin films are predominant (111)-oriented, indicative a well ordered microstructure.

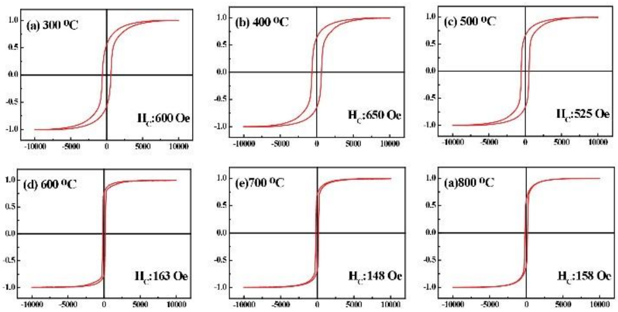

Fig. 2. M-H curves of 200-nm-thick $Co_{65}Pt_{35}$ thin films grown on glass substrate with various annealing temperature at (a) 300 °C (b) 400 °C (c) 500 °C (d) 600 °C (e) 700 °C (f) 800 °C.

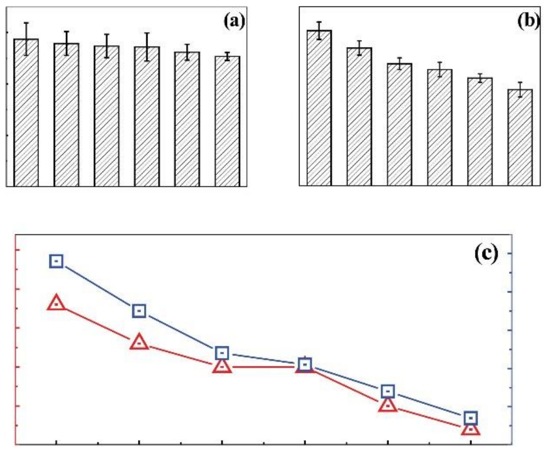

Fig. 3. (a)- (c) Young's modulus and Hardness of Co_3Pt film with various annealing temperatures

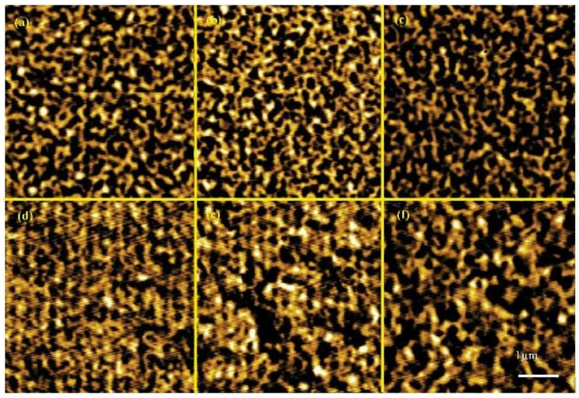

Fig. 4. MFM images of CoPt thin films grown on glass substrate annealed at (a) 300 °C (b) 400 °C (c) 500 °C (d) 600 °C (e) 700 °C (f) 800 °C.

Conclusions

- In this study, $Co_{65}Pt_{35}$ films with (111) and (002)-texture on glass substrate have been successfully prepared by sputtering.
- The intensity of peak of (111) phase is enhanced gradually and accompanied with (002) peak as the annealing temperature is increased.
- The decreased coercivity with annealing temperature results from enlarged sizes of grain and magnetic domain.
- Young's modulus and Hardness of CoPt films is decreased with the annealing temperature, related to larger grain size.

Significant enhancement of ΔE effect in $Fe_{87}Ga_{13}$ alloy by doping 0.2 at% Dy

D.H. Tseng[1], Y.H. Liao[1], H.W. Chang[2], S.U. Jen[2], C.R. Wang[1], W.C.Chang[2]

1 .Department of Applied Physics, Tunghai University, Taichung, 407 Taiwan
2 .Department of Physics, National Chung Cheng University, Chia-Yi, 621 Taiwan

Introduction

- Fe-Ga, Galfenol, alloys have attracted increasing attention due to high mechanical strength, good ductility, high imposed stress levels, low coercivity, and large saturation magnetostriction ($\lambda s \sim 350$ ppm) at low external magnetic field (Hs ~ 100 Oe).
- The magnetostriction of Fe-Ga alloy can be significantly increased by adding small amounts of R attributed to the formation and the tetragonal deformation of D03 phase caused by second-order crystal field interaction.
- In this work. effects on the mechanical properties including Young's modulus (E) and shear modulus (G) at magnetic field (H), that is ΔE and ΔG effect, magnetic properties, magnetostriction, and magneto-mechanical coupling due to the Dy-doping have been studied.

Experiment

$Fe_{87-x}Ga_{13}Dy_x$ (x=0、0.2、1.0、2.0) alloys prepared by Induction melting ⇨ Water quenched after 800^0C, 3hr quartz tube heating ⇨ Analysis (RFDA、MS-meter、RLC-meter、XRD)

Result and discussion

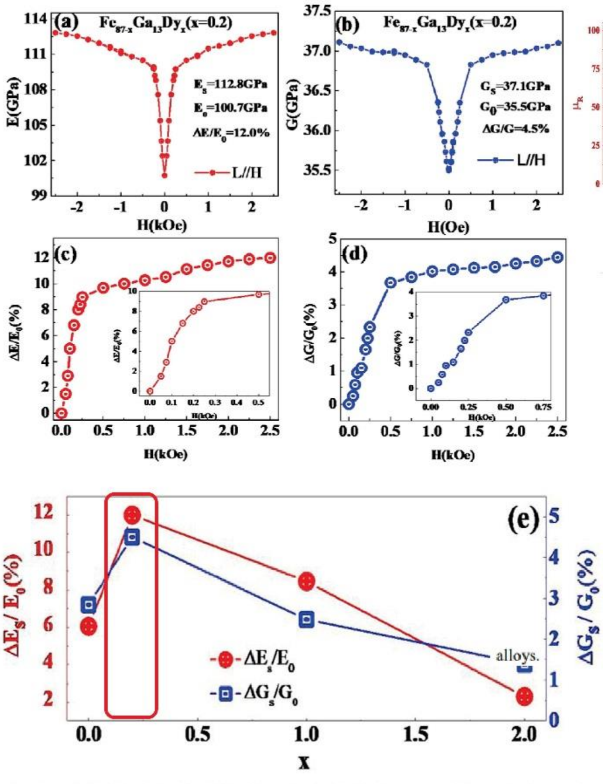

Fig.1 (a) E-H, (b) G-H, (c) $\Delta E/E_0$-H, and (d) $\Delta G/G_0$-H curves of $Fe_{86.8}Ga_{13}Dy_{0.2}$ alloy (e) $\Delta E_s/E_0$ and $\Delta G_s/G_0$ of $Fe_{87-x}Ga_{13}Dy_x$ (x=0-2) alloys.

$$K = \frac{\text{elastic (or mechanical)energy}}{\text{magnetic energy}}$$

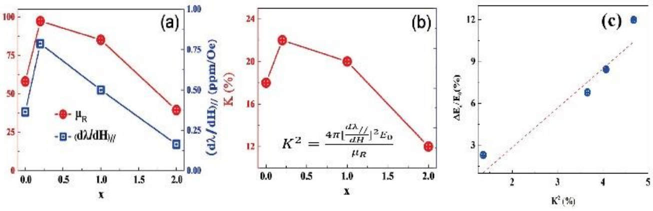

Fig.2(a) μ_R, $d\lambda_{//}/dH$, (b) K as a function of x and (c)$\Delta E/E_0$ as a function of $K^2$for $Fe_{87-x}Ga_{13}Dy_x$ (x=0-2) alloys

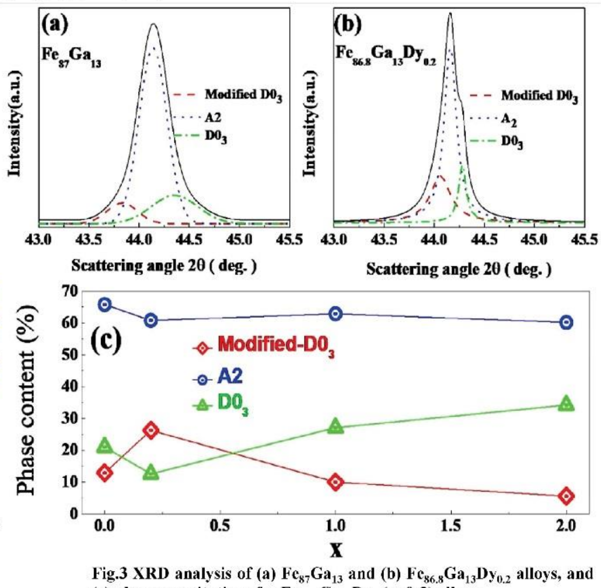

Fig.3 XRD analysis of (a) $Fe_{87}Ga_{13}$ and (b) $Fe_{86.8}Ga_{13}Dy_{0.2}$ alloys, and (c) phase constitutions for $Fe_{87-x}Ga_{13}Dy_x$ (x=0-2) alloys.

Conclusons

- The attractive $\Delta E/E_0$ of 5 % at very small H = 0.10 kOe and a significant enhancement of about 100 % from 6.1 % to 12.0 % in $\Delta E/E_0$ at H = 2.5 kOe achieved for $Fe_{86.8}Ga_{13}Dy_{0.2}$ alloy favors for applications.
- Large ΔE effect or magneto-mechanical coupling is considered to correlate to modified phase constitution by doping Dy and magnetic softening.
- The proportional relation between $\Delta Es/E_0$ and K^2 suggests that the experimentally $\Delta Es/E_0$ is consistent with theoretically calculated K^2 .
- This work provides an effective method for significantly enhancing the ΔE and ΔG effects and magnetostriction sensitivity for Galfenol alloys.

Organic solvents detectors using TMPTA/liquid crystal composited films

Ting-Shen Li (李鼎燊) and Chia-Yi Huang (黃家逸)*
*chiayihuang@thu.edu.tw
Department of applied physics, Tunghai University,
Taichung, Taiwan

Abstract

The TMPTA/liquid crystal composited films are fabricated from the mixture of TMPTA ,HTW and photoinitiator .An empty cell with homogeneous alignment layers is filled with the mixture, and then cured using UV light for 40 minutes. After polymerization, the composited films are taken out from the cell. Acetone, alcohol and their mixture are deposited on the composited films. The transmittance of these films are measured with time. Experimental results depict that the transmittance of the film that exposes to alcohol is constant with time, but that of the film that exposes to acetone linearly varies with time. The transmittances of the film that exposes to the mixtures of acetone and alcohol decrease with time. Therefore, the TMPTA/liquid crystal composited films can be used to detect organic solvents.

Fabrication

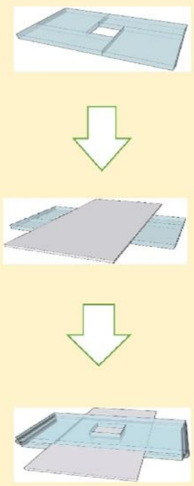

First of all, we make three kinds of liquid crystal composed, 65% of TMPTA (polymer liquid crystal), 33% of HTW (nematic liquid crystal), 2% of (Photoinitiator), and we made the liquid crystal (LC) on the rubbed films of 2cm*2cm glass-box which has already alignment, and the thickness of liquid crystal film is about 50 μm. Then, we use UV light made the LC box curing for 40 minutes, and the LC will become a film inside the box, and we take out the film from the box. After that, wwe cut four pieces of 1x2 glasses, using AB glue to stick to a big glass, after making 2 big glasses, we first stick 2 pieces of big glasses to become a small glass instrument. We use 20μm spacer to create a space so that we can put LC film into the instrument. Then creating a 1x1 hole at the middle of the instrument, and put the organic solvents droplets on the middle of that hole.

Results

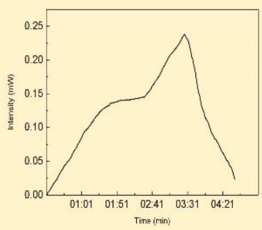

1)the change of light intensity for acetone (8μl)

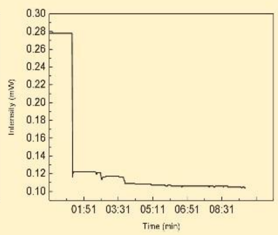

2) the change of light intensity for alcohol (8μl)

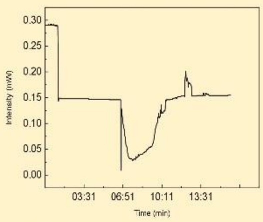

3) the change of light intensity for acetone alcohol hybrid (1:1)

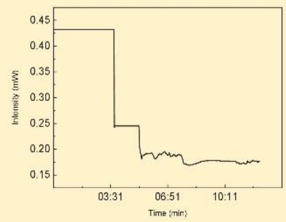

the change of light intensity for acetone alcohol hybrid (1:2)

Conclusion

We found out that LC film had the ability for detect various of solvents. In this experiment, we saw some change of reaction of different percentage of hybrid liquid composed. To enhance the sensitivity of our LC film, we discuss that the ups and downs after we drop the solvents on the film. The amounts and concentration is the main points that influence how the linearly chart goes. We will find out more kinds of different solvents to test in the future (or even use gas). Since there's some poison and harmful solvents fulfill in our environment, maybe the small film can be a new instrument of detection in everywhere in the future.

Acknowledgement

This research was financially supported by the Ministry of Science and Technology (MOST) of Taiwan under contract no. MOST 107-2112-M-029 -005 -MY3

東海大學

Detection of mercury ions using liquid crystal cells with photoresist grids

Yuan-Ming Liu(劉原銘) and Chia-Yi Huang* (黃家逸)
*chiayihuang@thu.edu.tw

Department of applied physics, TUNGHAI UNIVERSITY, Taichung, Taiwan

Abstract

Photolithography is used to fabricate photoresist grids, and vertical alignment films are deposited on the grids. The mixture of 5CB liquid crystal (LC) and ZT ligand is dropped on the photoresist grids. After mercury ions react with ZT, the LC appears non-uniformly bright as the photoresist grids are placed between two orthogonal polarizers. Experimental results depict that the LCs in the photoresist grids exhibit uniformly bright states as the 5CB/ZT mixture is spin-coated on the photoresist grids. The limit of detection for the concentration of mercury ions is 10^{-12} M. Therefore, the photoresist grids with the 5CB/ZT mixture can be used to develop mercury ion sensors. The ion sensors are compact, easy to carry, highly sensitive and real time.

Fabrication

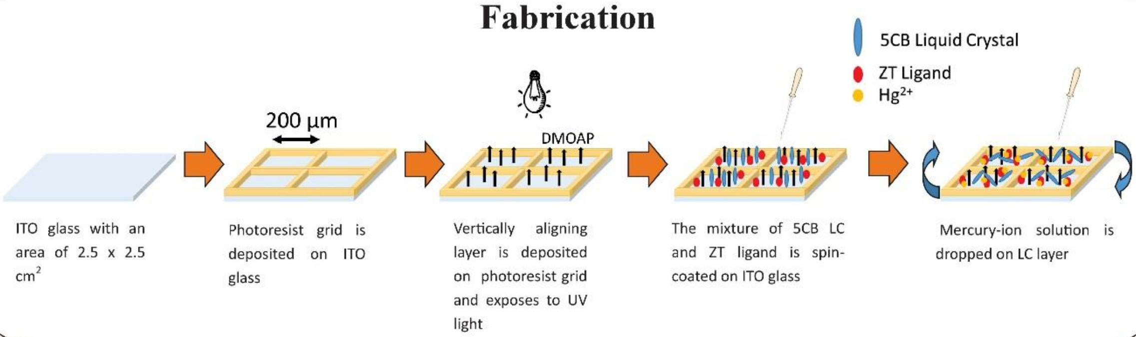

Theory

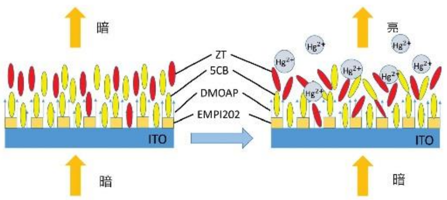

When the system was immersed in the solution containing Hg^{2+}, the complex of ZT and Hg^{2+} formed, which disrupted the orientation of LC and lead to a dark-to-bright transition of the image of LCs which is put in an optical microscope with crossed polarizers.

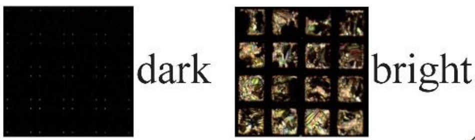

Experiment

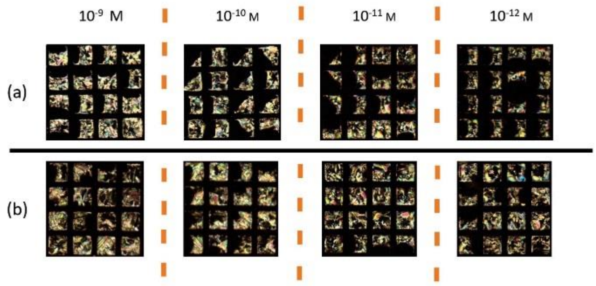

The image of samples which is put in an optical microscope with crossed polarizers, and by (a) titration (b) spin coater to coat ZT-doped 5CB on the photoresist grids.

Acknowledgments

This research was financially supported by the Ministry of Science and Technology (MOST) of Taiwan under contract no. MOST 107-2112-M-029 -005 -MY3

Conclusion

The liquid crystal cell can be used to develop test strips for the determination of mercury ion in aqueous samples. The test strips are compact, easy to operate and visible to naked eyes. The method to coat ZT-doped 5CB on the photoresist grids by spin coater. It could greatly increase the uniformity of the bright state.

东海大學

Uniformity of blue phase liquid crystal cells with in-plane-switching electrodes

Yan-Shou Lin(林彥守), Chia-Yi Huang*(黃家逸)
*chiayihuang@thu.edu.tw
Department of applied physics, TUNGHAI UNIVERSITY, Taichung, Taiwan

Abstract

Blue phase liquid crystal (BPLC) cells exhibit non-uniform domains as the cells have no alignment layer on theirs substrates. Photolithography is used to fabricate in-plane-switching (IPS) electrode. We intend to use IPS electrodes to fabricate an uniform BPLC cell due to their unidirectional structures.

Fabrication

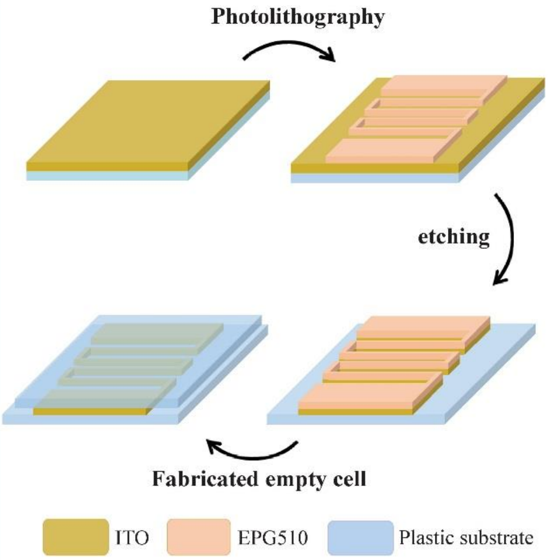

We cut plastic into 2 cm × 2 cm in pieces and the thickness is about 125 μm, then we deposited ITO on the plastic substrates by sputtering. After that, we used lithography to fabricate in-plane-switching electrode pattern and etching ITO from substrates. We filled with blue phase liquid crystals in empty cell which is fabricated.

Experiment

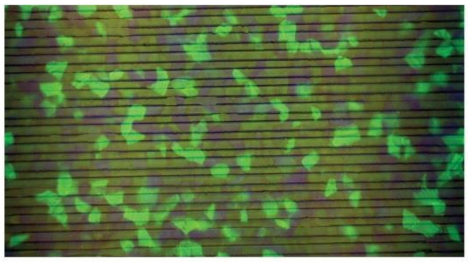

There is a gap between ITO and upper substrate.

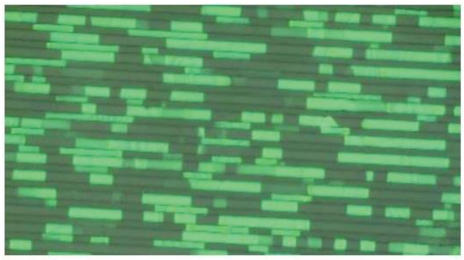

There isn't a gap between ITO and upper substrate.

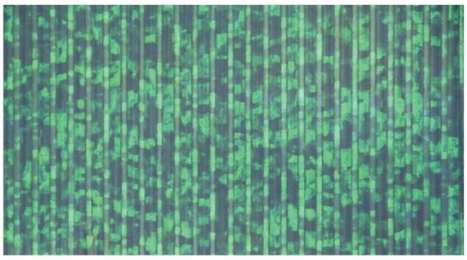

Using thermal cycling.

Conclusion

In this experiment, we use in-plane-switching electrode structure to support blue phase liquid crystal aligned, but this method need to enhance the process to let blue phase liquid crystal more uniform and spend less time.

Acknowledgments

This research was financially supported by the Ministry of Science and Technology (MOST) of Taiwan under contract no. MOST 107-2112-M-029 -005 -MY3

东海大學

Determining the position of soma with deep learning

光電三 黃關明
指導教授：施奇廷

Department of Applied Physics, Tunghai University, Taiwan[1]

Abstract： Artificial intelligence has become a technology that cannot be ignored in the 21st century. In particular, deep learning has great progress in recent years, especially in the fields of Image and speech recognition. Research in neuroimages has also made significant progress the help of artificial intelligence. *FlyCircuit*, the largest database of single-neuron images of *Drosophila* brain is established in the Brain Research Center in NTHU, Taiwan. Current available data in *FlyCircuit* were processed manually or semi-automatically. The approach is labor intensive and time-consuming. In this study, deep learning techniques are used to locate the soma position of neurons from the *Drosophila* brain images. This is the first step to fully automate the image process procedure, which can save labor and time. Convolutional neural network (CNN) is a powerful deep learning technique for image recognition. A CNN is composed of convolutional layers at the top, a pooling layer, a flatten layer, and fully connected layers. This structure enables the convolution neural network to take advantage of the two-dimensional even three-dimensional structure of the input data. The results show that 95% of the soma can be correctly detected from 1399 neuronal images.

Introduction

Target

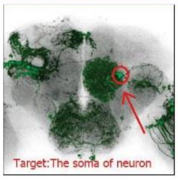

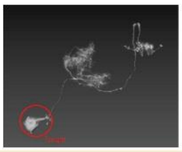

Convolution neural network

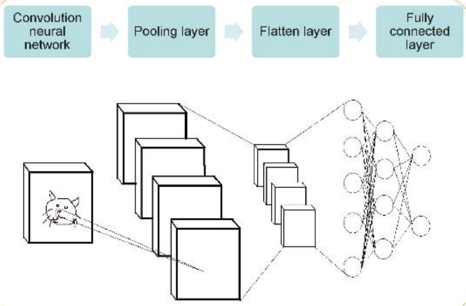

Experimental design

The neuron structure can be roughly divided into tow parts : soma , and neurite. The neurites are divided into dendrites and axon. Axon tend to be very long. So that we can "Tracing" the past data to mark the end points and the soma of the cells. Capture the position and surrounding image of the soma and the end point in the original image. Mark soma as 1 and mark end point as 0 to train the model.

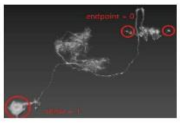

Machine Learning Framework and Result

Machine Learning Framework

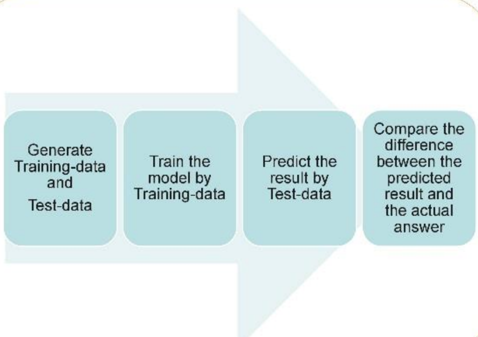

Result

- Test Data :183811
- 1399 Data for soma
- 182412 Data for endpoint
- Accuracy : 0.994
- Guess soma's Accuracy = 0.946
- Guess endpoint's Accuracy = 0.9941

Guess: Soma , Ans: Soma

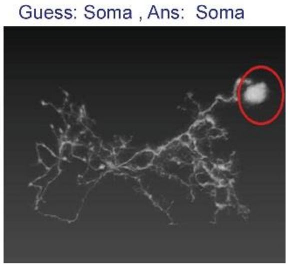

Guess: endpoint , Ans: Soma

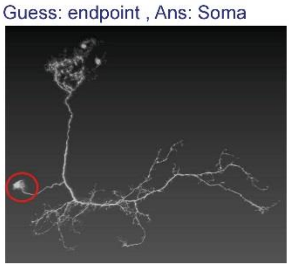

Guess: endpoint , Ans: endpoint

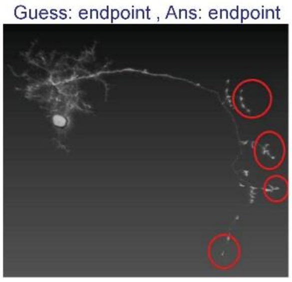

Guess: Soma , Ans: endpoint

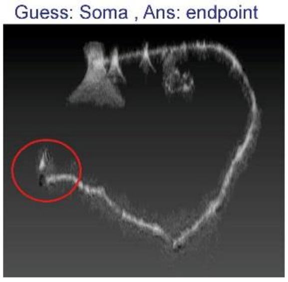

Summary & References

Summary
- CNN model is ideal for processing images, even 3D images
- . number of endpoints is much larger than number of somas
- The amount of data is nor balanced (soma's data and endpoint's data),need to try to balanced it.

References
- http://www.flycircuit.tw
- McCulloch W.S. and Pitts W., "Alogical Calculus of the Ideas Immanent in Nervous Activity," Bulletin of Mathematical Biophysics, 1943
- G.-W. He et al., Neuroinformatics 2017
- L. Liu, et al,"The Treasure beneath Convolutional Layers-Cross-convolutional-layer Pooling for Image Classification," CVPR, 2015.

Study of Two-dimensional Gratings with High Aspect Ratios and Their Prospect in Liquid Crystals

Ting –Yun Wang (王亭勻)and Chia-Yi Huang*(黃家逸)
*chiayihuang@thu.edu.tw

Abstract

We fabricated **High Aspect Ratio, HAR with lithograph and research** the diffraction characteristics, and used a fishnet mask in the prepared samples for grating preparation. In the measurement of diffraction properties, we tested the diffraction intensity、diffraction efficiency and polarization with a Hi-Ne laser, and it is observed that the diffraction efficiency of the two-dimensional is better than the planar gratings from the results of the diffraction intensity .We hope that the zero-order light energy of the laser diffracted light can be distributed to high-order terms through this grating by this study. We hope to apply the scanning elements of face recognition by the high diffraction efficiency of high aspect ratio gratings in application .

Department of applied physics,

Fabrication

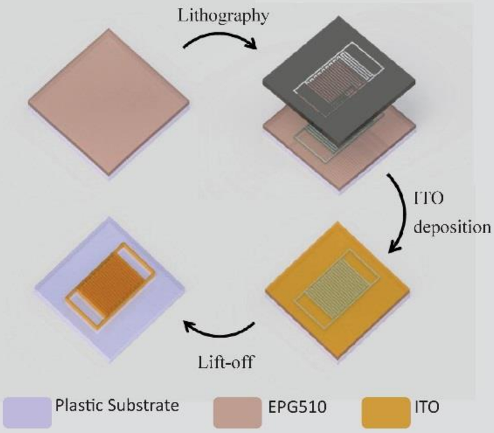

After the ITO is deposited on photoresist surface after patterning by sputtering. Because the target is isotropic scatter in sputter, the ITO particle uniform spread in the groove of the photoresist and none of photoresist. After putting the sample of ITO sputtered into dimethyl ketone, the photoresist under the sputtering layer ITO dissolved by the dimethyl ketone causing the ITO layer above the photoresist be detached. Take out after soaking for fifteen minutes and bake at 80° c for five minutes to dry the excess water , complete the High Aspect Ratio

Result

Planar Structure	HAR Structure
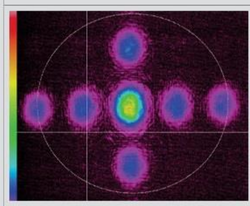	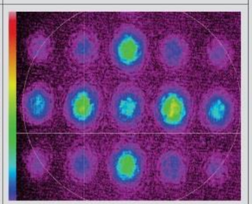
Diffraction Power Density (W/cm^2)	Diffraction Efficiency (%)
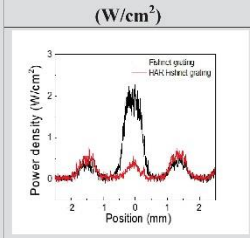	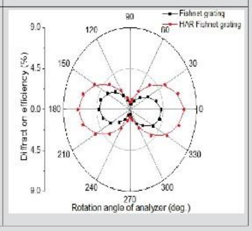

Conclusion

High Aspect Ratio gratings are fabricated with lithograph, which has distinct diffraction properties compared to planar gratings in this topic. The experimental shows that the diffraction efficiency of the two-dimensional high aspect ratio grating is greater than the diffraction efficiency of the two-dimensional plane grating. That is to say, a high aspect ratio grating is more capable of equally dividing the energy of incident light to higher order diffracted light than a planar grating. We hope to apply the identified scanning elements by the high diffraction efficiency of high aspect ratio gratings in application. It is more desirable to add liquid crystals to adjust the intensity in future and allow it to regulate the intensity and polarization of diffracted light through voltage and to increase the application of identifying scanning elements, such as face recognition, fingerprint recognition.

Acknowledgement

The authors would like to thank the guidance of Mr. Chia-Yi Huang, the help of the students and the R.O.C Taiwan Liquid Crystal Society.

TUNGHAI UNIVERSITY, Taichung, Taiwan

東海大學

Uniform blue-phase liquid crystals on Mylar spacers

Yi-Chen Ma (馬翊宸) and Chia-Yi Huang* (黃家逸)
*chiayihuang@thu.edu.tw

Department of applied physics, TUNGHAI UNIVERSITY, Taichung, Taiwan

Abstract

Blue phase liquid crystal (BPLC) cells exhibit non-uniform textures as they have no alignment. As an empty cell that is separated by 12 um-thick spacers is filled with a BPLC mixture, the mixture may flow to the spacers of the cell. Experimental results display that the BPLC mixture on the spacer is uniform. BPLC cells with different cell gaps are used to find the reason. The BPLC textures in the cells are evaluated by OM and AFM. Uniform BPLC cells can reduce their hysteresis, and be used to develop photonic devices, displays, electro-optical switches and electrically tunable focusing LC lenses.
Keywords：photoelectric，blue phase liquid

Fabrication

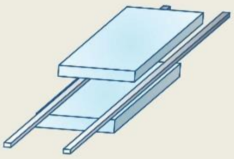

1.Prepare two pieces of ITO glass and place spacers on both sides of it, use a magnet to fix the upper and lower sides of the glass. .(ITO facing inward)

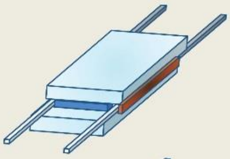

2. Put the ab glue both sides of the cell where have spacers, Wait until the glue is dry, remove the magnet. The blue phase of mixtures appeared at the temperature T< 32.2 ˚C. The mixture at isotropic state (~60 ˚C) was filled into an empty LC cell consisting of two ITO glass.

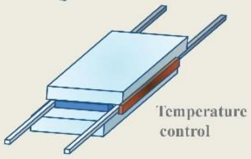

3.We heated up the cell to 33 ˚C and then cooled down the cell to 24.5 ˚C at the cooling rate of 0.5 ˚C /min。

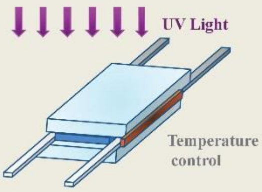

4. The cell was then exposed by UV light at 24.5 ˚C with intensity ~1.5 mW/cm2 for 60 minute for photo-polymerization.

Experiment

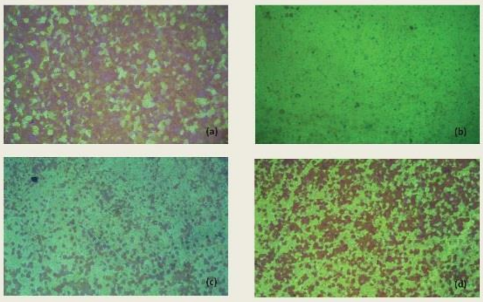

Figure1 (a) Blue phase liquid crystals grown on ITO glass. (b) Blue phase liquid crystals grown on 12um pet spacer. (c) Blue phase liquid crystals on 25um pet spacers. (d) Blue phase liquid crystals on 50um pet spacers.

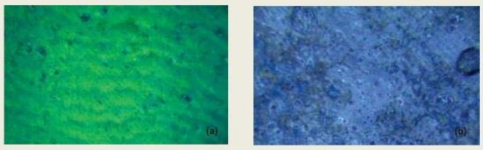

Figure 2 (a) blue phase liquid crystals grown on the 12um pet spacer's 40x om image. (b) 2um pet spacer's 40x om image.

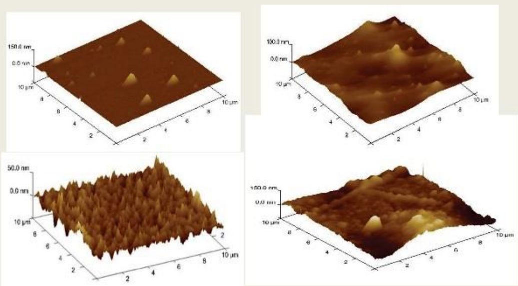

Figure 3 (a) surface structure of ito glass's afm image. (b) surface structure of the 12um 50um 100um pet spacer's afm image respectively

Conclusion

This research infers the possible mechanism of uniform growth of blue-phase liquid crystals on the pet spacer by observing and comparing the surface structures of different it。The groove-like surface structure gives the blue-phase liquid crystals similar rubbing alignment results, which can be used to further develop uniform blue-phase liquid crystals. It is hoped that the blue-phase liquid crystal will be the mainstream optoelectronic component in the future by giving full play to its fast response and other advantages.

Acknowledgments

This research was financially supported by the Ministry of Science and Technology (MOST) of Taiwan under contract no. MOST 107-2112-M-029 -005 -MY3

東海大學

全固態鋰離子電池製備之研究

何名元，陳政遠，陳穎億，蕭錫鍊
東海大學應用物理學系

固態鋰離子電池為近年最具潛力的固態電池，然而低離子導電率、高接面阻抗和低電容量一直是待以解決的問題，本專題研究先個別探討。。。的製備條件，以金屬媒電漿輔助化學氣相沉積系統合成矽奈米線，並在奈米線上長高密度石墨牆，做為陽極，再利用電子束蒸鍍法在上分別蒸鍍出LLZO、Li_2O及Ga_2O_3，重複鍍膜以得到多層膜固態電解質，其中改變LLZO、Li_2O及Ga_2O_3的蒸鍍順序，和調變其相對厚度做為變因，以找到最佳條件，接著利用射頻磁控濺鍍系統鍍上$LiCoO_2$為陰極，並加以退火，最後鍍上金做為電極，形成具有高離子導電率的$Li_{7-3x}Ga_xLa_3Zr_2O_{12}$電解質的固態電池。

簡介

近年液態鋰離子電池逐漸成為主流電池，也是電動汽車的主要動力來源，雖然至今為止仍然是液態鋰離子電池在主導市場，但其容易自燃的特點，使得安全問題一直難以根除，相形之下固態鋰離子電池即備受矚目，而因其具有高化學穩定性、不易燃、無腐蝕、不揮發等多項優點，對於提高電池的循環穩定性有所幫助，另外固態電解質高能量密度的特點，使得電池輕量化的可能指日可待；其中高化學穩定性令其對於陰、陽極的相容性有所幫助，然而低離子導電率、高接面阻抗和低電容量。因此本研究計畫將以沉積多層膜的結構，藉由改變膜與膜之間厚度比例及沉積順序，以找到可重複製備的高導電 $Li_{7-3x}Ga_xLa_3Zr_2O_{12}$薄膜最佳化的固態電解質薄膜，並加以製成固態電池。

研究方法

本研究工作分為二個部分，第一部分為陰極、陽極及電解質的合成及分析，以找出最佳化製程條件；其次為以所得的最佳化的陽極、陰極及電解質製成電池，最後分析測量電池特性。

1.陽極製備

a.石墨牆包覆矽奈米線之成長

利用電漿輔助化學氣相沉積系統(圖1)生長出的石墨牆包覆矽奈米線(圖2)，利用循環法量測，為避免探針將矽奈米線損毀，因此在表面滴上鎵的液滴，再進行量測(圖3)。

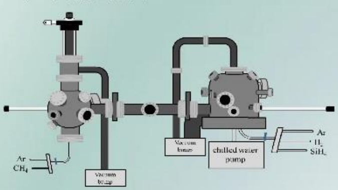

圖1.電漿輔助化學氣相沉積，電子層沉積系統示意圖。

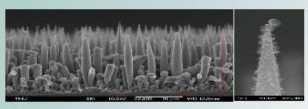

圖2.石墨牆包覆矽奈米線的SEM圖

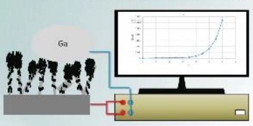

圖3. 循環充放電法示意圖

b.陽極特性分析

- 掃式電子顯微鏡及穿透式電子顯微鏡:分別觀察矽奈米線包覆石墨牆的表面形貌及結晶性。
- 熱探針法:量半導體載子濃度
- 奈米線電阻率量測

2. 多層膜固態電解質之合成

a. 電解質製備

將LLZO、Li_2O及Ga_2O_3以坩鍋乘載，分層將材料鍍於基板，得到多層膜電解質，並加以退火。

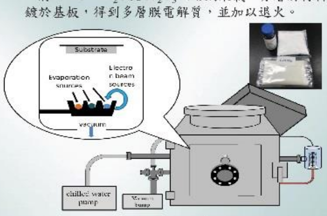

圖4. 電子束蒸鍍系統示意圖和預鍍材料圖

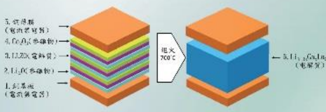

圖5. $Li_{7-3x}Ga_xLa_3Zr_2O_{12}$固態電解質示意圖

b.電解質特性分析

- EIS交流阻抗分析:量測電解質電導率
- X光繞射(XRD):測定電解質結晶相
- X光電子能譜(XPS)：利用X光電子能譜來識別$Li_{7-3x}Ga_xLa_3Zr_2O_{12}$薄膜中的原子濃度，以及元素的相應化學式。

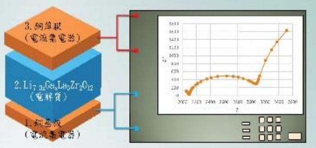

圖6.以交流阻抗分析儀量出電解質之電導率

3.陰極製備

a.$LiCoO_2$之合成

以磁控射頻濺鍍系統在銅基板濺鍍$LiCoO_2$，並在600°C下進行退火。

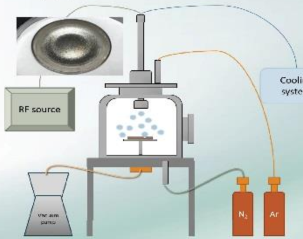

圖7.磁控射頻濺鍍系統示意圖

b.陰極特性分析

- X光繞射:測定電解質結晶相
- 電阻率

4. 全固態鋰離子電池製備

在銅基板上生長矽奈米線並於其表面成長石墨牆，接著分別鍍上最佳化電解質、氧化鋰鈷以及金薄膜

陽極及電器 陰極

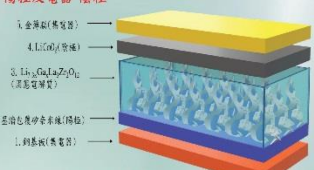

圖8.全固態鋰離子電池結構示意圖

2.固態電解質特性分析

- 循環充放電法:用以計算陽極電容量。
- 循環伏特安培法:主要用來量測氧化劑或還原劑之還原電位。
- 電流密度

預期結果

1.合成出低電阻率的石墨牆包覆矽奈米線的陣列

2.電漿輔助化學氣相沉積系統合成100微米的矽奈米線

3.磁控濺鍍系統鍍出厚度100奈米的LiC_OO_2的陰極

4.電子束蒸鍍系統鍍出10微米的固態電解質

5. 固態電解質之離子導電度大於10^{-3}S

參考文獻

1. Jos F. M. Oudenhoven , Loïc. Baggetto , Peter H. L. Notten, All-Solid-State Lithium-Ion Microbatteries: A Review of Various Three-Dimensional Concepts, Adv. Energy Mater, 10-33 (2011)
2. R. Murugan, V. Thangadurai and W. Weppner, Fast Lithium Ion Conduction in Garnet-Type Li7La3Zr2O12 Angew. Chem. Int. Ed. 46, 7778-7781 (2007)
3. M. RawlenceA. N. FilippinA. WäckerlinT.-Y. LinE. Cuervo-ReyesA. RemhofC. BattagliaJ. L. M. RuppS. Buecheler, The Effect of Gallium Substitution on Lithium Ion Conductivity and Phase Evolution in Sputtered Li7-3xGaxLa3Zr2O12 Thin Films, ACS Appl. Mater. Interfaces,13720-13728 (2018)
4. C. A. Geiger, E. Alekseev, B. Lazic, M. Fisch, T. Armbruster, R. Langner, M. Fechtelkord, N. Kim, T. Pettke and W. Weppner, Crystal chemistry and stability of "Li7La3Zr2O12" garnet: a fast lithium-ion conductor., Inorg. Chem. 50, 1089-1097, (2010)

異質接面背接觸太陽能電池之研製

Y.H. Hsieh (解元亨) and H.L. Hsiao (蕭錫鍊)
東海大學應用物理學系

本研究之目的為異質接面背接觸太陽能電池(Heterojunction Interdigitated Back Contact Solar Cell)之研製，結合了IBC背交指式太陽能電池以及HIT異質接面太陽能電池的優點提高轉換效率，以氫化非晶矽與結晶矽的異質接面搭配全背式電阻最大化提升轉換效率。

◆簡介

太陽能電池發展最重要的是提高轉換效率和降低成本，轉換效率需考慮的是光吸收、表面複合速率、內部複合速率及金屬接觸導電性有關，製程的簡化和精進則是降低成本的關鍵。

目前高效矽晶太陽能電池主流發展有PERC (Passivated Emitter. Rear Cell)、HIT (Heterojunction with Intrinsic Thin layer) 以及IBC(Interdigitated Back Contact)三種結構。本研究採用的HBC結構結合了HIT與IBC兩種結構的優點，他具有HIT結構中晶體矽與氫化非晶矽異質結結構以及IBC的全背電極之優點。前者由於高質量鈍化帶來高Voc[1]，後者因為其無前側電極存在不會產生陰影效應而具有高Isc[2]。本研究結合此兩種技術並參考Panasonic公司達成25.7%高效率的太陽能電池之製程[3]。希望能做以氫化非晶矽與結晶矽的異質接面做出25%以上效率之HBC太陽能電池。

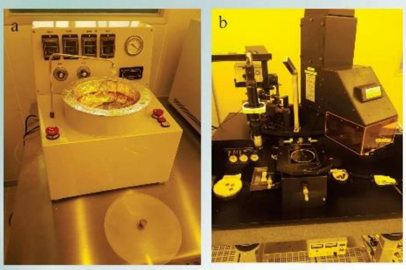

圖一 (a).微影製程中的塗佈機，用塗佈光阻。(b).為曝光機，配合光罩在電池上定義出p、n極。

◆研究方法

1. 清洗基板：
   在通過PECVD進行a-Si：H(氫化非晶矽)沉積之前，清潔基板表面。
2. 進行正面和背面連續沉積：
   正面（a-Si：H（i）/ a-Si：H（n））
   背面（a-Si：H（i）/ a-Si：H（p））。
3. 微影定義背面p型區域並蝕刻：
   此電極背面為p型與n型交錯，故此步驟使用微影技術，以混合酸部分蝕刻去除p層，僅去除n型區域而保留p型區域。
4. 背面沉積a-Si：H(i)/ a-Si：H(n)層：
   經過清洗後，在整個背面上以相同的方式沉積a-Si：H(i)/ a-Si：H(n)層。
5. 微影定義n型區域：
   此步驟必須僅去除a-Si：H（i）/ a-Si：H（n）層，另一方面，a-Si：H（i）/ a-Si：H（p）層不應蝕刻和損壞。使用鹼性蝕刻，由於蝕刻速率的極端差異，我們可以僅蝕刻a-Si：H（i）/ a-Si：H（n）層。
6. 沉積抗反射層：
   在正面a-Si：H層上沉積SiN的ARC。
7. 蒸鍍背電極和電極圖案化：
   通過E-beam (電子束蒸鍍)在背面沉積電極，並使用微影將其圖案化成交叉佈局。

圖二. PECVD系統，用以沉積製程中所需材料至電池原件上。

圖三. HBC太陽能電池之製程步驟圖。

◆參考文獻

1. M. Taguchi, A. Yano, S. Tohoda, K. Matsuyama, Y. Nakamura, T. Nishiwaki, K. Fujita, and E. Maruyama, "24.7% record efficiency HIT solar cell on thin silicon wafer," IEEE J. Photovoltaics,vol.4 (1), pp.96 99 (2014).
2. D. D. Smith, P. J. Cousins, A. Masad, S. Westerberg, M. Defensor, R. Ilaw, T. Dennis, R. Daquin, N. Bergstrom, A. Leygo, X. Zhu, B. Meyers, B. Bourne, M. Shields, and D. Rose "Sun power's Maxeon Gen III solar cell: High efficiency and energy yield," in Proc. IEEE (33th). Conf., pp. 0908 0913 (2013).
3. K. Nakamura, M. Kohira, Y. Abiko, T. Isaka, Y. Funakoshi, and T. Machida, "Development of back contact Si solar cell and module in pilot production line," in Proc. Eur. Photovoltaic Solar Energy Conf (23rd)., pp.1006–1009 (2008).

矽奈米線三維疊層技術之研究

K.C. Liang（梁凱鈞）, Y.A. Ho（何英銨）, H.L. Hsiao（蕭錫錬）
東海大學應用物理系

本論文研究目的使用三維疊層技術取代以往3D列印機無法達到的技術，預期具有高重複性可大面積化以及可控制的組裝技術，進而取代現今容錯率低的電路設計；利用冰轉壓印技術製成的懸浮液，可降低雜質的汙染，且該技術具重複性，預期該奈米線懸浮液具有高純度及高轉移率，並取代以往超音波震盪之懸浮液製程技術。

●簡介

矽奈米線的合成、組裝與應用，在過去這幾年間被廣泛研究，各種電子元件的應用被各大期刊發表，但目前最大的瓶頸與挑戰是組裝，具有高重複性可大面積化以及可控制的組裝技術一直是無法達成的，我們藉由3D列印機設計出三維疊層裝置，最後想要發展可用於三維的電路設計，但在現今的晶圓加工製造過程是相當困難的，所以我們才致力於開發三維疊層技術。

●研究方法

本實驗預定的流程（如圖1），我們利用金觸媒低壓化學氣相沉積（Low Pressure Chemical Vapor Deposition：LPCVD）合成矽奈米線（如圖2），製成過程中通入的磷化氫或乙硼烷氣體（PH_3或B_2H_6）決定矽奈米線為N型或P型，由熱探針法（如圖3）量測矽奈米線可得知其為N型或P型，再使用本實驗的冰轉壓印法轉移矽奈米線（如圖4、5）製成懸浮液。

三維疊層技術分為兩類，其一為超音波噴霧平台（如圖6）由超音波噴霧構築的矽奈米線層狀結構（如圖7），可由上下兩端加電極及電壓量測電阻得知三維疊層結構的電性；其二為噴墨式噴霧平台（如圖8）由噴墨式噴霧構築的矽奈米線層狀結構並雷射熔接（如圖9），由下端鍍上行列式電極量測（如圖10）。

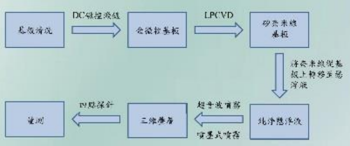

圖 1 實驗流程圖

➤矽奈米線的合成及分析

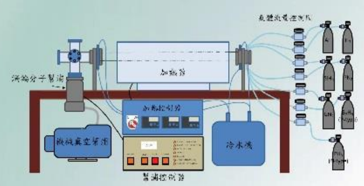

圖 2 低壓化學氣相沉積系統

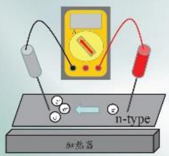

利用加熱器將基板加熱至高溫並測量電流，以此判斷為n型摻雜或p型摻雜。

圖 3 熱探針測量法

➤冰轉壓印矽奈米線懸浮液製備及分析

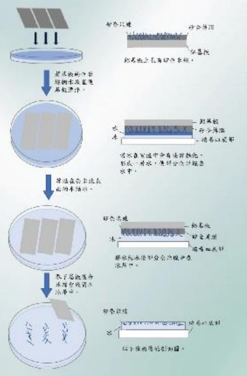

圖 4 冰轉壓印轉移矽奈米線流程圖

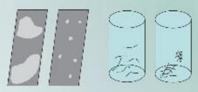

圖 5 實驗分析對照圖

1.經由基板上的矽金薄膜殘留多寡來確定懸浮液的純淨度。
2.測量基板上的奈米線有無斷裂，確定奈米線是否轉移至懸浮液。
3.觀察懸浮液中奈米線是否均勻且不團聚。
4.觀測轉移至懸浮液中的奈米線長度是否有達到預計的長度。

➤超音波噴霧

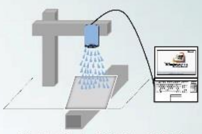

圖 6 超音波噴霧平台示意圖

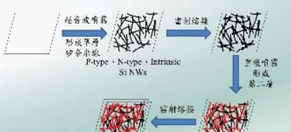

圖 7 超音波噴霧矽奈米線流程圖

➤噴墨式噴霧

圖 8 噴墨式噴霧平台示意圖

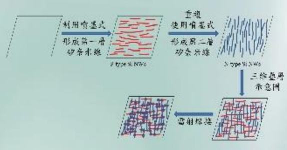

圖 9 噴墨式噴霧矽奈米線流程圖

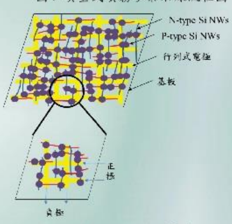

圖 10 使用四點探針測量電性

●預期結果

1. 矽奈米線的合成，我們預期合成100-200μm P型、N型和本質型的矽奈米線，使用熱探針量測為P型或N型。

2. 成功把鋁基板上的矽奈米線透過冰轉壓印方式轉移90-95%到懸浮液裡，以及懸浮液裡的矽奈米線不小於50 μm並且均勻和不團聚。

3. 三維疊層，我們首先確定矽奈米線的均勻性、雷射熔接後是否導電，再放上我們鍍上的電極，設計出容錯式電路。

●參考文獻

1. Bing-Chang Zhang,a Hui Wang,a Yu Zhao,b Fan Li, XueMei Ou, Bao-Quan Sunb and Xiao-Hong Zhang. Large-scale 46 assembly of highly sensitive Si-based flexible strain sensors for human motion monitoring .Nanoscale,8(4):2123-8. 2016.

2. Nipun Misra and Li Xu Yaoling Pan Nathan Cheung Costas P. Grigoropoulos. Excimer laser annealing of silicon nanowires. Applied Physics Letters, 90, 111111. 2007.

3. Young-Soo Sohn ,Jinsung Park ,Gwonchan Yoon,Jiseok Song ,Sang-Won Jee ,Jung-Ho Lee,Sungsoo Na ,Taeyun Kwon ,Kilho Eom. Mechanical Properties of Silicon Nanowires. Nanoscale Res Lett ,5:211–216. 2010.

4. M. Khorasaninejad, S. Patchett, J. Sun, N. O, and S. S. Saini. Diameter dependence of polarization resolved reflectance from vertical silicon nanowire arrays: Evidence of tunable absorption. Journal of Applied Physics, 114, 024304. 2013.

5. Xi Liu, Yun-Ze, Long, Lei Liao, Xiangfeng Duan and Zhiyong Fan. Large-Scale Integration of Semiconductor Nanowires for High-Performance Flexible Electronics. American Chemical Society VOL. 6 ' NO. 3 ,1888 1900 . 2012.

異質接面背接觸太陽能電池之研製

Y.H. Hsieh (解元亨) and H.L. Hsiao (蕭錫鍊)
東海大學應用物理學系

本研究之目的為異質接面背接觸太陽能電池(Heterojunction Interdigitated Back Contact Solar Cell)之研製，結合了IBC背交指式太陽能電池以及HIT異質接面太陽能電池的優點提高轉換效率，以氫化非晶矽與結晶矽的異質接面搭配全背式電阻最大化提升轉換效率。

◆簡介

太陽能電池發展最重要的是提高轉換效率和降低成本，轉換效率需考慮的是光吸收、表面複合速率、內部複合速率及金屬接觸導電性有關，製程的簡化和精進則是降低成本的關鍵。

目前高效矽晶太陽能電池主流發展有PERC (Passivated Emitter Rear Cell)、HIT (Heterojunction with Intrinsic Thin layer) 以及IBC(Interdigitated Back Contact)三種結構。本研究採用的HBC結構結合了HIT與IBC兩種結構的優點，他具有HIT結構中晶體矽與氫化非晶矽異質結結構以及IBC的全背電極之優點。前者由於高質量鈍化帶來高Voc[1]，後者因為其無前側電極存在不會產生陰影效應而具有高Isc[2]。本研究結合此兩種技術並參考Panasonic公司達成25.7%高效率的太陽能電池之製程[3]。希望能做以氫化非晶矽與結晶矽的異質接面做出25%以上效率之HBC太陽能電池。

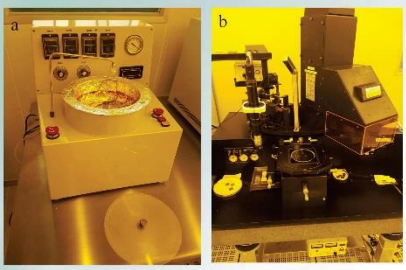

圖一 (a).微影製程中的塗佈機，用塗佈光阻。(b).為曝光機，配合光罩在電池上定義出p、n極。

◆研究方法

1. 清洗基板：
   在通過PECVD進行a-Si：H(氫化非晶矽)沉積之前，清潔基板表面。
2. 進行正面和背面連續沉積：
   正面（a-Si：H（i）/a-Si：H（n））
   背面（a-Si：H（i）/a-Si：H（p））。
3. 微影定義背面p型區域並蝕刻：
   此電極背面為p型與n型交錯，故此步驟使用微影技術，以混合酸部分蝕刻去除p層，僅去除n型區域而保留p型區域。
4. 背面沉積a-Si：H(i)/ a-Si：H(n)層：
   經過清洗後，在整個背面上以相同的方式沉積a-Si：H(i)/ a-Si：H(n)層。
5. 微影定義n型區域：
   此步驟必須僅去除a-Si：H（i）/a-Si：H（n）層，另一方面，a-Si：H（i）/a-Si：H（p）層不應蝕刻和損壞。使用鹼性蝕刻，由於蝕刻速率的極端差異，我們可以僅蝕刻a-Si：H（i）/a-Si：H（n）層。
6. 沉積抗反射層：
   在正面a-Si：H層上沉積SiN的ARC。
7. 蒸鍍背電極和電極圖案化：
   通過E-beam (電子束蒸鍍)在背面沉積電極，並使用微影將其圖案化成交叉佈局。

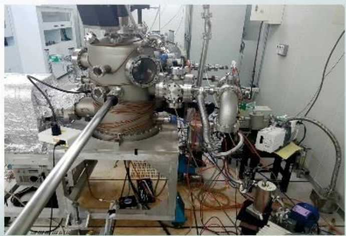

圖二. PECVD系統，用以沉積製程中所需材料至電池原件上。

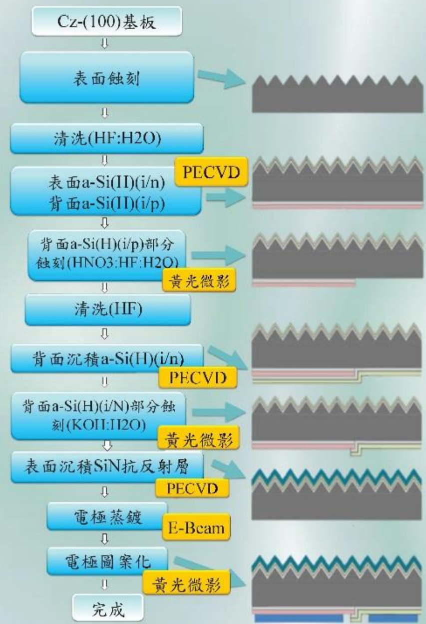

圖三. HBC太陽能電池之製程步驟圖。

◆參考文獻

1. M. Taguchi, A. Yano, S. Tohoda, K. Matsuyama, Y. Nakamura, T. Nishiwaki, K. Fujita, and E. Maruyama, "24.7% record efficiency HIT solar cell on thin silicon wafer," IEEE J. Photovoltaics,vol.4 (1), pp.96 99 (2014).
2. D. D. Smith, P. J. Cousins, A. Masad, S. Westerberg, M. Defensor, R. Ilaw, T. Dennis, R. Daquin, N. Bergstrom, A. Leygo, X. Zhu, B. Meyers, B. Bourne, M. Shields, and D. Rose "Sun power's Maxeon Gen III solar cell: High efficiency and energy yield," in Proc. IEEE (33th). Conf., pp. 0908 0913 (2013).
3. K. Nakamura, M. Kohira, Y. Abiko, T. Isaka, Y. Funakoshi, and T. Machida, "Development of back contact Si solar cell and module in pilot production line," in Proc. Eur. Photovoltaic Solar Energy Conf (23rd)., pp.1006–1009 (2008).

神經元形態特徵分析

許楷翊
指導教授：施奇廷

Department of Applied Physics, Tunghai University, Taiwan

簡介：腦神經研究已是現今科學的新目標，然而基礎科學研究仰賴跨領域的合作。腦神經研究在物理的領域中，將透過物理理論邏輯、物理方法，解決資料處理上所遇到的問題。 FlyCircuit是果蠅大腦單神經元圖像的最大資料庫，由台灣清華大學的腦研究中心建立。動物的行為皆受大腦神經網路控制，神經學家認為：人類許多異常行為是基因上的表現錯誤，但基因與神經網路如何發展出控制各式各樣行為的功能，則是科學目前所遇到的極大挑戰。果蠅跟人類一樣，擁有嗅覺、味覺、聽覺、視覺、痛覺、睡眠、學習和記憶等腦功能，於是對果蠅腦神經元的研究分析，對人類腦功能的研究上有很大的幫助。神經元具有不同的分子、形態、功能屬性，神經元分類，無論在技術上還是概念上都具有挑戰性，生物學家曾使用過『結構性，功能性，分子標準』去規避細胞類型分類的技術障礙。在此研究將使用FlyCircuit資料庫的果蠅神經細胞結構資訊，分析細胞形態上差異的眾多特徵值。

神經元形態差異：問題、策略

影像處理

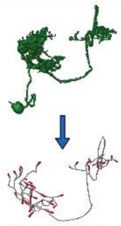

- 利用影像追跡(Tracing)演算法得到結構特徵值：Branch volume、Length、Level、EndToEnd、 Level...

神經細胞形態

Single Neuron Image

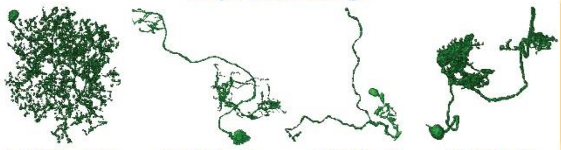

- ***FlyCircuit***資料庫：http://www.flycircuit.tw
- 清華大學生物學家以人工判別四種類型神經細胞類型
- 神經元類型數量尚未有正確答案，於是先透過形態特徵的分析，進行各項量化後的數值比較
- 數量龐大的神經元無法全數透過人工方式識別形態，將藉由特徵分析後所得的特徵量，未來進行形態分群

策略

目標
- 了解量化後之細胞特徵值影響形態的關鍵
- 分析多項特徵值製作各個神經元形態特徵量
- 將特徵量構建神經網路模型，進行大數據分析，達到自動分群目的

策略
- 形態種類劃分：大小、質量分佈(糾結團數量)、糾結團之間距離...等等
- 使用標準分數 (z-score) 排除特徵值之間單位不同之問題
- 40個神經元特徵量進行比對，得出的結果對照目前已知的4種形態類型

實驗與分析

神經細胞大小

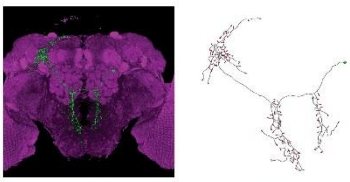

5-HT1B-M-500005（跨多腦區較大）

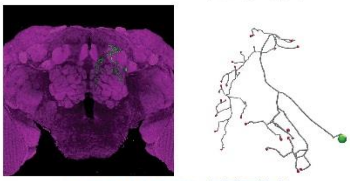

5-HT1B-M-600000（跨腦區較少）

- 透過迴轉半徑進行分析，能判定該神經細胞在大腦中所延伸範圍大小

$$迴轉半徑 = R = \sqrt{\frac{(r_1^2+r_2^2+...+r_n^2)}{n}}$$

- 迴轉半徑特徵值能看出該神經細胞是否跨腦區傳遞訊息
- 此處的迴轉半徑為該神經細胞所有Branch point 對細胞質心的均方根距離

Branch Point 質量分佈

- 每個神經細胞中有數量不一的BP個數，在此對計算每一個BP間的歐氏距離，將距離低於絕對數值劃分為一群
- 計算該細胞的BP群數量，目前所知糾結團結構數量不同多為不同類型神經細胞種類
- 歐氏距離：

e.g. 三維空間上兩點間的歐氏距離 $d_{12}=\sqrt{(x_1-x_2)^2+(y_1-y_2)^2+(z_1-z_2)^2}$

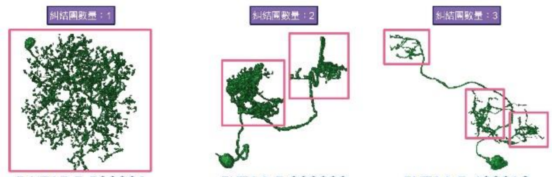

5-HT1B-F-500001 細胞類型：ALLN　5HT1A-F-000000 細胞類型：FB　5HT1A-F-400013 細胞類型：PN

目前進展與未來工作

- 我們經影像追跡(Tracing)演算法獲取神經元結構特徵值
- 對目前已知特徵量進行比對，尚未能成功匹配四個已確定類型，單個神經元特徵值間的權重關係尚需調整
- 下一步將嘗試透過機械學習，調整單個神經元特徵值之間的權重關係，以達到匹配已知類型

- 由於數量龐大的神經元無法全數透過人工方式識別形態上差異，所以形態特徵分析後建立神經網路模型，進行大數據分析，以達到自動分群之目的
- 科學上尚未知曉神經細胞類型的確切種類數量，未來透過形態特徵量所建立的網路模型，所產生的自動分群結果可能有助於人工分類上的問題

References
- Chiang, A.S et al. (2011), "Three-Dimensional Reconstruction of Brain-wide Wiring Networks in *Drosophila* at Single-Cell Resolution" Curr Biol 21, 1-11.
- Shih, C.T. et al., (2015), "Connectomics-Based Analysis of Information Flow in the *Drosophila* Brain" Curr Biol 25, 1249-1258.
- Hongkui Zeng & Joshua R. Sanes (2017), "Neuronal cell-type classification: challenges, opportunities and the path forward" Nature Reviews Neuroscience, 530-546
- http://www.flycircuit.tw

矽奈米線壓力感測器之研究

Y.Q. Chen(陳宥全), H.L. Hsiao(蕭錫鍊)
Department of Applied Physics, Tunghai University, Taichung 407, Taiwan

本專題研究目的是可彎折、高靈敏度、高穩定性且具有影像解析的壓力感測器，以做為智慧製造機器人的觸覺元件。本研究先以金觸媒催化化學氣相沉積及金濺鍍的方法合成金@矽奈米線，再以浸泡烘乾法製備吸附有金@矽奈米線的紙(或布)，然後固化聚二甲基矽甲烷(PDMS)，並濺鍍交指式電極，將固化的PDMS/吸附有奈米線的紙/鍍有電極的PDMS之三明治結構結合形成壓力感測器，希望能製造出可彎折兩萬次、高靈敏度(>1.5/kPa)之16*16影像解析的電子皮膚。

◆簡介

隨著科技進步，AI(人工智慧)與機器人科技的導入與應用，有助於解決不久的未來高齡少子社會型態引發的勞動人口不足、價值創造能力低落，以及產業競爭力衰退等中長期性的社會經濟問題。智慧製造機器人也有助於提升產業生產線效率、並有自動感知、自決策、自執行等功能。而目前智慧製造遇到的困難在於機器人科技還無法取代人工操作的精密性加工，故而希望能有像人類一樣的觸覺、視覺感知系統，才能達到真正的智慧製造科技。

Hongfang Li研究團隊以二維上下電極包覆奈米線結構製備出壓力感測器，具有1.33/kPa的靈敏度，但其偵測壓力範圍狹小，導致在極小壓力變化下就不會再產生電流變化。Morteza Amjadi研究團隊以二維PDMS包覆住一維密集銀奈米線製備壓力感測器雖有不錯的電流變化訊號，但其穩定性不好且彎折傷害性大，重複彎折循環下結構會崩解。本專題研究將以PDMS鍍上交指式電極/吸附有金@矽奈米線的紙(或布)/PDMS之三明治結構製備出可彎折、靈敏度高達1.5/kPa且具有8*8cm²空間解析之高穩定性的壓力感測器，以作為未來智慧製造機器人的觸覺元件。

◆金觸媒催化化學氣相沉積合成矽奈米線

本研究以低壓化學氣相沉積系統製備可控制直徑與長度的矽奈米線。

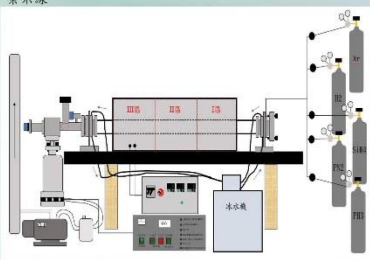

(圖一)低壓化學氣相沉積系統示意圖

◆金@矽奈米線製備

以直流偏壓濺鍍系統濺鍍金薄膜在矽奈米線上，形成金@矽奈米線。

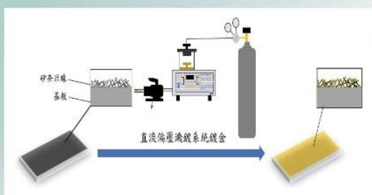

(圖二)矽奈米線鍍金步驟示意圖

◆ 浸泡烘乾法製備附有金@矽奈米線的紙

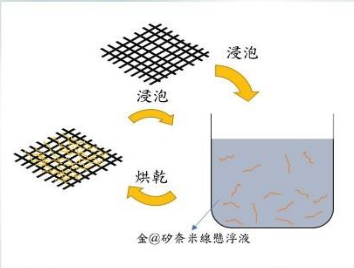

(圖三)製備金@矽奈米線紙之步驟示意圖

(附著前) (附著後)

圖(七)矽奈米線附著無塵擦拭紙

◆ 三明治結構壓力感測器之製造

以雷射切割機製備濺鍍金電極之遮罩。固化PDMS後利用直流偏壓濺鍍系統濺鍍和光遮罩合成交指式金電極，並將附有奈米線的紙覆蓋住電極，在固化PDMS形成壓力感測器。

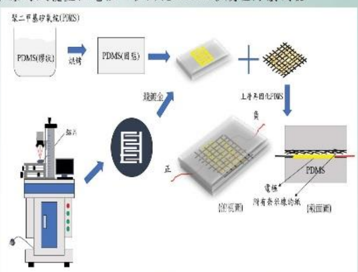

(圖四)壓力感測器製備步驟示意圖

◆壓力感測特性分析

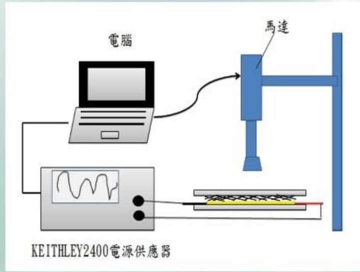

(圖五)壓力感測特性分析儀器示意圖

◆壓力感測器之工作原理

右上角兩張為預測物體在壓力感測器上經由電腦分析訊號後所形成的影像的示意圖

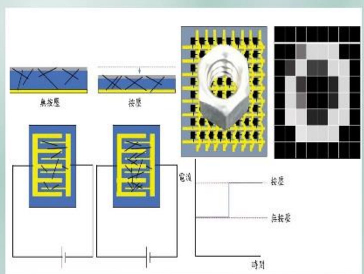

◆ 預期結果

1. 在矽奈米線側面包覆金薄膜形成金@矽奈米線
2. 吸附有高密度金@矽奈米線的紙(或布)
3. 寬的感測壓力範圍(13~2600 Pa)
4. 靈敏度大於1.5/kPa
5. 16*16陣列的影像解析能力(8cm*8cm尺寸)
6. 可重覆彎折超過兩萬次且高穩定性

◆ 參考文獻

1. Morteza Amjadi,Aekachan Pichitpajongkit,Sangjun Lee,Seunghwa Ryu, and Injyu Park, Highly Stretchable and Sensitve Strain Sensor Based on Silver Nanowire-Elastomer Nanocomposite, ACS Nano 8(5), 5154-5163, 2014
2. Hongfang Li, Guifu Ding, and Zhuoqing Yang, A High Sensitive Flexible Pressure Sensor Designed by Silver Nanowires Embedded in Polyimide(AgNW-PI), Micromachines 10(3), 206 (2019)
3. Shu Gong, Willem Schwalb, Yongwei Wang, Yi Chen, Yue Tang, Jye Si, Bijan, and Wenlong Cheng, A wearable and highly sensitive pressure sensor with ultrathin gold nanowires, Nature Communication 5, 3132 (2014)
4. Taemin Lee, Wonoh Lee, Sung-Woo Kim, Jae Joon Kim, and Byeong-Su Kim, Flexible Textile Strain Wireless Sensor Functionalized with Hybrid Carbon Nanomaterials Supported ZnO Nanowires with Controlled Aspect Ratio, Advanced Function Materials 10, 1002 (2016).
5. Chaoxing Wu, Tae Whan Kim, Fushan Li, and Tailiang Guo, Wearable Electricity Generators Fabricated Utilizing Transparent Electronic Textile Based on Polyester/Ag Nanowires/ Graphene Core-Shell Nanocomposites, ACS Nano 10, 6449-6457 (2016).

雷射剝蝕LiPON固態電解質之研究

黃瑞陞，蕭錫鍊
東海大學應用物理系

本專題研究目的是在銅基板上合成矽-石墨奈米複合材料作為陽極，然後利用掃描式脈衝雷射剝蝕系統鍍上均勻固態電解質(LiPON)，再利用射頻磁控濺鍍系統鍍上陰極($LiCoO_2$)，形成穿插結構，製作出高電容量，高充電速率，安全，穩定的全固態鋰離子電池，研究過程中所合成的複合材料及薄膜會透過拉曼、X光繞射分析其結構及成分並以掃描式電子顯微鏡觀測鑑定其形貌。

◆介紹

許多研究團隊努力開發高電容量、高循環穩定性與小體積的電池，期望解決目前可穿戴設備電容量不足的問題，而其中全固態電池是目前受到極大矚目選項之一，由於固態電解質不可燃、無腐蝕、不揮發、不存在漏液問題，因此提高電池的循環穩定性，而且還可以使電池輕量化，具有很大的發展潛力，再加上許多新型高性能電極材料，可能與液態電解液的相容性並不好，但是在使用全固態電解質後該問題可以得到一定的紓解，因此能量密度可以有一個較大幅度的提升。

◆研究方法

本專題利用電漿輔助化學氣象沉積結合氣-液-固成長機制生長 矽-石墨奈米複合材料，利用雷射剝蝕系統(如圖1)通入氮氣鍍上最佳化的固態電解質(LIPON)，再利用射頻磁控濺鍍系統通入氬氣鍍上最化陰極(LiCoO2)，形成穿插結構的全固態電池(如圖2)。

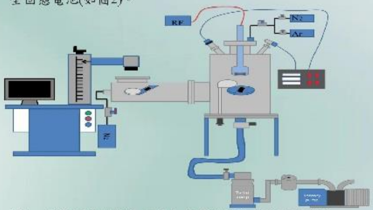

圖1，脈衝雷射剝蝕系統結合射頻磁控濺鍍系統示意圖。

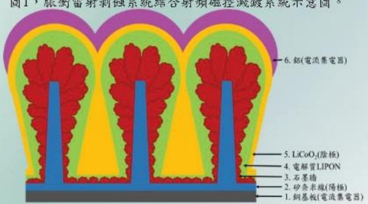

圖2，石墨牆包覆矽奈米線作為陽極之全固態鋰離子電池示意圖。

◆雷射剝蝕系統腔體的選擇

我們在脈衝雷射剝蝕系統腔體的挑選上，使用比較長的腔體(約44公分，如圖3)，避免兩邊的腔體互相汙染，而且腔體也要具備很足夠多的分支(如圖4)，使我夠再適當的位置加裝通氣系統及樣品的載台。

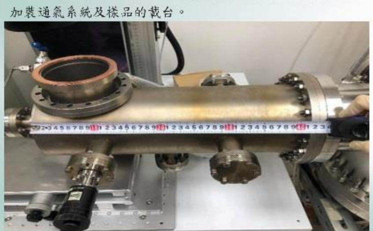

圖3，脈衝雷射剝蝕系統腔體

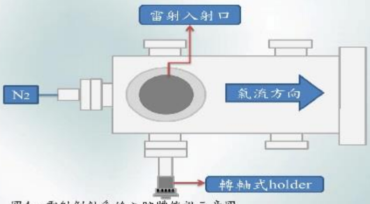

圖4，雷射剝蝕系統之腔體俯視示意圖

◆轉軸式holder的製作

我們在設計了轉軸式的Holder(如圖5、6)，這樣的設計有助於我們在調整雷射在靶材上聚焦時，由於我們是用掃描軟體控制(如圖7)雷射，因此當雷射在掃描的過程中，如果因為靶材表面不平，造成雷射失焦，我們能夠即時利用轉軸式的Holder做調整(如圖8)。

圖5，不鏽鋼Holder 、Holder圓形固定桿

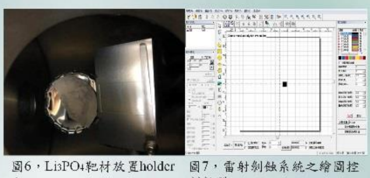

圖6，Li3PO4靶材放置holder上。 圖7，雷射剝蝕系統之繪圖控制軟體。

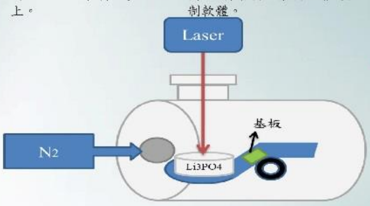

圖8，Holder與通氣口的相對位置示意圖。

◆在室溫下合成LiPON薄膜

我們利用脈衝雷射剝蝕系統製備固態電解質LiPON薄膜，圖9為LiPON薄膜的光學影像圖，圖10為靶材的訊號，可以看出是Li_3PO_4的結構，而圖11是我們利用脈衝雷射剝蝕系統鍍在矽基板上的訊號，從圖中可以看到Li_3PO_4的訊號有出現在樣品上，但是沒有明顯的氮化訊號，推論可能是由於我們的雷射剝蝕過程是在室溫下進行，所以剝蝕出來的Li_3PO_4沒有足夠的能量與氮氣作用，後續我們將針對這一點做進一步的改善。

圖9，LiPON之光學影像圖

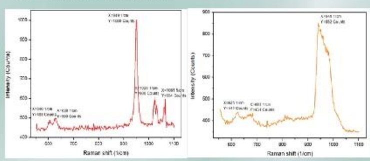

圖10，Li_3PO_4靶材拉曼圖 圖11，LiPON薄膜拉曼圖

◆在室溫下合成LiCoO2薄膜

我們利用射頻磁控濺鍍系統製備陰極$LiCoO_2$薄膜，並藉由光學顯微鏡觀測其表面形貌與拉曼分析其成分，圖12為$LiCoO_2$薄膜的光學影像圖，圖13為靶材的訊號，而我們利用射頻磁控濺鍍系統鍍在矽基板上的$LiCoO_2$訊號，但是我們鍍出來的薄膜沒有$LiCoO_2$的拉曼訊號，推斷可能是在室溫下進行製程，因此退火溫度不足沒有形成結晶相，後續我們將針對它的退火溫度來改善陰極材料製程的條件。

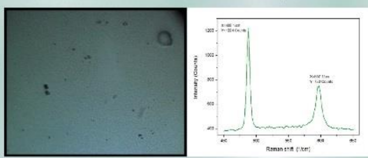

圖12，$LiCoO_2$之光學影像圖。 圖13，$LiCoO_2$靶材拉曼圖。

◆結論

本專題研究已經成功合成筆直、直立的矽奈米線，然後我們將架設好的掃描式脈衝雷射剝蝕系統結合射頻磁控濺鍍系統的真空設備經過多次的測試且運作良好，確保腔體真空度後，我們利用脈衝雷射剝蝕系統將Li_3PO_4薄膜鍍在矽基板上，從拉曼散射光譜分析顯示薄膜成分與靶材相同，沒有明顯氮化的跡象，後續將利用氮氣退火的方式讓它變成LiPON，此外我們也利用射頻磁控濺鍍系統鍍出$LiCoO_2$的薄膜，目前正在進行相關的特性分析，後續我們將繼續優化固態電解質、陰極材料的製程，並結合矽-石墨奈米複合材料製作出全固態鋰離子電池來分析探討其效能。

LAMPS

規則排列鎵陣列之製作

蔡馥亘, 蕭錫鍊
東海大學應用物理學系

◆介紹

隨著太陽能電池不斷的研發改良，最新的研究結果顯示2017年日本的KanekoSangyo公司研發出結合IBC與HIT結構的太陽能電池，其設計的電極位置皆在基板上因此沒有上電極，並結合HIT的單晶矽晶圓與非晶矽薄膜形成異質結構的太陽能電池，而量測到的轉換效率為26.6%1。其轉換效率較2014年日本Sanyo開發出的HIT太陽能電池結構提高1%，Sanyo的HIT異質結構是在PN接面處沉積不摻雜的本質層氫化非晶矽薄膜，形成PIN的異質接面結構2，其中本質層有較高的能隙與光吸收率且具有抗反射的能力，可有效的提高開路電壓，以及減少PN接面的表面缺陷避免載子復合，並改善太陽能電池的轉換效率。雖然IBC與HIT結構的太陽能電池具有較高的轉換效率，但其製作成本卻相當昂貴，因此，一方面要降低成本，另一方面則希望有一定的效能，可能要從不同的角度思考這個問題，像是如何設計PIN接面的結構等問題。

近年來，矽奈米線太陽能電池之所以受到大家矚目，則是因為其可於可撓式基板上合成單晶矽奈米線太陽能電池，且可有效的降低成本。而對於奈米線太陽能電池的研究仍相當的多，根據Jia Zhu等人的研究指出，筆直直立的奈米柱和奈米線結構較薄膜的光吸收率有更好的表現，使光線可更完全的吸收3，但因為利用金屬誘發所生長之奈米線多為測向結晶，再透過電漿之自偏壓(self-bias)將其拉直，使得要長出筆直直立且整齊排列的奈米柱和奈米線並不容易。

本專題將分別透過黃光微影技術及雷射雕刻技術，使基板上的觸媒整齊排列形成陣列，以利未來生長筆直且規則之奈米線，並探討其是否有利於奈米線規則生長。

◆研究方法

本專題將分別利用(一)黃光微影技術及(二)雷射雕刻技術，使基板上的鎵呈現規則的點陣列。黃光微影技術先使光阻上呈現點陣列凹槽，並利用電子束蒸鍍的方式將鎵沉積於基板上後將光阻去除；雷射雕刻技術則先使用電子束蒸鍍將鎵沉積於基板，再利用雷射雕刻出所需點陣列，以利未來生長筆直且規則之奈米線。

1. **黃光微影技術**

   ① 微影觸媒模具

   光阻作為觸媒模具將利用旋轉塗佈法，在氧化矽基板放入烤箱預考後，塗佈正光阻於基板上，完成將基板放入烤箱軟烤，取出後放上曝光機蓋上光罩曝光，接著依序放入顯影劑與DI水中，最後放入烤箱硬烤，並於SEM中探討其厚度及均勻度。

   ② 觸媒製備

   合成矽奈米柱的鎵觸媒將利用室溫電子束蒸鍍（room temperature electron beam evaporation）的方式沉積鎵奈米顆粒於模具上，沉積完成後將基板取出以丙酮浸泡去除光阻，並於SEM中分析表面形貌、厚度及光阻去除完成度。

2. **雷射雕刻技術**

   ① 觸媒製備

   利用室溫電子束蒸鍍的方式沉積鎵奈米顆粒於氧化矽基板上，並採用當膜厚偵測器的讀值約15 nm的鎵薄膜作為催化觸媒，並於SEM中分析表面形貌。

   ② 雷射雕刻

   沉積鎵顆粒的基板利用雷射，將圖形之間分割開，形成點陣列，並於SEM中分析表面形貌及圖形完整度。

最後，可將鍍有鎵陣列之基板，利用電漿輔助化學氣相沉積法，合成筆直直立的奈米線和奈米柱，並比較兩種製程對奈米線生長的影響，以及探討與觸媒無經過陣列排列之奈米線的光電轉換特性差異。

◆結果與討論

圖(1)是利用旋轉塗佈正光阻於氧化矽基板，且於一轉轉速2000 rpm、二轉轉速7000 rpm，旋轉時間分別為10秒、40秒條件下之SEM圖，由圖1(a)(b)(c)中可知，此條件下所得之光阻薄膜厚度約為1.54 ± 0.02 µm，且均勻。

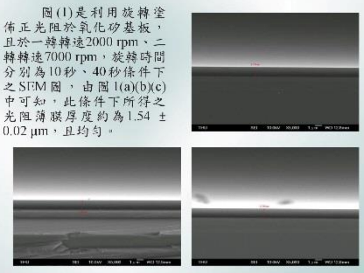

圖(1) 光阻塗佈後SEM圖(a)基板前端厚度約1.52µm (b)基板中端厚度約1.56µm (c)基板後端厚度約1.54µm

圖(2)為光阻曝光後所形成之觸媒模具SEM圖，由圖2(a)可看到曝光後圖形的均勻度極好，每點的直徑約為2.8 ± 0.1 µm，兩點間距約為7 µm；圖2(b)顯示點的深度約為1 µm。

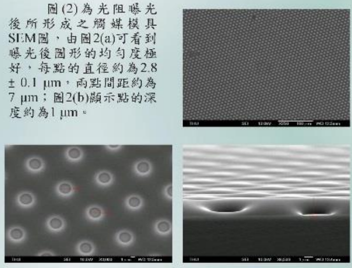

圖(2) 光阻曝光後所形成之觸媒模具(a)俯視SEM圖 (b)俯視放大SEM圖 (c)橫切面SEM圖

在製作觸媒方面，本專題利用室溫電子束蒸鍍於塗佈光阻模具的基板，採用膜厚偵測器讀值為15 nm的鎵沉積於上作為觸媒。圖3(a)(b)為沉積觸媒並去除光阻後SEM圖，由圖3(b)此放大圖可看到去除光阻後，鎵觸媒點完整且排列整齊。但因製程步驟較繁瑣，因此後續將使用製程速度較為快速的雷射雕刻。

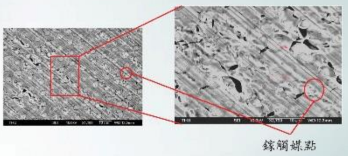

圖(3) (a)鍍鎵並去除光阻後SEM圖 (b)點陣列之局部放大SEM圖

圖4(a)是利用室溫電子束蒸鍍於氧化矽基板，且膜厚偵測器讀值為15 nm的鎵觸媒SEM圖，從SEM圖中觀察到觸媒形貌為顆粒狀，圖1(b)為觸媒直徑統計分佈圖，透過圖像分析軟體將蒸鍍出的觸媒形狀近似成球形，得到的觸媒直徑分佈為50 ± 7 nm，而所使用的雷射雕刻機所雕刻之圖形，最小間距約20 µm。另外，圖5是我們所製作膜厚偵測器讀值分別為10 nm、15 nm、25 nm及100 nm的觸媒直徑大小與膜厚關係圖，從分析的結果顯示隨著膜厚的增加觸媒的直徑大小呈正相關的關係。

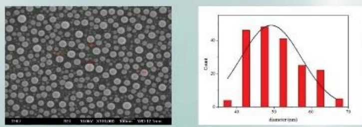

圖(4) (a)膜厚偵測器讀值為15 nm的鎵觸媒SEM圖(b)膜厚15 nm的觸媒直徑統計分佈圖。

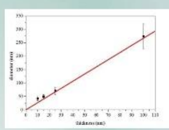

圖(5) 膜厚偵測器厚度與觸媒直徑大小關係圖。

◆結論

使用黃光微影技術的部份，透過室溫電子束蒸鍍鎵於塗佈光阻模具的基板在SEM的觀察下，發現已生長出規則之鎵觸媒點陣列，但因製程步驟較繁瑣，因此後續將使用製程速度較為快速的雷射雕刻。

使用雷射雕刻技術的部分，則在室溫電子束蒸鍍的鎵薄膜於SEM的觀察中，發現鎵觸媒呈現顆粒狀，大小約只為雷射雕刻機所雕刻之最小圖形間距的0.0025倍，進一步使用圖像軟體分析得知，蒸鍍的膜厚與觸媒直徑大小呈正相關的關係。而為了使單一觸媒點所生長的奈米線減少，以利生長筆直直立的奈米線，未來將增加觸媒厚度，以及在鍍有觸媒的基板上生長奈米線，最後比較兩種製程對奈米線生長的影響，並探討與觸媒無經過陣列排列之奈米線的光電轉換特性差異。

◆參考資料

1. Kunta Yoshikawa, Hayato Kawasaki, Wataru Yoshida, Toru Irie, Katsunori Konishi, Kunihiro Nakano, Toshihiko Uto, Daisuke Adachi, Masanori Kanematsu, Hisashi Uzu & Kenji Yamamoto, Silicon heterojunction solar cell with interdigitated back contacts for a photoconversion efficiency over 26%, *Nature Energy*, **2**, 17032, (2017)
2. Corsin Battaglia, Andres Cuevasb, and Stefaan De Wolfc, High-efficiency crystalline silicon solar cells: status and perspectives, *Energy Environ. Sci.*, **9**, 1552-1576, (2016)
3. Jia Zhu, Zongfu Yu, George F. Burkhard, Ching-Mei Hsu, Stephen T. Connor, Yueqin Xu, Qi Wang, Michael McGehee, Shanhui Fan, and Yi Cui, Optical Absorption Enhancement in Amorphous Silicon Nanowire and Nanocone Arrays, *Nano Lett*, **9**, 279-282, (2009)
4. J. D. Beach, C. Veauvy, R. Caputo, R. T. Collins, A. A. Khandekar, T. F. Kuech, C. K. Inoki, T. S. Kuan, and R. E. Hollingsworth, Formation of regular arrays of submicron GaAs dots on silicon, *Appl. Phys. Lett.*, **84**, 5323-5325, (2004)

LAMPS

碳化矽奈米管之合成與特性分析

Z.W. Wang(王政崴), H.L. Hsiao(蕭錫鍊)
東海大學應用物理系

本專題之目的合成出高長寬比碳化矽奈米管。首先在電漿輔助化學氣相沉積系統成長矽奈米線，接著傳輸至原子層沉積系統進行碳化，我們使用四氟化碳作為碳的來源，並以高溫和電漿將矽奈米線表面碳化，最後使用氫氟酸將沒被碳化的矽核蝕刻掉，留下一根根的碳化矽奈米管。

◆簡介

碳化矽具有許多優秀的性質，例如高機械強度、寬能隙、高崩潰電壓(表一)、更好的化學穩定性[1]，近年來更被證實能夠長時間存在於身體內，在生技領域中可以做為生物感測器的第一選擇[2]。做為生物體內感測器，為了不對體內造成過多的負擔，需要以奈米級的尺度來製作，但是合成碳化矽奈米線需要相當高的溫度，許多論文提出的方法皆需要超過1000℃的高溫[3、5]，即使近幾年提出以較低溫合成碳化矽奈米線也需要至少900℃[6]。另一方面，碳化矽奈米管能夠合成出純度更好的碳化矽，原因在於大多數都是以矽奈米線做為基底，再進行滲碳處理，接著蝕刻掉矽的部分，但是此種作法也需要高達1100℃[4]。故本專題以碳化的方法[7]合成碳化矽奈米管，以降低製程溫度，我們將合成出的矽奈米線進行碳化，以氫氟酸蝕刻掉沒被碳化的矽核，留下中空的碳化矽奈米管。再使用掃描式電子顯微鏡和穿透式電子顯微鏡，觀察矽奈米線碳化的情況和碳化矽奈米管是否形成。

	Si 立方晶系	β-SiC 立方晶系	α-SiC 六方晶系	4H-SiC 四方晶系
能隙(eV)	1.12	2.29	3.00	3.20
崩潰電場 (MV/cm)	0.25	2.12	2.5	2.2
熱導率 ($W\,m^{-1}K^{-1}$)	149	360	360	370
電子遷移率 ($cm^2V^{-1}s^{-1}$)	1450	800	600	1000
電洞遷移率 ($cm^2V^{-1}s^{-1}$)	470	40	100	115

表一、矽與其他三種晶型之碳化矽性質比較表

◆研究方法

1.電漿輔助化學氣相沉積系統與原子層沉積系統的架設

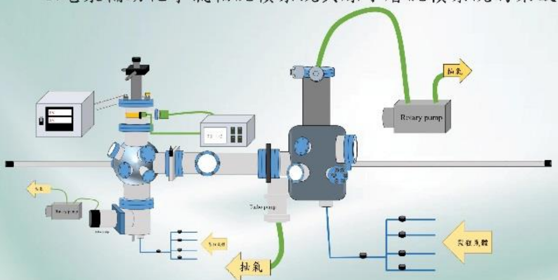

圖一、系統架構圖

2.矽奈米線之合成

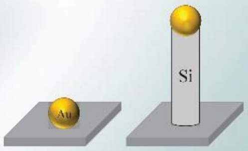

左圖為矽奈米線成長的簡易示意圖。在基板上鋪上金顆粒作為催化劑，矽金合金在約363 ℃時為液相，經擴散等作用由合金底部沉積出矽奈米線。

3.碳化

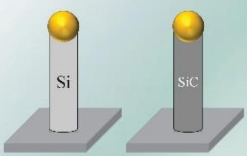

此步驟將矽進行碳化的處理。在腔體內通入CF_4作為碳的來源，在高溫及電漿的作用下將矽奈米線的表面碳化，形成有著碳化矽管壁的矽奈米線。

4.碳化矽奈米管之形成

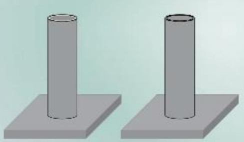

最後使用氫氟酸將碳化矽管壁內的矽蝕刻掉，由於碳化矽對幾乎所有酸鹼不反應，最終只留下碳化矽的奈米管。

◆預期成果

1. 利用電漿輔助化學氣相沉積系統成功成長矽奈米線
2. 使用原子層沉積系統碳化矽奈米線的表層
3. 去除矽核保留下碳化矽奈米管

◆參考文獻

[1] Ivanov P.A. and Chelnokov V.E., *Recent developments in SiC single-crystal electronics.* Sci. Technol. 7, 863–880 (1992)
[2] Saddow S.E., *Silicon Carbide Biotechnology: A Biocompatible Semiconductor for Advanced Biomedical Devices and Applications.* 2nd ed. (2016)
[3] Zekentes, K., & Rogdakis, K., *SiC nanowires: material and devices.* Journal of Physics D: Applied Physics, 44(13), 133001(2011).
[4] Latu-Romain, L., Ollivier, M.et al., *Silicon carbide nanotubes growth: an original approach.* Journal of Physics D: Applied Physics, 46(9), 092001(2013).
[5] Latu-Romain, L., Ollivier, M.et al., *From Si nanowire to SiC nanotube.* Journal of Nanoparticle Research, 13(10), 5425–5433(2011).
[6] Wei-Li Xie, *Low-temperature synthesis of SiC nanowires with Ni catalyst.* Rare Metals, doi:10.1007/s12598-015-0459-8 (2015)
[7] V. V. Zhirnov and E. I. Givargizov, *Chemical vapor deposition and plasma-enhanced chemical vapor deposition carbonization of silicon microtips*.* Journal of Vacuum Science & Technology B: Microelectronics and Nanometer Structures, 12(2), 633(1994)

東海大學應用物理系